SCHOOL OF POSTGRADUATE STUDIES

COLLEGE OF NATURAL SCIENCES

DEPARTMENT OF CHEMISTRY

PREPARATION OF BIOCHAR-BASED NANOCOMPOSITES FOR REMOVAL OF METHYLENE BLUE AND HEXAVALENT CHROMIUM FROM WATER

PhD DISSERTATION

BY

JEMERE KOCHITO AYANO

June, 2024

JIMMA, ETHIOPIA

JIMMA UNIVERSITY
SCHOOL OF POSTGRADUATE STUDIES
COLLEGE OF NATURAL SCIENCES
DEPARTMENT OF CHEMISTRY

PREPARATION OF BIOCHAR-BASED NANOCOMPOSITES FOR REMOVAL OF METHYLENE BLUE AND HEXAVALENT CHROMIUM FROM WATER

BY: JEMERE KOCHITO AYANO

PRINCIPAL ADVISOR: **ABERA GURE (PhD, Prof)**
CO-ADVISORS: **TAMENE TADESSE (PhD, Assoc. Prof)**
OLU EMMANUEL FEMI (PhD, Prof)

A PhD DISSERTATION SUBMITTED TO THE SCHOOL OF GRADUATE STUDIES OF JIMMA UNIVERSITY IN PARTIAL FULFILLMENT OF THE REQUIREMENTS FOR THE DEGREE OF DOCTOR OF PHILOSOPHY (PhD) IN CHEMISTRY (ANALYTICAL)

June, 2024
JIMMA, ETHIOPIA

DECLARATION

I, the undersigned, declare this PhD dissertation, entitled "**Preparation of Biochar-Based Nanocomposites for Removal of Methylene Blue and Hexavalent Chromium from Water** " is my work and has not been submitted for the award of any academic degree or similar qualification at any other institution or university. Furthermore, I confirm that all the sources I have used or quoted have been appropriately indicated and acknowledged.

Name: Jemere Kochito Ayano

Signature: _____

Date: _____

JIMMA UNIVERSITY

SCHOOL OF POSTGRADUATE STUDIES

COLLEGE OF NATURAL SCIENCES

DEPARTMENT OF CHEMISTRY

APPROVAL OF DISSERTATION FOR DEFENSE

We hereby certify that we have supervised, read, and evaluated this dissertation titled "**Preparation of Biochar-Based Nanocomposites for Removal of Methylene Blue and Hexavalent Chromium from Water**" by **Jemere Kochito Ayano.** It was prepared under the supervision of **Abera Gure (PhD, Prof), Tamene Tadese (PhD, Assoc. prof) and Olu Emmanuel Femi (PhD, Prof)**. We recommend submission of the dissertation for the oral defense.

Abera Gure (PhD, Prof)	_____	_____
Principal Advisor	Signature	Date
Tamene Tadesse (PhD, Assoc. Prof)	_____	_____
Co-Advisor	Signature	Date
Olu Emmanuel Femi (PhD, Prof)	_____	_____
Co-Advisor	Signature	Date
Kassim Kedir (M.Sc., Assist. Pro)	_____	_____
Department Head	Signature	Date

JIMMA UNIVERSITY

SCHOOL OF POSTGRADUATE STUDIES

COLLEGE OF NATURAL SCIENCES

DEPARTMENT OF CHEMISTRY

BOARD OF EXAMINERS OF THE DISSERTATION

We, the undersigned, members of the Board of Examiners of the Viva Voce/oral defense by **Jemere Kochito Ayano** have read and evaluated his/her dissertation entitled "**Preparation of Biochar-Based Nanocomposites for Removal of Methylene Blue and Hexavalent Chromium from Water**" and examined the candidate. This is, therefore, to certify that the doctoral dissertation has been accepted for the fulfillment of the requirements of the doctoral degree in Chemistry (Analytical).

_____	_____	_____
Chair Person	Signature	Date
_____	_____	_____
External Examiner	Signature	Date
_____	_____	_____
Internal External Examiner	Signature	Date
_____	_____	_____
Principal Advisor	Signature	Date

DEDICATION

I dedicate this PhD to my late mother Chidache Diro.

ACKNOWLEDGMENTS

First and foremost, I thank Almighty God for being by my side throughout my journey. Secondly, I want to express my heartfelt appreciation to my supervisor, Prof. Abera Gure. Your unwavering support, guidance, advice, and teachings have helped me overcome challenges and complete my PhD studies. Thank you for teaching me how to effectively communicate with the scientific community and publish my work in scholarly journals.

I also want to extend my special thanks to my co-supervisor, Prof. Olu Emmanuel Femi. Your valuable advice, encouragement, and assistance with writing scientific manuscripts, providing laboratory facilities, and helping with sample characterization, including in international laboratories, were instrumental in my success.

Additionally, I would like to thank my co-supervisor, Dr. Tamene Tadesse, for your kind, friendly, and supportive approach. Your guidance, technical assistance in writing, encouragement, and prompt responses to my requests have greatly contributed to my accomplishments.

I am grateful to Jimma University for accepting me as a PhD student in the College of Natural Sciences, Department of Chemistry. I want to express my gratitude to the academic, technical, and administrative staff members in the chemistry department at Jimma University. This study would not have been possible without your support. I will always appreciate the time I spent with you, and the lessons I learned from your curiosity, willingness to share knowledge and materials, and hospitality. I am also thankful for the contribution made by Mizan Tepi University for providing me the study leave and sponsorship during my studies.

My special gratitude goes to my wife, Etalem Brehanu, for your immeasurable patience, love, and encouragement. I passionately thank you for your faithfulness, commitment to our family, and self-sacrifice to shoulder all the responsibility of the family. My thanks go to my son Misganaw and daughters Hiwot, Bereket, and Ermona. Besides your encouragement and moral support for my study, your commitment, persistent courage, and hard work for your educational career with excellent achievements in many areas of living, in the absence of my guidance and assistance, is an unforgettable contribution to my success. Thank you for keeping our home lively and encouraging me each day.

Hereafter, I will make more time to parent and help you learn. Also, I am grateful to my brothers, Fikiralem Kochito and Atrisagn Agelo, for their support and encouragement.

Finally, I would like to extend an enormous thank you to Mr. Solomon Lema, Mrs. Membere Bekele, Mr. Adugna Andemo, Mrs. Asresash Ketema, Mr. Bizuayehu Aboneh, Mr. Hiruy Getachew, Mr. Mebratu Mamo, Mr. Daniel Geneme, Dr. Achame Shana, Dr. Bewuketu Haile, Mr. Tesfa Yitayew, Mr. Tilahun Bekele, Mr. Tadele Bekele, Mr. Mesfin Wondimu, Mr. Teshale Abetto, and too many others to mention by name. Your support and encouragement have made this day possible, and I am forever grateful.

ABSTRACT

Currently, due to urbanization and rapid development, environmental pollution through industrial effluents and unattended disposal of anthropogenic wastes causes health problems and harms the ecosystem in general. Industrial effluents from tanneries, textiles, breweries, metallurgy, dyeing factories, and agro-processing are polluting environmental waters with heavy metals and synthetic dyes. One of the common organic dyes used for coloring paper, cotton, leather, and plastics is methylene blue (MB). However, consuming high levels of MB can result in various health problems, such as respiratory and gastrointestinal issues, eye irritation, and tissue necrosis. Similarly, heavy metals like arsenic, cadmium, and chromium can be harmful to the kidney, liver, brain, and may even cause cancer. Chromium exists in nature mainly in two forms: Cr(III) and Cr(VI), with Cr(VI) being significantly more hazardous than Cr(III). The main objective of this study was to investigate the effectiveness of manganese oxide coffee husk (CH) and khat leftover (KL) biochar nanocomposites and magnetic CH and KL biochar nanocomposites for the removal of MB and Cr(VI) from water.

Each biomass, CH and KL, was pyrolyzed at 300 °C for 1 h to produce the pristine biochars. Similarly, 25 g of each biomass was treated with 12.5 mmol of $KMnO_4$ before being pyrolyzed for 1 h at 300 °C to produce the manganese oxide CH biochar nanocomposite (MnOx-CHBNC) and manganese oxide KL biochar nanocomposite (MnOx-KLBNC). They were characterized by XRD, SEM, FTIR, and BET. The results showed that the adsorbents are amorphous, and the activated biochars are more porous and contain various functional groups such as C-O, C=C, O-H, C-H, and R-MnOx. Additionally, the batch adsorption experiments revealed that MnOx-CHBNC and MnOx-KLBNC have higher efficiency in removing MB and Cr(VI) compared to their pristine biochars. Under the optimized conditions, MnOx-CHBNC exhibited a MB removal efficiency of 99.27% with a maximum adsorption capacity (q_m) of 39.52 mg g^{-1}. Similarly, MnOx-KLBNC showed a MB removal efficiency of 98.28% with a q_m of 43.47 mg g^{-1}. The Cr(VI) removal efficiency of MnOx-CHBNC was 99.63% with a q_m of 72.99 mg g^{-1}, while that of MnOx-KLBNC was 99.84% with a q_m of 109.84 mg g^{-1}.

Similarly, magnetic CH biochar nanocomposites (Fe_3O_4-CHBNC) and magnetic KL biochar nanocomposites (Fe_3O_4-KLBNC) were synthesized by pretreating 25 g of biomass with a 12.5 mmol mixture of FeS and $FeCl_3$ at a 1:1 molar ratio, followed by

pyrolyzing at 300 °C for 1 h. The resulting products were characterized using XRD, FTIR, SEM, and BET. The results showed that the adsorbents are amorphous, and the magnetic biochar nanocomposites are more porous and contain various functional groups such as C-O, C=C, O-H, C-H, and Fe-O. The resulting nanocomposites exhibited a maximum MB removal efficiency of 99.10% and 99.23% with Fe_3O_4-CHBNC and Fe_3O_4-KLBNC, respectively, with q_m of 51.02 and 78.13 mg g^{-1}. Additionally, the Cr(VI) removal efficiencies were determined to be 99.83% for Fe_3O_4-CHBNC and 99.86% for Fe_3O_4-KLBNC, with their Cr(VI) q_m values of 109.89 and 151.52 mg g^{-1}, respectively. The study on the regeneration of the adsorbents found that, except for MnOx-CHBNC in the MB removal test, all adsorbents were effective for the removal of MB and Cr(VI) over six successive cycles. However, MnOx-CHBNC can effectively be used for three successive MB removals from water. Therefore, MnOx-CHBNC, MnOx-KLBNC, Fe_3O_4-CHBNC, and Fe_3O_4-KLBNC can serve as alternative adsorbents for the removal of MB and Cr(VI) from water.

Keywords: Adsorption, Biochar-nanocomposite, Chromium (VI), Coffee husk, Khat leftovers, Methylene blue, Water

TABLE OF CONTENTS

LIST OF FIGURES

LIST OF TABLES

ABBREVIATIONS

BNC	Biochar nanocomposite
BET	Brunauer-Emmett-Teller
CH	Coffee husk
CHB	Coffee husk biochar
DPC	1, 5-diphenylcarbazide
FTIR	Fourier transform infrared
KL	Khat leftover
KLB	Khat leftover biochar
Fe_3O_4-BNC	Magnetic biochar nanocomposite
Fe_3O_4-CHBNC	Magnetic coffee husk biochar nanocomposite
Fe_3O_4-KLBNC	Magnetic khat leftover biochar nanocomposite
MB	Methylene blue
MnOx-BNC	Manganese oxide biochar nanocomposite
MnOx-CHBNC	Manganese oxide coffee husk biochar
MnOx –KLBNC	Manganese oxide khat leftover biochar
pH_{PZC}	pH of point of zero charge
XRD	X-ray diffraction

CHAPTER ONE

1. INTRODUCTION

1.1. Background of the Study

Contamination of the environment with toxic chemical pollutants is a serious worldwide concern [1]. Some of these chemical pollutants consists synthetic dyes like malachite green, congo-red, methylene blue (MB), and crystal violet and some heavy metals such as chromium (Cr), lead (Pb), selenium (Se), mercury (Hg), and arsenic (As). They mainly originate from anthropogenic activities like sewerage, dumping of wastes, mining and industrial effluents, vehicle exhaust, and recreational activities [2]. Following the rapid development and population growth, different industries such as tannery, textile, metallurgy, dyeing factory, and agro-processing are widely spreading in different urban areas. The untreated or partially treated wastewater from such processes is usually disposed into soil and nearby water resources. Therefore, emissions containing toxic chemicals pollute groundwater, surface water, food crops, and agricultural soil, which cause severe and long-lasting human health hazards to the population in diverse ways [3, 4]. Pollution of heavy metals and synthetic dye in an aquatic environment is an increasing worldwide problem, and currently, an alarming rate has reached [5].

Dyes are commonly used in heavy industries like paper, textiles, and food processing for coloring products [6]. From around 100,000 different types of dyes, global annual production of more than 700,000 tons is used in various industries [7]. Reported literature showed that dyes discharged from industries account for 20% of water pollution [8, 9]. These dyes can damage water ecosystems, the food chain, and community health [10]. For instance, even small amounts of dyes in water can have effects on changing the color of water, light penetration, and gas solubility, which are essential for respiration and photosynthesis [11]. Synthetic dyes, such as MB, can be dangerous to human health when they are present in contaminated sources [12]. MB is a common organic dye used for leather and plastic dyeing, coloring paper, and printing cotton. Ingesting or inhaling high levels of MB can lead to acute gastrointestinal issues such as nausea, vomiting, and diarrhea. It can also cause respiratory problems, mental confusion, tissue necrosis and eye irritation [13]. In severe cases, MB exposure can even result in a condition called cyanosis, which is characterized by blue-tinged skin [14]. Additionally, there are potential

long-term concerns such as an increased risk of chronic digestive and mental disorders, blindness caused by eye damage, and respiratory distress [15, 16].

Toxic heavy metals can lead to various health problems in humans, depending on the specific metal, the level of exposure, and how long the exposure lasts [17]. For example, exposure to lead, mercury, and arsenic can harm the brain and nervous system, resulting in learning disabilities, memory loss, developmental delays, and even brain death [18]. Heavy metals can also damage the kidneys, which remove waste products from the blood, causing kidney failure. In addition, heavy metals can damage the liver, which detoxifies the body, leading to liver failure. Some heavy metals, such as arsenic, cadmium, and chromium, are known to be carcinogenic [19, 20]. Chromium is designated as a priority contaminant by the US Environmental Protection Agency (US EPA) [21]. The two primary forms of Cr that are present in nature are Cr(III) and Cr(VI), where Cr(VI) being significantly more toxic than Cr(III). Additionally, due to the higher solubility of Cr(VI), hydrophytes have the ability to absorb it, which can then leach into groundwater and have toxic effects on people [22, 23].

Consequently, it is crucial to use proper treatment techniques before releasing industrial effluents into the environment [24]. Various physical and chemical methods have been utilized for the removal of heavy metals and dyes from industrial emissions [25–30]. However, some of these techniques have drawbacks, such as excessive energy consumption, high expenses, hazardous sludge production, inadequate treatment, and reagent usage. Due to its low cost, high removal efficiency, and simplicity of regeneration, adsorption is preferred as a suitable technique for removing dyes and heavy metal ions from contaminated water [31]. So, considerable efforts have been made to remove organic and inorganic aqueous contaminants using various adsorbents such as clay, activated carbon, biomass, biochar and other synthetic adsorbents. But recently, biochar-based nanocomposite, which has the advantages of biochar and nanoparticle, has received attention which removes pollutants from wastewater [32, 33]. The adsorption capacity of biochar nanocomposite varies based on the type of biomass used [34]. The yield and quality of biochar produced through pyrolysis depends on the percentage of cellulose, hemicellulose, and lignin in the biomass [35]. High lignin content in plant species produces more biochar at moderate temperatures [36]. Also, different metallic oxides result in varying adsorption capacities in biochar-nanomaterial compositions.

Literature shows that different biochar-based nanocomposites have been applied for water treatment [32]. However, to the best of our knowledge there is no reported result in using manganese oxide and magnetic iron oxide nanocomposites of coffee husk and khat leftover biochar for the removal of synthetic dyes and heavy metals from water. Hence, this research is concerned with synthesizing various alternative biochar-based nanocomposite material adsorbents from coffee husk and khat leftovers.

This study was carried out to assess the conversion of khat leftover and coffee husk into valuable goods with dual benefits. These include removal of hazardous contaminants from water and economically discarding biomass wastes. The manganese oxide coffee husk biochar nanocomposite (MnOx-CHBNC), manganese oxide khat leftover biochar nanocomposite (MnOx-KLBNC), magnetic iron oxide-coffee husk biochar nanocomposite (Fe_3O_4-CHBNC), and magnetic iron oxide-khat leftover biochar nanocomposite (Fe_3O_4-KLBNC) were produced, characterized and their MB and hexavalent chromium (Cr(VI)) removal efficiencies were determined. The study examined the effects of contact time, adsorbent dosage, concentration, and pH on the adsorption capacities of adsorbents for MB and Cr(VI) and evaluated their kinetics and adsorption isotherms. Furthermore, tests on regeneration were carried out to evaluate the adsorbents' potential for reuse.

1.2. Statement of the Problem

Currently, the volume of discharging wastes containing heavy metals and synthetic dyes has increased. This is because of rapid population growth, urbanization, industrialization, and agricultural activities. These toxic contaminants enter the ecosystem by discharging untreated or partially treated industrial effluents, accumulating for a long time without degradation. They contaminate plants, and animals through various mechanisms, and thus, can directly or indirectly be consumed by a human being through food, water, and air, which may cause non-reversible health problems [37].

For instance, the United States Environmental Protection Agency (US EPA) lists chromium as a priority contaminant and is one of the most common heavy metals in the environment [21]. There are two naturally occurring types of chromium: Cr(III) and Cr(VI). Cr(VI) is more toxic, soluble, and mobile than Cr(III). It suggests that Cr(VI) can seep into groundwater and can easily be absorbed by aquatic plants, leading to adverse impacts on human health [22]. Also, MB is an organic dye commonly used for coloring paper, printing cotton, and dyeing leather and plastics [12, 14, 15]. Frequent and prolonged contact with MB can cause tissue necrosis, cyanosis, and also threats to marine life [13]. Hence, using suitable treatment methods before discharging industrial emissions into the environment is a vital issue.

Various physical and chemical methods such as ultrafiltration [38, 39], electrochemical [25], ion exchange [26], photo-catalytic, chemical precipitation [40, 41], coagulation [42], degradation [27, 28], electrochemical degradation [43] and adsorption [29, 30] have been used for removal of heavy metals and dyes from industrial effluents [12, 32, 44–46]. Nevertheless, a number of these techniques come with built-in drawbacks, including excessive energy usage, expense, the production of hazardous sludge, insufficient treatment, and reagent consumption [7, 47, 48]. Because of its low cost, high removal efficiency, and simplicity of regeneration, adsorption is one of the most effective processes currently available for removing heavy metal ions and synthetic dyes from contaminated water [31].

Considerable efforts have been made to remove organic and inorganic aqueous contaminants using various adsorbents such as clay, activated carbon, biomass, biochar and other synthetic adsorbents, but recently, biochar-based nanocomposite, which has the

advantages of biochar and nanoparticle, has received attention which removes pollutants from wastewater [32, 33]. The adsorption capacity of biochar nanocomposites varies from one adsorbate to another. The percentage of cellulose, hemicellulose, and lignin in the biomasses determine the amounts of pyrolysis product, biochar. Plant species with high lignin content produce a larger biochar yield when pyrolyzed at moderate temperature [36]. Also, the characteristics of the biochar products is affected by a set of parameters, such as temperature, residence pressure, size of the biomass, and residence time during pyrolysis [49, 50]. Moreover, different metallic oxides form variable metal-organic frameworks in the biochar-nanomaterial compositions, and due to this reason, the materials have different adsorption capacities.

This research aims to synthesize biochar-based nanocomposite material adsorbents from coffee husks and khat leftovers. Because, coffee husk and khat leftover taking larger part of environmental pollution in Ethiopia, they are chosen for this study. Coffee and khat are widely produced and consumed in Ethiopia, which results in large amounts of biomass waste that contaminates the environment [51, 52]. Agriculture contributes to over 70% of Ethiopia's population and 36.3% of its gross domestic product (GDP). The coffee and khat industries are leading sectors for export trading. However, the production of coffee and khat generates large amounts of biomass waste rich in organic matter, nitrogen, and phosphorus [53, 54]. Disposing of these byproducts in water bodies leads to environmental pollution, causing damage to aquatic ecosystems and hindering soil fertility. Burning coffee husks releases harmful pollutants into the atmosphere and discarding khat wastes results in visual pollution, attracts disease-carrying vectors, and creates breeding grounds for pathogens. Furthermore, unattended coffee husk and khat leftover disposal increases municipal waste, which raises transportation expenses when brought to the disposal site [55]. Therefore, it is crucial to remove this biomass waste safely.

1.3. Objectives of the Study

1.3.1. General objective

The main objective of this study was to study the potential preparation of biochar-based nanocomposites from biomasses (CH and KL) for the removal of MB and Cr(VI) from water.

1.3.2. Specific objectives

The specific objectives of this study were:

- To prepare MnOx-CHBNC and MnOx-KLBNC for the removal of methylene blue from water.
- To evaluate the removal efficiency of MnOx-CHBNC and MnOx-KLBNC for Cr(VI) from water.
- To prepare Fe_3O_4-CHBNC, and Fe_3O_4-KLBNC for removal of methylene blue from aqueous solution.
- To evaluate the removal efficiency of Fe_3O_4-CHBNC, and Fe_3O_4-KLBNC for Cr(VI) from water.

1.4. Significance of the study

Among the wastewater treatment methods adsorption using biochar-based nanocomposite is the cost-effective, environmentally friendly, and simple approach. Synthesizing the biochar nanocomposite adsorbent materials from coffee husk has dual benefits which are converting biomass waste into useful products. Therefore, findings of this study may play a significant role in promoting green methods for wastewater treatment and management of biomass wastes. Particularly, it may provide deeper insight into how carbon materials could be fabricated from cheaper biomass wastes like coffee husk and khat leftovers. Thus the study employed simple, fast, eco-friendly, low-cost material synthesis that resulted in reusable products. It may provide valuable information for those who work on biochar-based nanocomposites, biomass waste management, water treatment for removal of Cr(VI), and MB. In evaluating the significance of these findings, to the best of our knowledge we did not find reported studies about the removal of MB and Cr(VI) from water using MnOx and Fe_3O_4-activated CH and KL biochar nanocomposites (MnOx-

CHBNC, MnOx-KLBNC, Fe_3O_4-CHBNC, and Fe_3O_4-KLBNC). Thus, reporting these results offers several advantages, including:

- The products can be used as alternative adsorbents for the removal of MB and Cr(VI) from aqueous solutions.
- The production process of $KMnO_4$-activated biochar is faster, generates less ash content, is environmentally friendly, and reacts less with organic materials than other activation processes, even at room temperature [56, 57]. So, despite their removal efficiency, MnOx-CHBNC and MnOx-KLBNC are more ecologically friendly.
- Magnetic biochar nanocomposites are synthesized using two common agricultural residues, coffee husk, and khat waste. This process reduces the need for new materials and supports the recycling of waste, making it more sustainable and contributing to a circular economy.
- Given the advantages of MnOx-CHBNC, MnOx-KLBNC, Fe_3O_4-CHBNC and Fe_3O_4-KLBNC production, this document can serve as preliminary support for the scientific community interested in conducting studies to enhance the removal efficiency of toxic heavy metals and synthetic dyes using MnOx and Fe_3O_4 based CH and KL biochar nanocomposite.

1.5. Organization of the Dissertation

This dissertation contains eight chapters. The first chapter provides an introduction of the study, while the second chapter is a review of the literature. The third chapter presents experimental, including chemicals and reagents, instruments and equipment, experimental conditions and characterization techniques. The subsequent four chapters (chapters four to seven) presents the main findings of the studies. Chapter four describes the preparation and characterization of MnOx-CHBNC and MnOx-KLBNC for removal of MB from water. Chapter five presents the applications of MnOx-CHBNC and MnOx-KLBNC for removal of Cr(VI) from water. Chapter six describes preparation and characterization of Fe_3O_4-CHBNC and Fe_3O_4-KLBNC for the removal of MB from aqueous solutions; and the seventh chapter explains the applications of Fe_3O_4-CHBNC and Fe_3O_4-KLBNC for the removal of Cr(VI) from water. The general conclusions, recommendations and future prospective are presented in chapter eight.

CHAPTER TWO

2. LITERATURE REVIEW

2.1. Water Pollution and Toxic Effects of Heavy Metals

One of the most significant challenges that the world is currently facing is environmental contamination [58]. Due to urbanization, population growth, and rapid economic development across various sectors, including agriculture and industry, the environment is becoming increasingly polluted [59]. Various organic and inorganic toxic materials are continuously released into the soil and water ecosystems from natural and anthropogenic sources. Most environmental pollution originates from anthropogenic sources. Due to the presence of heavy metals like Cd, Cr, Pb and As in the particulate matter of emissions from industrial discharge, automobiles, and railway exhausts, these sources are prominent sources of heavy metal pollution [60]. Heavy metals play a major role in environmental pollution due to their toxic nature and potential for bioaccumulation in the food chain, despite being natural constituents of the environment [61]. The heavy metal elements make up a large part of the periodic table including metals and metalloids having densities greater than 5 g cm^{-3}. They are released into the environment mainly from anthropological activities such as industrial effluent, mining, domestic, commercial, agricultural activities, and natural sources from weathering of rocks [62].

Heavy metals like Fe, Zn, Mn, Cu, Co, and Ni are necessary for the growth and normal functions of both plants and animals in trace amounts, but when used for a longer time or at a larger concentration level, they may cause acute or chronic health effects [17]. For instance, if a larger amount of Fe is consumed, it may lead to health problems such as depression, rapid and shallow respiration, coma, convulsions, and cardiac arrest [63, 64]. Toxic doses of Co cause asthma, pneumonia, vomiting, vision problems, heart problems, thyroid damage, shortness of breath, cough, decreased pulmonary function, nodular fibrosis, permanent disability, and final death [65]. Exposure to water contaminated with Cu can lead to the cause of anemia, liver and kidney damage, diarrhea, abdominal pain, vomiting, headache, and nausea in children. Besides, zinc is a component of several enzymes (alkaline phosphatase, superoxide dismutase, alcohol dehydrogenase, carbonic anhydrase) in humans, but when taken at high concentrations, it can lead to a system disruption, which may result in growth and reproduction impairment. The clinical signs

of zinc toxicities include diarrhea, vomiting, icterus (yellow mucus membrane), bloody urine, anemia, kidney failure, and liver failure [66].

Heavy metals including Pb, Hg, Cd, Cr, and As are generally toxic metals [18]. They have chronic and acute health effects on human beings and other animals. For example, Cd is carcinogenic and has chronic health effects when accumulated in the liver and renal cortex. Overexposure to its high concentrations can cause acute kidney damage. Pb causes increased blood pressure, which is a significant risk factor for cardiovascular diseases and mortality [20].

Arsenic is another heavy metal that is prominently toxic and carcinogenic [19]. It is extensively available in the form of oxides or sulfides or as a salt of iron, sodium, calcium, copper, etc.[67]. Its inorganic forms such as arsenite and arsenate compounds are lethal to the environment and living creatures. The most common pathway for human exposure to arsenic is through drinking water, contaminated with arsenical pesticides, natural mineral deposits, or inappropriate disposal of arsenical chemicals. Its long-term exposure may cause lung, kidney, liver, and skin cancers. Generally, its acute and chronic poisoning causes skin lesions, loss of appetite, muscular weakness, diabetes, and gastrointestinal and cardiovascular diseases [68].

The toxicity of Hg depends on its compound types and chemical form [69]. Ingestion of inorganic forms of Hg causes spontaneous abortion, congenital malformation, and gastrointestinal disorders. Ingestion of its organic forms may lead to erethism, gingivitis, stomatitis, neurological disorders, central nervous system damage, acrodynia, and congenital malformation [70].

Chromium is the 21st most abundant element on earth. It naturally occurs in two valence states: hexavalent Cr(VI) and trivalent Cr(III) [71]. Cr(VI) is more soluble in water and 1000 fold high toxic than Cr(III) [72]. Generally, Cr(VI) was determined as highly toxic, mutagenic, and carcinogenic to human. High-reactivity intermediates like Cr(V) and Cr(IV), which can harm DNA, can be produced when Cr(VI) is reduced in cells [73]. Exposure to Cr(VI) compounds can lead to mutagenesis and cytotoxicity, potentially resulting in lung and sino-nasal cancer. It is reported that exposure to Cr causes health problems such as mouth ulcers, indigestion, acute tubular necrosis, vomiting, abdominal

pain, kidney failure, and even death [74, 75]. For human beings, the most common route of exposure to Cr is through contaminated water [76].

2.2. Toxic Effects of Dyes

Dyes are often used in heavy industries like textile, paper, and food processing to add color to their products. Unfortunately, when these dyes are released into water, they contribute to 20% of water pollution [9]. They are hazardous and harmful to the aquatic ecosystem, food chain, and public health. Dyes are dangerous and can harm the aquatic ecosystem, food chain, and public health. Even a small amount of dye in water can negatively impact its aesthetic value, reduce light penetration, and affect the gas solubility required for photosynthesis and respiration processes.

Worldwide, about 100,000 types of dyes are annually produced, and over 700,000 tones are utilized as a part of a few businesses [7]. MB, Malachite green, and Congo red are industrial dyes that are commonly used. MB is a cationic dye, and it is widely used for coloring paper, printing cotton, dyeing leather, as an indicator of oxidation-reduction reactions in analytical chemistry, and antiseptic. Short and prolonged contact with MB causes tissue necrosis, cyanosis, and heartbeat rise in humans and causes threats to marine life.

Malachite green is a type of dye that belongs to the triphenylmethane family. It contains an auxochrome group that gets protonated in water when the pH is low, resulting in a positive charge density (pKa = 10.3) [9]. Malachite green is used to dye various materials such as cotton, jute, paper, silk, wool, and leather. It is also used in fish farming to treat fungal, bacterial, and parasitic infections. However, despite its usefulness, this dye has adverse effects on both aquatic life and human health due to its toxic properties. Malachite green can cause damage to the liver, spleen, kidneys, and heart, as well as lesions in the skin, eyes, lungs, and bones. Additionally, it can have teratogenic effects on the brain and nervous system.

Congo red is an anionic dye with a pKa of 4.5 [9]. It is widely utilized in the textile, paper, rubber, and plastics sectors. In water, it produces a red colloidal solution and metabolizes to benzidine, a chemical known to be carcinogenic and mutagenic to aquatic life [7].

The presence of a very small amount of Azo dyes in water (<1 ppm) is highly significant [77]. This affects aesthetic merit, transparency, and water-gas solubility. Reducing light penetration through water decreases photosynthetic activity, causing oxygen deficiency and disturbing the biological cycles of aquatic biota. Azo dyes are aromatic compounds that cause a high potential health risk by adsorption and their breakdown products like toxic amines through the gastrointestinal tract, skin, and lungs and also the formation of hemoglobin adducts. Several Azo dyes cause damage to DNA that leads to malignant tumors [78]. Many Azo dyes are also highly poisonous to the ecosystem and mutagens, meaning they can have acute to chronic effects upon organisms, depending on the exposure time and Azo dye concentration.

2.3. Environmental Pollution by Coffee Husk and Khat Leftover in Ethiopia

Agriculture is one of the dominant sectors in the Ethiopian economy and its share of gross domestic product (GDP) is 36.3% and above 70% of Ethiopia's population is employed in the sector. The coffee and khat industries are the leading agricultural sectors for export trading [51, 52, 79]. Coffee and khat are widely produced for export and local consumption and the process results in large amounts of biomass waste. According to a report by Dadi and coworkers, the dry processing of coffee beans results in approximately a kilogram of husk being generated from the production of each kilogram of coffee beans produced [80]. Due to their high demand, wet coffee processing plants are usually built near rivers or other water sources [81]. After the coffee is harvested, various byproducts such as coffee pulp, husk, silver skin, and spent coffee grounds are generated. These byproducts of coffee contains tannins, caffeine, and polyphenols [55, 82, 83].

Generally, coffee husks and khat leftovers are rich in organic matter, nitrogen, and phosphorus [53, 54]. Disposing of these byproducts in water bodies leads to environmental pollution, causing damage to aquatic ecosystems. This is due to the promotion of algae and aquatic plant growth, depletion of oxygen levels, eutrophication and chemical contents that can be toxic to aquatic life. Large-scale dumping of coffee husks and khat leftovers can lead to nutrient imbalances, hinder plant growth and soil fertility, and increase soil acidity [84]. Burning coffee husks releases harmful pollutants into the atmosphere, contributing to air pollution and respiratory problems. Coffee husks left to decompose in landfills emit methane, which is a potent greenhouse gas that contributes to climate change [81, 85]. Also, discarding khat wastes in open dumpsites,

results in visual pollution, attracts disease-carrying vectors, and creates breeding grounds for pathogens. Khat leftovers are sometimes littered on the streets, degrading the environment and potentially blocking drainage systems [86, 87]. Therefore this biomass wastes should be removed safely.

2.4. Removal of Heavy Metals and Dyes

The presence of elevated concentrations of inorganic and organic contaminants in water bodies is considered a serious global issue [88]. As mentioned earlier, they enter the aquatic environment through effluents from industries, such as mining, textile, dyeing and tanning, and electroplating causing different environmental risks and human health problems. As a result, it is critical to apply suitable treatment methods before discharging industrial effluents into the environment. Various techniques, such as physical, chemical, and biological methods like electrochemical, filtration, reverse osmosis, ion exchange, chemical precipitation, adsorption, and coagulation, have been used to remove dyes and heavy metals from wastewater [44]. However, each approach has inherent drawbacks, such as high energy consumption, expense, the production of hazardous sludge, partial treatment, and excessive reagent usage [7]. Amongst the current methods, adsorption is particularly attractive for the removal of organic and inorganic pollutants. It is a cheap, eco-friendly, and efficient method.

Various reports indicate that the effectiveness of removing heavy metals and synthetic dyes by adsorption is mostly determined by the absorbent materials used [89]. Inorganic and organic pollutants in water have been removed using adsorbents such as activated carbon, natural clay minerals, synthetic inorganic materials, synthetic nanoparticles, and biomass [10]. However, recently attention has been given to investigating some alternative low-cost materials that are efficient and selective in removing toxic heavy metals and dyes from wastewater. Activated carbon is an ideal adsorbent to remove contaminants from water, but its preparation and raw materials are tedious and expensive. Biochar, which requires relatively, less investment, has been used as an alternative adsorbent [90].

Biochar is a high-carbon material with oxygen functional groups and large surface areas obtained by pyrolysis of organic feedstock in the absence or partial supply of oxygen [33]. More hydrogen and oxygen remain in its structure along with the ash originating

from the biomass is used for adsorption. Biochar is widely applied to remove heavy metals and dyes from wastewater. For instance, biochars prepared from different materials such as *Onopordom heteracanthom* were used for removal of Cr [VI] and MB [91], rice straw for removal of cationic dye [29], beli (*Aegle Marmelos*) fruit shell for removal of MB [92], palm kernel shell for removal of crystal violet [93], spent coffee ground for removal of Cd, Mn and Pb [94], hardwood and corn straw for removal of Cu and Zn [95], sago stems for Cd, Hg, Cu, and Pb [96], rice husks, olive pomace and orange waste for removal of Cu(II) [97].

However, the adsorption capacity of pristine biochar is limited. So it is important to modify it by composing it with nanomaterials to enhance its adsorption capacity [98]. That is, organic and inorganic materials synthesized at the nano-scale have better efficiency and selectivity to remove effectively heavy metals and dyes from aqueous solutions. Nanomaterials have a large surface area making them suitable for maximum adsorption. Metallic oxide nanomaterials, including magnetic ferric oxide, manganese oxide, titanium oxide, magnesium oxide, and others, have been studied for application in wastewater treatment [99]. However, aggregation of nanoparticles is a serious issue. Thus, it is important to provide support favoring the stability and recyclability of the adsorbent. These days, considerable efforts are exerted in using biochar-based nanocomposite materials to remove contaminants from aqueous samples. The biochar-based nanocomposite integrates the benefits of both biochar and nanomaterials, producing a composite material with enhanced properties [32].

2.5. Preparation of Biochar

Heating biomass such as wood, manure, and agricultural leftovers, with little or no oxygen via pyrolysis or charring, produces biochar [100]. It is carbon-rich and porous with oxygen functional groups and aromatic surfaces. It has different physical and chemical properties depending on the feedstock and pyrolysis technology. Studies revealed that the feed-stocks' virgin resources and residuals such as wood, coffee husk, rice straw, tea waste, and wheat straw are highly potential precursors to produce biochar [101–103].

Biomass mainly contains lignin, cellulose, and hemicellulose [35]. During preparation, the proportion of cellulose, hemicellulose, and lignin content determines the ratios of bio-

oil, gas, and biochar products [36]. Palma reviewed that biomass decomposes according to the following four stages: at temperatures < 220 ℃, the moisture evaporated; at 220–315 ℃, predominantly hemicellulose decomposition occurred; at 315–400 ℃, cellulose decomposition was observed; and at > 400 ℃, mainly lignin decomposed [104]. Similarly, the thermo-gravimetric analysis (TGA) of the activated biochar of Khat reported by Kumari and coworkers revealed that the first mass decomposition occurred nearby at 100 ℃due to physically absorbed water desorption. The evaporation of a small number of volatile compounds may also contribute to weight loss. The second stage is mass loss at 300 ℃, due to the decomposition of cellulose, hemicelluloses, or lignin degradation. Third-stage decomposition followed between 350 and 600 ℃ due to the burning of carbonaceous residues [52, 105]. However, different decomposition pattern was observed based on weight losses during TGA for different types of biomass [104].

It is well established that gasification comprises sequential steps: pre-heating for drying, pyrolysis, char gasification, and oxidation. The pyrolysis step takes place at 200–500 ℃, where the fuel decomposes into three often lumped products: char, volatiles (condensable hydrocarbon or tar), and gases (non-condensable) [106]. Also, Celso and Rapagna reported that the pyrolysis results of wood are gas, tar, and char yields, which are found to be influenced by the method of feed introduction, the bed temperature, fluidizing gas composition, and wood particle diameter [107].

Therefore, the choice of the feed-stocks and pyrolysis conditions will be determined by the desired balance between the pyrolysis products (biochar, bio-oil, gas). For instance, high lignin-containing feed stocks generally produce the highest biochar yield when pyrolyzed at moderate temperatures (ca. 500 ℃). The characteristics of the biochar product are heavily affected by the extent of pyrolysis (temperature and residence pressure) and entirely by biomass size and kiln or furnace residence time [49].

Pyrolysis techniques can be distinguished, by parameters, including the residence time, temperature, the pyrolysis material, pressure, size of adsorbent, heating rate, and method [108]. For example, based on the reaction temperature, it can be classified as high-temperature hydrothermal synthesis (180–300 ℃), flash carbonization (300–600 ℃), and anoxic (400–900 ℃). The temperature during pyrolysis can affect both biochar output and surface characteristics. At higher pyrolysis temperatures, the amount of biochar and

the number of acidic functional group (-COOH) decreased, whereas the alkaline functional groups, ash content, and pH increased.

Generally, the pyrolysis process is slow pyrolysis (SP) or fast pyrolysis (FP) [34]. SP is slow heating (minute to hours) of the organic material in the oxygen-depleted atmosphere and relatively long solids and gas residence times [109]. Liquid and solid products of the SP process are char, bio-oil, and syngas. SP is the most effective process to produce a typical biochar yield of 35.0% from dry biomass weight. The FP is the most efficient method for producing biofuels, and gasification is the most efficient for producing syngas and hence is usually used to generate heat and energy. Biochar yield and its physicochemical properties widely depend on the reactor type or design and operating parameters of pyrolysis [50].

Hence, the biomasses such as Khat (*Catha edulis*) leftover and coffee husk give a higher quantity of biochar. As summarized in Table 2.1, studies have revealed that they contain a higher portion of cellulose, hemicellulose, and lignin [110–115]. For example, Oliviera conducted a characterization study on coffee from Brazil (*Coffea arabica*) husk and reported that coffee husk is a by-product from coffee processing that contains a very high amount of lignin, while the compositions of cellulose, hemicellulose, and lignin are 26.5, 25.5 and 33.5% respectively [113].

Table 2.1. Cellulose, hemicellulose, and lignin content of coffee husk and Khat.

Biomass and its origin	Cellulose Wt.%	Hemicellulose wt.%	Lignin wt.%	Ref.
Coffee husk (Ethiopia-Addis Ababa)	35.5	14.8	30.7	[112]
Coffee husk (*C. arabica* from Brazil)	26.5	25.5	33.5	[113]
Coffee husk (*C. arabica* from Ethiopia Mettu)			71.2	[114]
Khat waste (Ethiopia-Addis Ababa)	39.4	12.8	28.7	[115]

2.6. Interaction of Biochar with MB and Cr(VI) in the Aqueous Solution

The two main characteristics of biochar explain the removal of MB and Cr(VI) from an aqueous solution [116]. Firstly, biochar has a highly porous structure, with microscopic pores and cavities that act as tiny traps for MB molecules and ions containing Cr(VI). The surface area of these pores is crucial, as higher surface area biochar generally exhibits

greater adsorption capacity. Secondly, the surface chemistry of biochar plays a significant role. Biochar can have functional groups, such as carboxylic and phenolic groups, on its surface that can interact with MB molecules through various mechanisms. MB is a cationic dye which carries a positive charge. Depending on the pH, biochar surfaces can be negatively charged, creating an electrostatic attraction between the positive MB molecule and the negative biochar surface, promoting adsorption [117]. Essentially the high surface area, with its intricate network of pores provides ample space for MB molecules to accumulate. Also, the surface functionalities like charged groups act as binding sites for the MB molecules to adhere. Some studies suggest that physical adsorption (binding through weak van der Waals forces) and chemical adsorption (stronger covalent bonding) can be involved in the MB-biochar interaction, with the latter potentially playing a dominant role [118].

The interaction of biochar with Cr(VI) is a bit different from MB adsorption [119]. The primary mechanism for Cr(VI) removal by biochar is a reduction of redox groups on the biochar surface. This process converts the toxic Cr(VI) to the less harmful Cr(III) [120]. Additionally, complexation with functional groups can occur, further immobilizing Cr(VI) within the biochar matrix. Biochar surfaces may have oxygen-containing groups like carboxylic and hydroxyl groups. These can form complexes with Cr(VI) ions, immobilizing them within the biochar structure. The porosity still plays a role. Pores allow Cr(VI) ions to penetrate the biochar and access the active functional groups mentioned above [121].

2.7. Preparation of Biochar Based Nanocomposites

Biochar contains higher oxygenated surface functional groups (phenolic, carboxylic, carbonyl) and fixed carbon than biomass. Hence, it could be used as a catalyst, adsorbent, and carbon electrode [36]. Biochar has a relatively low specific surface area, deprived porosity, and lean surface functional group. Its applications are limited. Because it has a lower specific surface area and porosity, but the surface area and adsorption capacity will increase by activation. The activation by either physical or chemical processes increases the specific surface area and pore density of the biochar [32].

2.7.1. Physical activation

Physical activation or thermal activation is a method in which the porosity of biochar increases by high temperature. At high temperatures (ca. 700–900 °C), the char produced is auto-gasified due to the presence of steam, carbon dioxide, etc.[50]. It is a dual-stage process, that features the carbonization stage in the presence of an inert gas (N_2 or Ar) followed by the activation stage with the aid of an oxidizing gas (O_2, CO_2, H_2O steam) in the temperature range of 800–1200 °C. This loss of mass in the form of gas and other volatiles makes the biochar product more porous. In this activation process, the nitrogen gas and carbon dioxide generated can be used to produce more pores in the biochar [100, 122]. The advantages of physical activation are its clean, green production deprived of any secondary waste disposals compared to chemical activation. However, the disadvantages of physical activation are associated with its high activation temperature, considerably long processing time, relatively low carbon yield, and poor specific surface area.

2.7.2. Chemical activation

During chemical activation, biochar is impregnated with chemical agents [123]. In the chemical activation process, many chemical reagents have been used as activating agents. Activating agents can be classified into acidic, alkaline, neutral, and self-activating agents. Different types of activating agents react with cellulose, hemicellulose, lignin, or polysaccharide in carbon precursor, leading to various activation mechanisms. The porous structure of activated biochar is developed through the synergistic effect of pore formation, pore expansion, pore combination, and pore collapse.

For example, Wu and coworkers have synthesized sawdust biochar/Ag/Fe nanocomposite, conducted SEM analysis of the original biochar, modified biochar (MB), fresh sawdust biochar/Ag/Fe composite (Ag/FeMB), and used sawdust biochar/Ag/Fe composite (Ag/FeMBCX) [124]. The result presented in Figure 2.1 showed that the SEM images of OB, MB, fresh Ag/Fe/MB, and used Ag/Fe/MB. The modified biochar (Figure 2.1b), with abundant micro-pores formed on the surface, is rougher surface than the original biochar (Figure 2.1a). Some well-distributed globular structures formed on the biochar are due to the impregnated Ag/Fe nanoparticles (Figure 2.1c). Figure 2.1d shows

that the size of the Ag/Fe nanoparticles increased a lot after CLX adsorption, due to the formation of iron hydroxides or oxide layer on the surface of Ag/Fe.

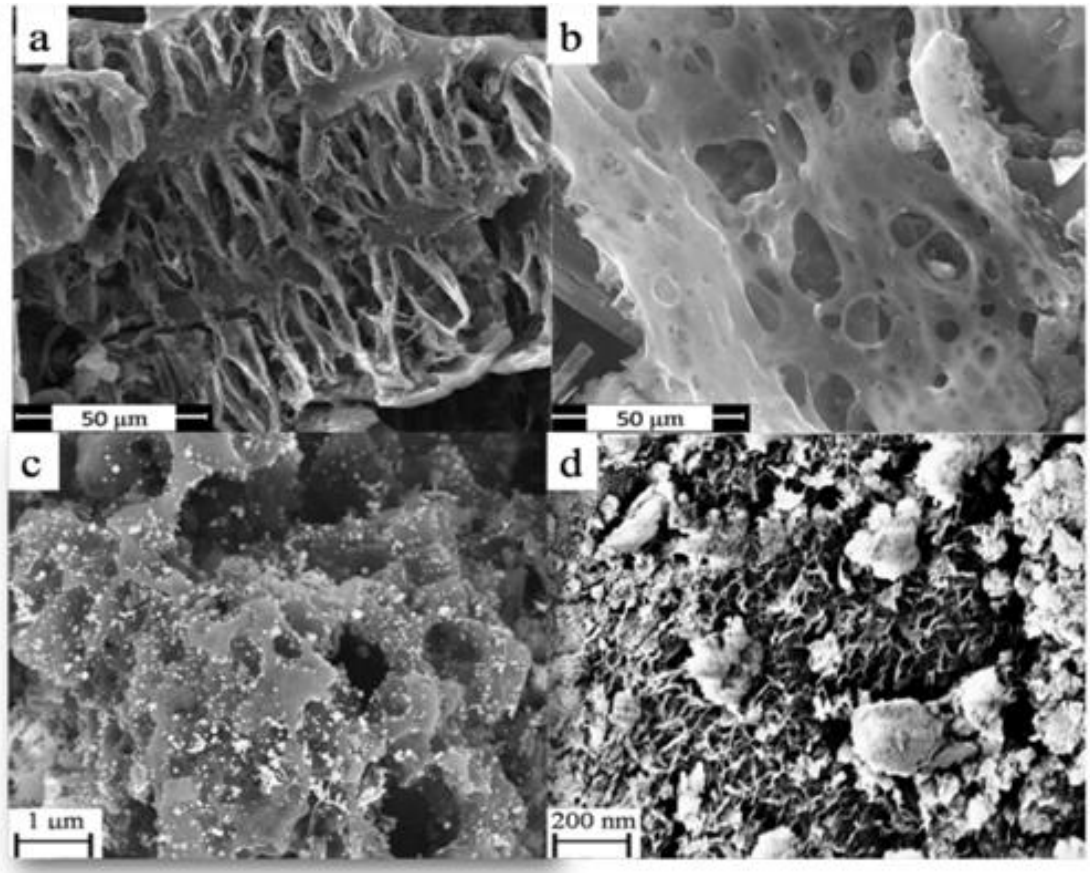

Figure 2.1. SEM images of (a) OB (b) MB, (c) fresh Ag/Fe/MB and (d) used Ag/Fe/MB [124].

2.7.2.1. Acid activated biochars

Acid-activated biochars are synthesized by treating the feed-stocks with acids such as hydrochloric acid, nitric acid, sulfuric acid, phosphoric acid, etc.[122]. The acid modification aimed mainly to introduce acid functional groups on the surface of biochar [123]. Peng and coworkers reported that biochar of reed activated by 1M hydrochloric acid, is enriched with hydrophobic adsorption site to remove pentachlorophenol [125]. Also, Mahmoud reported that, when kenaf fiber biochar is treated with hydrochloric acid, there is an increase in surface area from 289.5 to 346 m^2 g^{-1} [126].

2.7.2.2. Alkaline activated biochars

Alkaline activated biochar is synthesized by treating the feed-stocks with strong bases like sodium hydroxide, potassium hydroxide [103, 127, 128], medium alkaline such as potassium carbonate [129, 130] and sodium carbonate [131], and weak alkaline is known as salts of a strong base and weak acids such as potassium silicate, sodium silicate, potassium acetate, etc. Alkaline modification is suitable to increase the surface area and oxygen-containing functional groups on the surface of biochar. In comparison with other alkaline activating agents, potassium hydroxide is the most effective to prepare activated biochar with a very high specific surface area. Hence reported work show that KOH can suppress the generation of tar, lower the temperature of pyrolysis, speed up the elimination of non-carbon constituents, and increase the rate of pyrolysis [132].

For example, Chen and coworkers reported that KOH can react with oxygen-containing species in the biomass, which is the main reaction at the lower ratios of KOH: biomass (1:8-1:2) or lower temperatures (400-600℃). In the reaction, KOH is completely changed to K_2CO_3, releasing a large amount of gaseous products and phenols. However, at higher ratios (>1:2) or a higher temperature (700-800℃), there is a significant decrease in the concentration of phenols and oxygen-containing species, and the hydrocarbons become the dominant species. Also, this reaction generated an abundance of pores in the biochar that are rapidly occupied by OH^- from KOH forming a large number of oxygen-containing groups such as C=O, –OH, C–O, and –COOH. This increases the oxygen content in the biochar. Generally, the study revealed that at higher temperatures, the reaction between KOH and biomass was significantly enhanced along with a sharp increase in the specific surface area and the oxygen-containing groups further transformed into more stable –OH, C–O, and –COOH groups [133].

Similarly, Bag and coworkers reported that Oak wood samples were converted into activated biochar by chemical activation with KOH [134]. The study revealed that the yield of activated carbon decreases with increased temperature and a higher ratio of KOH to biomass. However, the highest surface area of activated biochar was obtained 1662 m^2 g^{-1} at the highest temperature of 800℃ with 50% wt. KOH concentration.

2.7.2.3. Neutral activated biochars

Metal salts often used to activate biochars include $CaCl_2$, $MgCl_2$, $KMnO_4$, $AlCl_3$, $MnCl_2$, $TiCl_4$, and $ZnCl_2$. This activation process produces nanoparticles such as CaO, MgO, MnOx, Al_2O_3, AlOOH, TiO_2, and ZnO on the biochar surface [36]. The majority of biochar nanocomposites are prepared via chemical treatment with metallic ions. This preparation can be completed in a single or two-step activation approach [32]. As it is described in Figure 2.2, in a single step process, both activation and carbonization are completed concurrently. In contrast, a two-step method involves carbonizing the biomass feedstock first and then activating it with the required chemical. Metal ions required for activation bind to the surface or penetrate the biomass interior when impregnated with metal ion salt solutions. During pyrolysis, the metal ions are converted into nano-metal oxides or metal hydroxides, producing biochar-based nanocomposites [99].

2.7.2.4. Magnetic biochar-nanocomposites

Magnetic biochar-based adsorbent can be prepared by the pyrolysis of iron ion (Fe^{3+}/Fe^{2+}) treated biomass [135]. In this process nano-sized iron oxides including Fe_3O_4 and γ-Fe_2O_3 can be impregnated into the biochar, resulting in the introduction of magnetism and active sites of iron oxide to remove contaminants from water. Introducing magnetic medium to the biochar through chemical co-precipitation is an efficient method to enable the sorbent to be successfully removed by magnetic separation technique [136].

As it is mentioned above, biochar nanocomposites are commonly synthesized by chemical co-precipitation of biomass before pyrolysis (through a single step) and chemical treatment of biochars after pyrolysis (through two steps). However, Ali and coworkers conducted a comparative study between these two methods that revealed co-precipitation of iron oxides onto the biomass before pyrolysis have better Fe_3O_4 content, magnetization, thermal stability, and As(III and V) adsorption efficiency than the magnetic biochar synthesized through two steps [137]. Also, Mubarak and coworkers reported that novel magnetic biochar was synthesized by single stage microwave heating technique, by treating empty palm fruit bunch with $FeCl_3.6H_2O$ [138]. In this specific study, the analysis revealed that optimum conditions for the high porosity magnetic bio-char production were at 900 W microwave power, 20 min radiation time, and 0.5 ($FeCl_3$: biomass) impregnation ratio. This newly produced magnetic bio-char has a high surface

area of 890 m^2 g^{-1}. Figure 2.2 represents the schematic diagram of synthesizing biochar-based nano-composites.

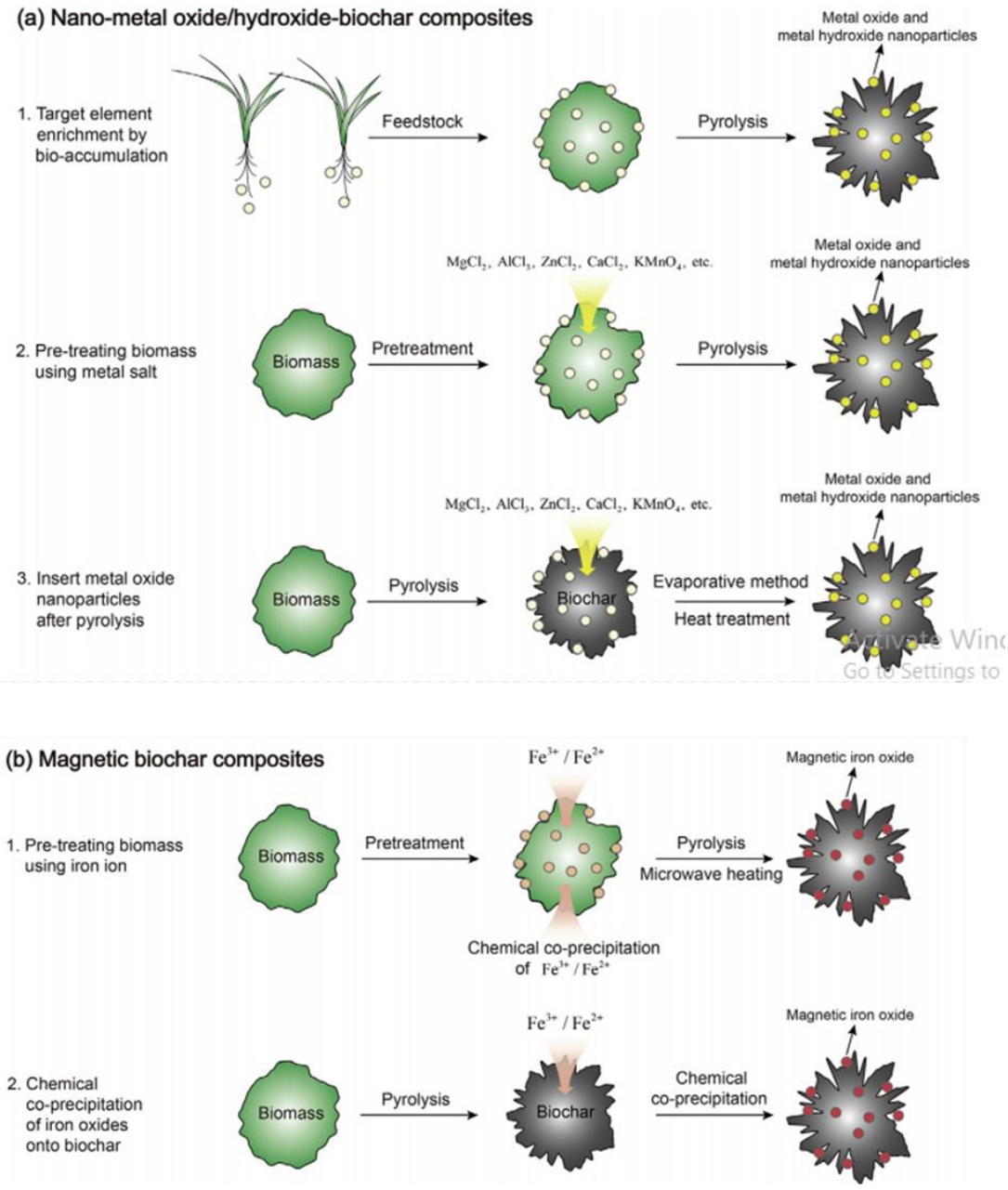

Figure 2.2. The schematic diagram of synthesizing biochar-based nano-composites [32]**.**

2.8. Characterization of biochar-nanocomposites

Biochars have diverse chemical compositions and structures, leading to many methods to enhance their functionalities for pollution treatment [100]. Modification techniques like pre-treating biomass and chemical modification of biochar surface produce biochar-based

nanocomposite materials [49]. Hence, different characterization techniques are used to determine the qualitative and quantitative properties of biochar-nanocomposite materials. Some of the characterization techniques and their uses are as follows.

2.8.1. Fourier Transform Infrared Spectroscopy Studies

Fourier transform infrared (FTIR) spectroscopy is used to investigate the changes in structure and the functional groups found in the nanocomposite materials at different synthesizing conditions [10, 49, 139, 140]. For example, Mohan and coworkers reported that the FTIR spectroscopy analysis of biochar-nanocomposite synthesized through fast pyrolysis of oak wood and bark treated with Fe^{2+}/Fe^{3+} /NaOH solution [141]. The result shows that both magnetic biochars exhibited similar spectra. Sharp band absorptions at 2325 and 2355 cm^{-1} attributed to bond vibration modes in goethite ($Fe_2O_3.H_2O$). After being treated with Fe^{2+}/Fe^{3+} /NaOH, the FTIR spectra of oak wood and bark biochars showed new bands that were not present before. The magnetic oak bark biochar (MOBBC) and magnetic oak wood biochar (MOWBC) showed peaks at 3751 and 3446 cm^{-1}, which can be attributed to both free and H-bonded -OH stretching vibrations caused by alcoholic or phenolic functional groups. In the range 1800-1685 cm^{-1}, the peaks indicated C=O stretching vibrations due to ketones, esters, carboxylic acids, and anhydrides.

Similarly, Shams and coworkers employed FTIR spectroscopy analysis in comparison research to explore the influence of techniques of preparation on magnetic Kan's grass biochar for increased As (III, V) removal from aqueous solution [137]. In the study, magnetic Kan's grass biochars (MKGBs) were synthesized through four different methods by single-step and two-step procedures at residence times of 2 and 4 h, but other conditions were constant for all. Biochars were prepared from Kans grass using two methods: pyrolysis followed by treatment with Fe^{+2}/Fe^{+3}/NaOH to prepare biochars $MKGBC_1$ and $MKGBC_2$ and a single-step process using Fe^{+2}/Fe^{+3}/NaOH followed by pyrolysis to produce magnetic biochars MKGBC3 and MKGBC4. FTIR spectroscopic analysis revealed various functional groups in the Fe_3O_4/biochar composites, including organic residues such as aromatic C–C bonding in lignin, polysaccharide, fatty acid, polymeric CH_2, and hydroxyl. The peaks around 1057 and 3400 cm^{-1} represent the stretching mode of C–O–C and –OH, respectively, which were either reduced or eliminated in MKBC3 and MKBC4 (Figure 2.3).

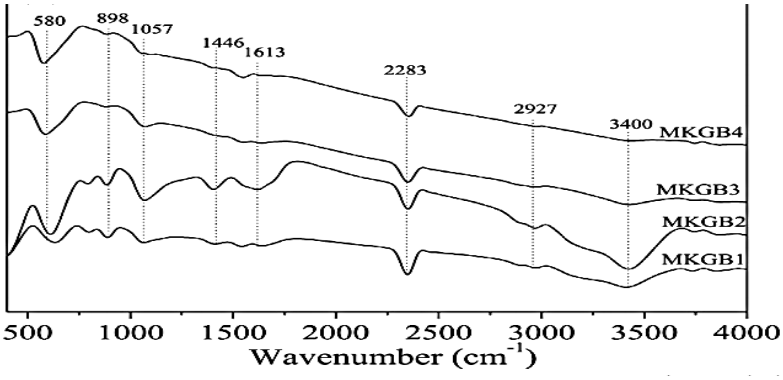

Figure 2.3. FTIR spectra of $MKGB_1$, $MKGB_2$, $MKGB_3$, and $MKGB_4$ [137]**.**

2.8.2. Measuring specific surface area

Specific surface area (SSA) is a term used to describe the physical properties of solid substances such as catalysts, pigments, polymers, cement, and adsorbents [142]. The pores in these substances are classified into three categories based on their diameter. Micropores are pores with a diameter less than 2 nm, mesopores lie between 2 to 50 nm, and macropores are pores with a diameter exceeding 50 nm. Micropores can be further divided into different subcategories based on their size. Ultra-micropores are pores with a diameter of less than 0.7 nm, medium-sized micropores have a diameter between 0.7 nm and 0.9 nm, and super-micropores have a diameter greater than 0.9 nm. The Brunauer-Emmett Teller theory (BET) is a widely used technique to determine SSA. It is an extension of the Langmuir monolayer molecular adsorption model to multilayers [49]. To determine the BET, an equilibrium adsorption isotherm is measured at the boiling point of the adsorbate, such as nitrogen (N_2) and argon (Ar), at 77 K and 87 K, respectively. Nitrogen is commonly used as the gas adsorbate because it is inert, widely available, inexpensive, and interacts with most solids.

The N_2 physisorption analyzer has two main components - the degassing and adsorption stations [142]. First, the quartz cell for gas adsorption is calibrated, then evacuated under high vacuum at 300 ℃ for 2 h (degassing), followed by a complete adsorption cycle in the empty cell at 77 K. Next, 50-150 mg of the sample is loaded into the cell and connected to the degassing station to remove physically adsorbed water and other volatiles that accumulate during storage. The cell is then transferred to the adsorption station after degassing, where adsorbate gas is incrementally introduced through the calibration volume (CAL), and the difference between the measured pressure and that of

the empty cell correlates with moles of adsorbed nitrogen. Table 2.2 provides examples of BET applications.

The data in Table 2.2 shows that the specific surface and pore volumes of Fe_3O_4/C nanocomposite are higher than that of pure Fe_3O_4 nanoparticles [129]. The specific surface area and pore volumes of lentil waste biochars activated with K_2CO_3 at various temperatures and impregnation ratios are different. Generally, as the impregnation ratio is kept constant, the specific surface area and pore volumes of biochar nanocomposite decrease with increasing pyrolysis temperature [129, 136].

Table 2.2. Some applications of BET.

Name of the nanoparticle or biochar-nanocomposite		**Result of BET analysis**			**Ref.**
		SSA ($m^2.g^{-1}$)	**Pore volume ($cm^3.g^{-1}$)**	**Pore diameter (nm)**	
Fe_3O_4 nanoparticles	Fe_3O_4	7.08	0.013		[10]
Fe_3O_4/C nanocomposite	Fe_3O_4/C	26.13	0.023		
Lentil waste/K_2CO_3	LWC381	1875	0.995	1.97	[129]
	LWC391	1766	0.936	2.24	
Orange peel/ γFe_2O_3	MOP250	41.2	0.0522	5	[136]
	MOP400	23.4	0.0425	7.2	
	MOP700	19.4	0.0329	6.8	
Kans grass biochar/ γFe_2O_3	MKGB1	38.22	0.1869	18.57	[137]
	MKGB2	31.16	0.1075	16.37	
	MKGB3	27.90	0.1144	14.80	
	MKGB4	31.45	0.1771	21.96	
Palm oil empty fruit bunch/γFe_2O_3		890		2	[138]
Pine-wood and Pine-wood bark biochar/ γFe_2O_3	PWB	209.6			[143]
	PWBM	193.1			
Hickory wood chip biochar/MgO	HC	249.7	0.112		[144]
	MHC	310.7	0.140		

2.8.3. Scanning electron microscopy and Transmission electron microscopy

Electron microscopes, such as scanning electron microscopy (SEM) and transmission electron microscopy (TEM), are incredibly useful for examining nanoparticles. They allow us to determine the structure and size of these tiny particles [145]. SEM can magnify the object up to 100,000 times, which helps us study the micro-structure of solid surfaces and analyze the internal structure of materials [146]. SEM is better suited for larger nanoparticles, with diameters greater than 50 nm, and has a detection limit of 1 nm. On the other hand, TEM is more accurate for smaller particles with diameters greater than 0.1 nm [147].

SEM and TEM are widely applicable in the characterization of biochar nanocomposite materials. For example, Wang and coworkers conducted a study on maize straw/Ce^{3+} biochar nanocomposite for phosphate adsorption [148]. The reported SEM and TEM analysis results on the comparative characterization of biochar nanocomposite before and after adsorption showed a different arrangement of particles. Also, the study revealed the effect of pH on the structure.

Similarly, Wu and coworkers have synthesized sawdust biochar/Ag/Fe nanocomposite, conducted SEM analysis of the original biochar, modified biochar (MB), fresh sawdust biochar/Ag/Fe composite (Ag/FeMB), and used sawdust biochar/Ag/Fe composite (Ag/FeMBCX) [124]. The modified biochar, with abundant micro-pores formed on the surface, is a rougher surface than the original biochar. Some well-distributed globular structures formed on the biochar are due to the impregnated Ag/Fe nanoparticles. The size of the Ag/Fe nanoparticles increased a lot after CLX-adsorption due to the formation of iron hydroxides or oxide layers on the surface of Ag/Fe [124, 148]**.**

2.8.4. X-ray diffraction spectroscopy

Diffraction is a phenomenon that occurs when a beam of electromagnetic waves, with a wavelength comparable to the distance between atoms, interacts with the periodic arrangement of molecules in a crystal [149]. This interaction results in constructive interference at a specific angle, which is used to gather information about the atomic arrangement in the crystal. The incident beams, which typically have wavelengths of around 0.1 nm, are generated by x-ray sources (photons), electron guns (electrons), and

nuclear reactors (neutrons). X-ray diffraction (XRD) is the most commonly used method for this purpose [150]. In contrast, amorphous materials like glass lack a periodic arrangement. Therefore, it could not produce any significant peak in the diffraction pattern. XRD is an effective and convenient means of characterizing crystal parameters and reflecting changes in surface elemental composition and elemental species [151, 152].

For instance, XRD spectroscopy is suitable and highly applicable for the characterization of biochar nanocomposite materials. Table 2.3 summarizes some of the examples for applications of XRD spectroscopy.

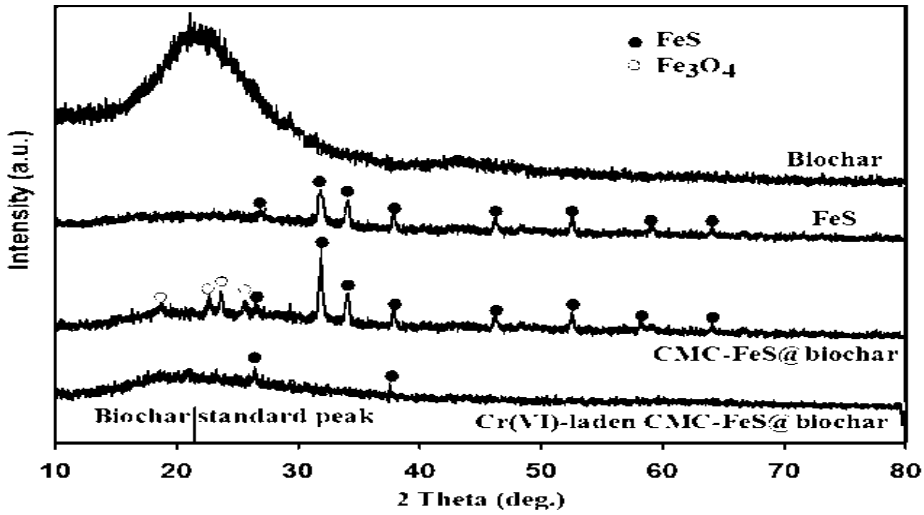

Figure 2.4. XRD patterns of biochar, FeS, biochar/FeS nanocomposite, and Cr (VI)-laden biochar/FeS nanocomposite [153].

Table 2.3. Some applications of XRD spectroscopy.

Biochar-nanocomposite material and purpose	Result of XRD spectroscopic analysis	Ref.
Orange peel-magnetite NS for organic pollutant and phosphate removal.	The magnetic biochar is mainly comprised of two phases which include iron oxide nano-particles with a diameter around 20–30 nm and biochar.	[136]
Wheat straw biochar/iron sulfide nanocomposite for removal of Cr (VI).	A comparison of peaks of FeS and biochar with peaks of biochar/FeS nanocomposite showed that FeS is incorporated in the biochar/ FeS nanocomposite as indicated by different peaks at 27.0 to 64.1° that are presented in Figure 2.4.	[153]
Silicon-containing rice husk biochar/ɣ-Fe_2O_3 nanocomposite for uranium adsorption	The crystalline phase and amorphous phase are observed. Also, the results suggested that the unique ɣ-Fe_2O_3 was simultaneously incorporated into the biochar precursor.	[154]
Corn straw biochar/MgO nanocomposite for phosphate removal from aqueous solution	Pure biochar was amorphous, but the biochar/MgO nanocomposite was semi-crystalline due to the presence of MgO. The XRD peak pattern changes were observed after phosphate adsorption because of $MgHPO_4$ and $Mg_3(PO_4)_2$ formation, which depends on contact time.	[155]
Khat/ZnO and neem/ZnO biochar nanocomposites for treatment of garage wastewater	Activated carbon from khat leaves was more amorphous, and the same result was observed from the XRD analysis. Activated neem biochar was more crystalline in comparison with activated khat biochar because of the presence of minerals such as Na, Ca, Mg, Cr, Fe, Zn, and Cu.	[52]

2.8.5. Thermo-gravimetric analysis

Thermo-gravimetric analysis (TGA) is an essential analytical method to identify the thermal properties of carbonaceous material occurring at different temperatures under different atmospheres [52]. Some studies revealed that, generally, there are three stages

during the thermal decomposition of lingo-cellulosic materials [137, 138]. These are in the range of 27-300 ℃ evaporation of adsorbed water, pyrolysis of biochar, and the release of most gases (300-500 ℃). Then, further consolidation of cross-linked product structure occurs between 500 and 850 ℃ and a weight loss. For instance, Chakraborty and coworkers reported the thermal stability of graphene oxide-coated biochar composite as described in Figure 2.5. The result revealed that the highest thermal degradation was observed within 400-800 ℃ [156].

Different biochars have varying thermal properties. For instance, Shamas and colleagues discovered that activated magnetic biochars synthesized using different procedures from Kans grass have varying thermal stabilities at higher temperatures [137]. During the investigation, the magnetic biochars followed almost the same degradation pattern between 700-800 ℃. However, in the last half of the third step, magnetic biochars synthesized in a single-step procedure from Kan's grass showed better thermal stability than those produced using a two-step procedure.

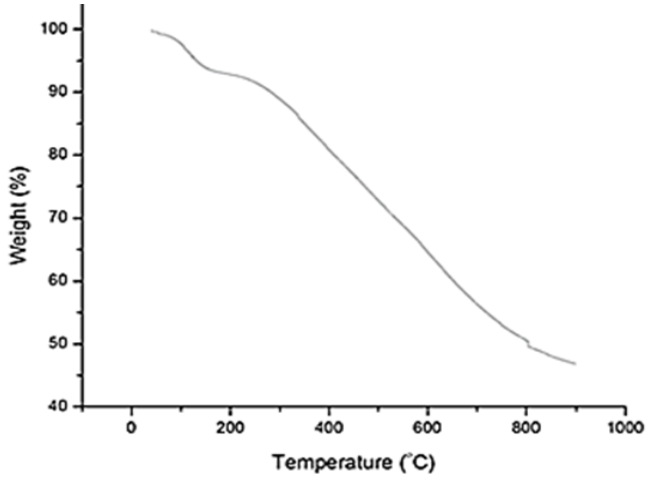

Figure 2.5. Thermal stability graph of graphene oxide-coated biochar composite [156].

2.9. Applications of Biochar-Based Nanocomposites for Wastewater Treatment

To remove various organic and inorganic contaminants from the water ecosystem, scholars are actively working to develop new methods that are cheap, easily accessible, and eco-friendly approaches [157]. Nanotechnology is a newly emerging field. It provides nanomaterial for the purification of water with a low cost, high efficiency, and reusability. Nanomaterials have properties such as large surface area and quantum size

effects. The use of nanomaterials as the adsorbent can provide unique opportunities, such as strong adsorption, enhanced redox reactions, and photo-catalytic properties to remove contaminants from wastewater [11]. A variety of nanomaterials such as nano metals, nano metal oxides, graphene or graphene-based nanomaterials, polymer-based nanomaterial, and biochar-nanocomposite have been reported for the removal of contaminants from wastewater.

For instance, Peng and coworkers reported their investigation on application of triarrhena biochar and its biochar-nanocomposite adsorbents to remove Congo red from water [158]. The adsorption capacity of the biochar was increased when titanium oxide (TiO_2) nanoparticles were added. During the pyrolysis process, TiO_2 is added to synthesize biochar-nanocomposite (BC-TiO_2) to activate the biochar. The adsorption performance of BC-TiO_2 composite is greatly enhanced due to the synergistic adsorption combination effect of TiO_2 and biochar. Similarly, Nadeem and coworkers have synthesized sawdust biochar-Fe_3O_4 nanocomposite, which exhibited efficient adsorption to remove reactive blue 21 (RB21) during the treatment of textile wastewater [140].

Haipeng and coworkers also synthesized biochar-nanocomposite derived from water hyacinth through-loading MnO_2 on its surface, which was effectively used to remove Pb, Cd, Cu, and Zn from water solution [159]. The study revealed that the biochar-nanocomposite has better adsorption efficiency for the heavy metal ions than the pristine biochar. In this specific study, higher adsorption capacities of the biochar-nanocomposite for the heavy metal were observed because of its abundant surface Mn-OH groups.

In general, biochar-based nanomaterials have higher efficiency in removing toxic heavy metals and synthetic dyes from wastewater. According to some reported studies, Fe_3O_4 biochar nanocomposites made from sawdust, rice husk, and palm oil empty fruit bunch have a better removal efficiency than virgin biochar [10, 138, 160–163]. Also, magnetic nanocomposite of activated carbon, carbon core-shell [164], and besides this metal-free activated spent coffee ground [162, 163], are employed for MB removal. Cervera-Gabalda and Kataria with their coworkers reported that Fe_3O_4 biochar nanocomposites of sewage sludge and woodchips, Vine shoots, burley tobacco stems, peanut husk and bagasse are investigated with higher efficiency than their pristine biochar. Furthermore, Fe_3O_4 nanocomposite of activated carbon [165, 166] and graphene [167] are employed for Cr(VI) removal.

The magnetic property of magnetic biochar offers a significant environmental advantage compared to other biochar-nanocomposites in the context of easy separation and regeneration of the biochar after its use, minimizing potential risks associated with the release of nanoparticles into the environment. In addition, $KMnO_4$-activated sludge [56], pine [168], and MnO_2 orange peel [169] biochar nanocomposites are employed to remove MB. $KMnO_4$ is a powerful oxidizing chemical that may be used to cleanse water and oxidizes harmful substances as well as to mildly oxidize biomass at room temperature [56]. The $KMnO_4$-activated biochar manufacturing technique has several advantages over other activation procedures, such as a faster activation period at ambient temperature, a moderate interaction with organic materials, reduced ash content biochar, and more environmental benefits.

Therefore, in this study, different biochar-base-nanocomposite materials were prepared from easily locally available biomass such as coffee husk and Khat (*Catha edulis*) leftover, treating separately with $KMnO_4$, and 1:1 molar ratio of FeS and $FeCl_3$. The efficiency of synthesized biochar-nanocomposites to remove Cr(VI) and MB from the aqueous solution were evaluated.

3. EXPERIMENTAL

3.1. Biomass Sample Collection

Coffee husk was collected from different coffee processing enterprises in Mizan-Aman, Ethiopia. Similarly, khat leftovers were collected in Jimma, Ethiopia. The two biomasses were chosen because of their broad availability and the large amounts of municipal solid waste that cause significant environmental harm across the country.

3.2. Chemicals and Reagents

The chemicals and reagents including $K_2Cr_2O_7$ (99%, NICE), $KMnO_4$ (99%, Finkem), $FeCl_3$ (99 %, Finkem), FeS(99%, Merck), HNO_3 (69%, Qualikems Fine chemicals), MB; $C_{16}H_{18}N_3SCl$ (99%, NICE), ultra-pure NaOH (99%, Merck), 1, 5-diphenylcarbazide (DPC) (99% Kiran Light Laboratories), ultra-pure KOH (99%, Merck), and NaCl (99.5%, Sigma-Aldrich) were used.

3.3. Instruments and Equipment

The pyrolysis process was carried out in a muffle furnace (DDRAWELL Artist of Science Muffle Furnace 1000 °C SX-4-10, Shanghai, China). An X-ray diffractometer (DRAWELL Artist of Science XRD-7000, Shanghai, China) was used to examine the crystallinity of the produced materials. Scanning electron microscopy (FEI Quanta 250, Romania) was used to analyze the surface morphology. The surface functional groups were qualitatively examined using Fourier transform infrared (FTIR) spectroscopy (Spectrum 65 FT-IR, PerkinElmer). Utilizing liquid N_2 adsorption-desorption isotherms at 77 K on an automated adsorption apparatus (ASAP 2020, Micrometric, USA), the porosity and pore sizes of the adsorbents were ascertained. Double-beam UV-Vis spectroscopy (SPECORDR200 PLUS Analytik Jena, Germany) was used for MB and Cr(VI) analysis.

3.4. Experimental Conditions

3.4.1. Characterization

To assess the crystallinity of the biochar nanocomposites using a DRAWWELL Artist of Science XRD-7000 X-ray diffractometer, the samples were ground into a powder. This was done by grinding the sample in a mortar and pestle. The powder was placed on a sample holder and it was loaded into the XRD instrument. The X-ray beam from the Cu tube source, with a wavelength of 1.5406 Å and power of 1.8 kW was scanned across the sample and the diffraction pattern was recorded in the range 2º to 150° with resolution 0.0001º.

A PerkinElmer Spectrum 65 FT-IR was used to carry out four scans of FTIR spectroscopy at a resolution of 4 cm^{-1} in the 4000-400 cm^{-1} range. KBr was used to prepare the material into thin pellets. It was placed in the FTIR spectrometer and the spectrum was acquired. The functional groups contained in the biochar nanocomposite were ultimately determined by analyzing the spectrum.

A scanning electron microscope (SEM FEI QUANTA 250, Romania) was used to detect the surface morphologies. The sample was placed on a stub and covered with a conductive tinny layer material. After it was placed inside the SEM chamber, the vacuum inside the chamber was increased. Then the image was acquired by scanning using low-energy electrons.

Using automated adsorption equipment (ASAP 2020, Micrometrics, USA) and liquid N_2 adsorption-desorption isotherms at 77 K, the porosity of the adsorbents was ascertained. The biochar nanocomposite sample was degassed to remove any adsorbed molecules. This is because the BET measurement is based on the adsorption of a known amount of gas onto the surface of the sample. If there are already molecules adsorbed on the surface, the BET measurement will be inaccurate. To degas the sample, it was heated to a high temperature in a vacuum chamber. The Brunauer-Emmett-Teller (BET) method was utilized to compute the surface area, while the Barrett-Joyner-Halenda (BJH) method was employed to analyze the pore size distribution.

The salt addition technique reported by Elisee and coworkers was applied to examine the pH of point of zero charge (pH_{PZC}) of the adsorbents [13, 170]. A 40 mL of 0.1 M $NaNO_3$

solution was added to a series of 50 mL centrifuge tubes. After adjusting the pH to the proper range of 2, 3, 4, 5, 6, 7, 8, 9, 10, and 11, using 0.1 M solutions of HNO_3 and NaOH as required, the values of pH were denoted as pHi. Then, after adding 0.2 g of adsorbents, the mixture was continuously shaken at 200 rpm for 24 h. Next, the pH of the supernatant in every tube was determined after it had settled, and the results were indicated by pH_f. pH_{PZC} was determined by taking the x-intercept of the ΔpH ($pH_f - pH_i$) plotted against pH_i.

3.4.2. Limit of detection, limit of quantification and linearity ranges of the analysis

The UV-Vis spectrometer was calibrated using standard solutions of MB and Cr(VI) at 665 and 540 nm, respectively. The instrument's limit of detection (LOD), linearity ranges (LR), and limit of quantification (LOQ) were determined by analyzing replicate standard solutions of varying concentrations prepared through serial dilutions. To determine the linearity range, a series of standard solutions with known concentrations of MB and Cr(VI) were prepared separately. The absorbance of each standard solution was then measured at the specified wavelengths for both MB and Cr (VI). Finally, the curves were plotted to identify the linear ranges. The linearity ranges were found to be 0.01-20 mg L^{-1} for MB analysis and 0.01-10 mg L^{-1} for Cr(VI) analysis (see Figure A1 a and b) provided in the Appendix.

To determine the LOD and LOQ of the method for MB analysis, ten blank samples (deionized water) were taken. Their pH was adjusted to 7.5 and their absorbance was measured at 665 nm. For Cr(VI), another ten of blank samples were taken, and after adjusting their pH to 2 their absorbance was measured at 540 nm. The LOD and LOQ were determined by multiplying the standard deviation (SD) of the blank analysis by 3 and 10, respectively. The LOD and LOQ for MB were found to be 0.002 and 0.005 mg L^{-1}, respectively. For Cr(VI) the LOD and LOQ were also determined to be 0.002 and 0.005 mg L^{-1}, respectively. After determining the LOD, LOQ and LR as expressed in section 3.3.2, calibration curves were constructed for each analysis, and used for three successive days (72 h). Representative calibration curves are provided in the Appendix, (see Figure A2 a and b)). The repeatability of the analyses was evaluated by analyzing replicate samples and expressed as the standard deviation (SD), indicated as error bars in the figures.

CHAPTER FOUR

4. MnOx-COFFEE HUSK AND KHAT LEFTOVER BIOCHAR NANOCOMPOSITES FOR REMOVAL OF METHYLENE BLUE FROM WATER

CHAPTER THREE

4.1 Introduction

Dyes are widely used to color materials in heavy industries such as textiles, paper, and food processing [6]. Reports show that dyes emitted by businesses account for 20% of water contamination [8, 9]. and they are persistent, non-biodegradable, bioaccumulative, poisonous, and carcinogenic, generating serious environmental consequences even at low concentrations [171]. They are also toxic to aquatic habitats and the food chain [10]. For example, even at low concentrations, its presence in water lessens its aesthetic value, limits light penetration, and influences gas solubility for photosynthesis and respiration processes [11]. MB, an organic dye used in paper, cotton, leather, and plastics, can cause tissue necrosis, cyanosis, and harm marine life. It enters the environment through industrial effluents, so proper treatment before discharge is crucial.

Various methods such as photo-catalytic degradation [27, 28], ultrafiltration [12, 45], electrocoagulation [46], electrochemical degradation [43], chemical precipitation [32], and adsorption [29] have been used for the removal of dyes from industrial effluents [44]. However, some of these methods have inherent limitations, such as high energy consumption, cost, generation of toxic sludge, incomplete treatment, and significant reagent consumption [47, 48]. Among these methods, the adsorption technique is a cost-effective, eco-friendly, and efficient solution for removing organic and inorganic pollutants [7].

The efficiency of the adsorption method primarily depends on the adsorbent materials used [34]. Adsorbents such as activated carbon, natural clay minerals, synthetic inorganic materials, synthetic nanoparticles, and biomass have been employed to remove various contaminants from aqueous solutions [89]. Recently, researchers have focused on searching for low-cost, efficient, and selective materials for the removal of toxic

Kochito, J.; Gure, A.; Abdissa, N.; Beyene, T. T.; Femi, O. E. MnOx-*Coffea arabica* Husk and *Catha edulis* Leftover Biochar Nanocomposites for Removal of Methylene Blue from Wastewater. *Sci. World J.*, **2024**, ID. 7585145. DOI:10.1155/2024/7585145.

chemicals such as dyes from wastewater [10]. Although activated carbon is a widely used adsorbent for water treatment, its raw materials and preparation methods are expensive and labor-intensive [33]. Materials that are porous and have a high surface area are known to have good adsorption capacity. Nowadays, scholars are focusing on using activated biochar to overcome some drawbacks associated with activated carbon [90]. Biochar is porous material produced through pyrolysis of biomass at temperatures less than 700 ℃ in oxygen-limited conditions. However, pure biochar also has minimal adsorption performances; thus, it should be modified by combining it with suitable nanomaterial [98].

Metallic oxide nanoparticles such as magnetic ferric oxide, manganese oxide, titanium oxide, and magnesium oxide which have high specific surface area have been used in wastewater treatment [99]. Nevertheless, nanoparticle aggregation presents a challenge, necessitating the use of supporting materials to enhance their stability and recyclability [8]. The biochar-based nanocomposite involves the use of composite material that combines the advantages of biochar which is porosity and having a higher specific surface area of nanomaterials [32].

Metal salts such as $AlCl_3$, $CaCl_2$, $MgCl_2$, $KMnO_4$, $MnCl_2$, $ZnCl_2$, and $TiCl_4$ are commonly used to activate biochar, resulting in the formation of Al_2O_3, AlOOH, CaO, MgO, MnOx, ZnO and TiO_2 nanoparticles on biochar surface [36]. Most biochar-based nanocomposites are synthesized by chemical activation using metallic ions. The synthesis can proceed in either one-step or two-step modification processes [32]. In the one-step process, both carbonization and activation are completed simultaneously in the presence of an activator. Whereas, in the two-step process, the biomass feedstock is carbonized first, then it is followed by activation using the appropriate salt. The metal ions used for activation are either attached to the surface or get into the interior of biomass upon impregnating/ dipping into salt solutions. Then, after pyrolysis, the metal ions are transformed into nano-metal oxide or metal hydroxide, and the biomass impregnated with metal ions becomes biochar-based nanocomposites [99].

Some reports show that different metallic oxide nanocomposites such as Fe_3O_4 nanocomposites of saw dust, rice husk, palm oil empty fruit bunch, spent coffee ground biochar and activated carbon are employed to remove MB from aqueous solution [10, 138, 160–163]. Also, $KMnO_4$-activated sludge [56] and pine [168], and MnO_2 orange

peel [169] biochar nanocomposites are used for MB removal. $KMnO_4$ is a strong oxidizing agent which can be used for water disinfection and oxidation of toxic matter which can undergo mild oxidation of biomass at room temperature conditions [56]. The $KMnO_4$-activated biochar production process is more advantageous in terms of its shorter activation time at room temperature, mild reaction with organic materials, forming less ash content biochar, and being more environmentally friendly than other activation processes. So, despite their removal efficiency MnOx-CHBNC and MnOx-KLBNC are environmentally preferable. However, based on the knowledge of the authors of this study, any investigation is not reported about utilizing $KMnO_4$-activated coffee husk and khat left over biochar nanocomposites for removal of MB from aqueous solution.

In Ethiopia, there is high production and consumption of *Coffea arabica* (coffee), and *Catha edulis* (khat), which yields tons of biomass wastes that pollute the environment [51, 52]. CH and KL that are not properly disposed of add to municipal waste, which raises the cost of transportation to the disposal site [55]. Coffee husks and khat leftovers are rich in organic matter, nitrogen, and phosphorus [53, 54]. Due to their high demands, wet coffee processing plants are usually built near rivers or other water sources [81]. After the coffee is harvested, various by-products such as coffee pulp, husk, silver skin, and spent coffee grounds are generated. Disposing of these by-products in water bodies leads to environmental pollution, causing damage to aquatic ecosystems. This is due to the promotion of algae and aquatic plant growth, depletion of oxygen levels, and eutrophication. Coffee husks also contain chemicals such as caffeine, tannins, chlorogenic, free phenols, and rosmarinic that can be toxic to aquatic life [84]. Large-scale dumping of coffee husks and khat leftovers can lead to nutrient imbalances, hinder plant growth and soil fertility, and increase soil acidity. Burning coffee husks releases harmful pollutants into the atmosphere, contributing to air pollution and respiratory problems. Coffee husks left to decompose in landfills emit methane, which is a potent greenhouse gas that contributes to climate change [81]. Discarding khat wastes in open dumpsites results in visual pollution, attracts disease-carrying vectors, and creates breeding grounds for pathogens. Khat leftovers are sometimes littered on the streets, degrading the environment and potentially blocking drainage systems [86, 87].

The purpose of this study was to evaluate the transformation of CH and KL into valuable products, offering dual advantages. These include eliminating hazardous contaminants

from water and disposing of biomass waste efficiently. The manganese oxide-coffee husk biochar nanocomposite (MnOx-CHBNC) and manganese oxide-khat leftover biochar nanocomposite (MnOx-KLBNC) were synthesized, characterized, and their MB and Cr(VI) removal efficiencies were evaluated. The effects of time, adsorbent dose, concentration, and pH on the MB adsorption efficiencies of the two adsorbents were investigated. Moreover, the kinetics and adsorption isotherms were determined. Desorption experiments of MB from MnOx-CHBNC and MnOx-KLBNC were carried out to assess the adsorbents' regeneration or reusability.

4.2. Experimental Procedure

4.2.1. Preparation of MnOx-CHBNC and MnOx-KLBNC.

The KL samples, which included hard leaves, branches and twigs typically discarded by producers, traders and consumers, were cut into small slices. They were then washed with deionized water, dried at 105 ℃ for 24 h, milled into powders of 2 mm, and stored in a dry plastic container at ambient conditions [138, 172]. Likewise, the CH samples were cleaned, dried, ground, and stored following the same procedures as the KL sample.

For the synthesis of biochar nanocomposite materials, 25 g of each biomass powder was separately immersed in a 300 mL solution containing various concentrations of $KMnO_4$: 12.5, 25, 50, and 75 mmol [136, 172–175]. After 1 h of stirring, the water was evaporated in an oven at 80 ℃ until the mixture's weight remained constant. The dried sample was transferred to the crucible, wrapped in aluminum foil, and put in a muffle furnace heated to 110 ℃. After 30 min at 110 ℃, the sample was heated at a rate of 10 ℃ min^{-1} until it reached 300 ℃. Finally, it was pyrolyzed at 300 ℃ for one h. The generated biochar-metal oxide/hydroxide composite was then cooled to ambient temperature, pulverized, and sieved through 0.1 mm - 0.2 mm mesh sizes. The pristine biochar was likewise made with 25 g of dry biomass powder. Finally, it was repeatedly rinsed with deionized water. Then, it was oven-dried at 80 ℃ and kept for further experiments. The same procedures were followed to synthesize the biochar nanocomposites of the metallic oxides specified above at 400 ℃ and 500 ℃. The prepared biochar nanocomposites were labeled as MnOx-$CHBNC_{300}$, MnOx-$CHBNC_{400}$, MnOx-$CHBNC_{500}$, MnOx-$KLBNC_{300}$, MnOx-$KLBNC_{400}$, and MnOx-$KLBNC_{500}$.

4.2.2. Adsorbent selection

Following the procedures mentioned in section 4.2.1, 30 different adsorbents were produced. The synthesized materials were evaluated to select the most efficient adsorbent for removing MB from an aqueous solution. Preliminary tests were conducted to assess the MB removal efficiency of each using 0.2 g adsorbent, 20 mL of 20 mg L^{-1} MB, pH 7.5, and shaking the mixture at 200 rpm and 25±1 ℃ for 2 h, following the adopted experimental procedures reported by Giraldo and coworkers [176]. Then, after shaking the content at 200 rpm for 2 h on the horizontal shaker, it was centrifuged at 5000 rpm for 10 min. The supernatant was transferred to the cuvette for the UV-Vis analysis at λ = 665 nm. Each experiment was conducted in triplicate sample analysis.

The MB removal efficiency (R) for each adsorbent was calculated using Equation (4.1), and the dye adsorption capacity (q_e) of the materials was determined employing Equation (4.2).

$$R = \frac{(C_o - C_e)}{C_o} \times 100 \quad (4.1)$$

$$q_e = \frac{(C_o - C_e)V}{m} \quad (4.2)$$

The starting and equilibrium concentrations of adsorbate are C_o (mg L^{-1}) and C_e (mg L^{-1}), respectively; m (g) is the mass of the adsorbent; and V (L) is the volume of the sample solution [177].

4.2.3. Adsorption isotherm and kinetics

Batch adsorption experiments were performed using 20 mL aqueous samples containing different initial concentrations of MB from 10 – 500 mg L^{-1}. To each dye solution, 0.2 g MnOx-CHBNC_{300} was added at 25±1 ℃. Similarly, to other sets of dye solutions, 0.15 g MnOx-KLBNC_{300} was added. The mixtures were then shaken at 200 rpm using a horizontal shaker for 2 h. Subsequently, the samples were filtered, and the equilibrium concentrations of the MB in each solution were measured by UV-Vis spectrometry at 665 nm.

4.2.4. Regeneration studies

The reusability of the adsorbents was evaluated by carrying out, adsorption-desorption for six cycles at 25°C following the experimental design reported by Păcurariu and coworkers [8]. A 2 g of MnOx-CHBNC and 1.5 g of MnOx-KLBNC were separately dispersed in 200 mL of 20 mgL^{-1} MB solution by shaking for 120 min at pH 7.5. Then it was centrifuged, and the concentrations of the MB in the supernatant were analyzed. For desorption, 2 g of the MB-loaded adsorbents were dispersed in 50 mL of 50% ethanol at pH = 6.5. The content was shaken for 120 min and then separated by filtration. After each cycle, the MnOx-CHNBC and MnOx-KLBNC adsorbents were washed with distilled water, dried at 70 ℃ for 2 h, and reused for adsorption in the next cycle.

4.3. Results and Discussion

4.3.1. Adsorbent selection

In this study, biochar-based nanocomposites were prepared by varying the temperature of pyrolysis and the mass of the activating agent, $KMnO_4$. Table 4.1 summarizes that the preliminary tests conducted for the adsorbent selection show that all 30 different adsorbents synthesized in this study exhibited different efficiencies in removing MB from an aqueous solution. This is due to the effect of the type of biomass, pyrolysis temperature, and the amount of activating agent.

Table 4.1. Result of adsorbent selection based on MB removal efficiency.

Adsorbent	$KMnO_4$, mmol	Pyrolysis Temp, ℃	MB Removal Efficiency, %
CHB_{300}	0.0	300	39.08
CHB_{400}	0.0	400	44.73
CHB_{500}	0.0	500	80.78.
MnOx-$CHBNC_{300}$	**12.5**	**300**	**99.23**
MnOx-$CHBNC_{400}$	12.5	400	89.96
MnOx-$CHBNC_{500}$	12.5	500	96.10
MnOx-$CHBNC_{300}$	25.0	300	97.20
MnOx-$CHBNC_{400}$	25.0	400	96.95
MnOx-$CHBNC_{500}$	25.0	500	93.99
MnOx-$CHBNC_{300}$	50.0	300	84.40
MnOx-$CHBNC_{400}$	50.0	400	95.33
MnOx-$CHBNC_{500}$	50.0	500	95.51
MnOx-$CHBNC_{300}$	75.0	300	66.65
MnOx-$CHBNC_{400}$	75.0	400	97.46
MnOx-$CHBNC_{500}$	75.0	500	86.38
KLB_{300}	0.0	300	75.26
KLB_{400}	0.0	400	76.41
KLB_{500}	0.0	500	88.37
MnOx-$KLBNC_{300}$	**12.5**	**300**	**98.01**
MnOx-$KLBNC_{400}$	12.5	400	97.14
MnOx-$KLBNC_{500}$	12.5	500	96.86
MnOx-$KLBNC_{300}$	25.0	300	97.39
MnOx-$KLBNC_{400}$	25.0	400	95.99
MnOx-$KLBNC_{500}$	25.0	500	96.73
MnOx-$KLBNC_{300}$	50.0	300	89.45
MnOx-$KLBNC_{400}$	50.0	400	95.45
MnOx-$KLBNC_{500}$	50.0	500	97.30
MnOx-$KLBNC_{300}$	75.0	300	86.64
MnOx-$KLBNC_{400}$	75.0	400	86.75
MnOx-$KLBNC_{500}$	75.0	500	96.80

The effects of pyrolysis temperature and the activating agent to biomass ratio on the efficiency of MnOx-CHBNC and MnOx-KBNC were investigated for removing MB from an aqueous solution. Figure 4.1a and b show the effects of pyrolysis temperature and activating agent-to-biomass ratio on the efficiency of MnOx-CHBNC and MnOx-KBNC. For pristine CHB and KLB, the efficiency of MB removal from aqueous solution increases with increasing pyrolysis temperature. Yang and coworkers reported that the pyrolysis temperature can affect the yield and the surface properties [108]. The report describes that at higher pyrolysis temperatures, the amount of biochar and the number of acidic functional group (-COOH) decreased. In contrast, the alkaline functional groups, ash content, and pH increased. Therefore, the pyrolysis temperature can affect the MB adsorption efficiency of MnOx-CHBNC and MnOx-KLBNC. Treating with $KMnO_4$ significantly increases the adsorption efficiency from 39.08 to 99.26% for CHB and 75.26 to 98.20% for KLB. The results also showed that the amount of the activating agent affected the removal efficiency. In this work, we observed the highest efficiency when 25 g of each biomass was pretreated with 12.5 mmol of $KMnO_4$ (2:1 g $mmol^{-1}$ ratio). Generally, the study revealed that MnOx-CHBNC and MnOx-KLBNC synthesized by pretreating 25 g of biomass with 12.5 mmol of $KMnO_4$ and pyrolyzed at 300 ℃ for 1h have the highest efficiency than the other types of biochar synthesized in this study.

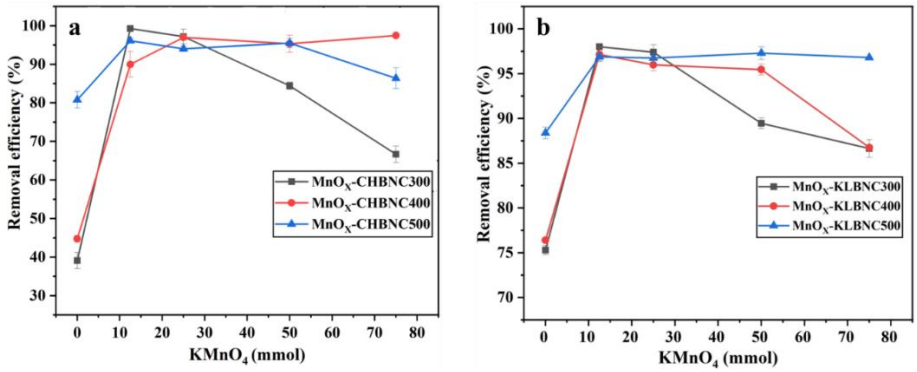

Figure 4.1. Pyrolysis Temperature and biomass to activating agent ($KMnO_4$) ratio evaluation: (a) MnOx-CHBNC and (b) MnOx-CHBNC. Experimental conditions: MB initial concentration, 20 mg L^{-1} ; adsorbent dose, 0.2 g L^{-1}; pH, 7.5; temperature, 25±1 ℃ ; contact time, 120 min.

4.3.2. Adsorbent characterization

Figure 4.2a show the XRD patterns of the pristine CHB and MnOx-CHBNC and 4.2b show that of KLB and MnOx-KLBNC. All adsorbents consist of natural cellulose, lignin, and non-crystalline hemicelluloses. The diffraction peak appeared at 2θ = 16.1º, and 22.4º was assigned to natural cellulose, which is in agreement with the study reported by Baig and coworkers [137]. Reports confirm that large d-spacing in the XRD peaks of the biochar is attributed to the existence of unconverted cellulose and the presence of -OH, C=C, and C-O groups [153]. Generally crystalline materials have sharper and more intense peaks than amorphous materials [178, 179]. The broadening of XRD peaks is mainly caused by particle size and the arrangement of lattice strains. The scattering of X-rays from non-uniformly arranged surface materials and pores of the biochar leads to broad peaks [161, 180]. Very weak broad peaks around 37.4º and 41.2º indicate the presence of MnO_2 in the biochar nanocomposite with a non-uniform distribution, which causes the scattering of X-rays [181]. Additionally, biochar is a porous material and its pores can trap X-rays. So the result implies that the diffraction peaks in the XRD patterns of both adsorbents cannot be indexed as crystallized. In general, each pristine biochar, MnOx-CHBNC, and MnOx-KLBNC have no uniform structure (amorphous).

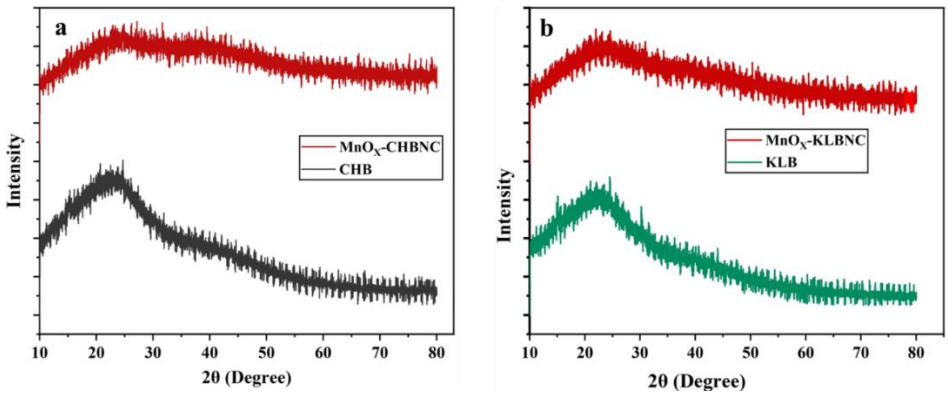

Figure 4.2. XRD patterns of (a) CHB and MnOx-CHBNC and (b) KLB and MnOx-KBNC.

Figure 4.3a-d shows the SEM images of the activated and pristine biochar, CHB, and KLB. The images confirmed the amorphous and heterogeneous structures of the biochar. Pores were found in all biochars as the result of volatile material escape and channel structure creation during pyrolysis [182]. As shown in Figures 4.3b and d**,** that the

formation of larger pore structure is more prominent in MnOx-CHBNC and MnOx-KLBNC. As the literature indicates, activation increases porosities and enlarges the diameter of smaller pores created during pyrolysis [123].

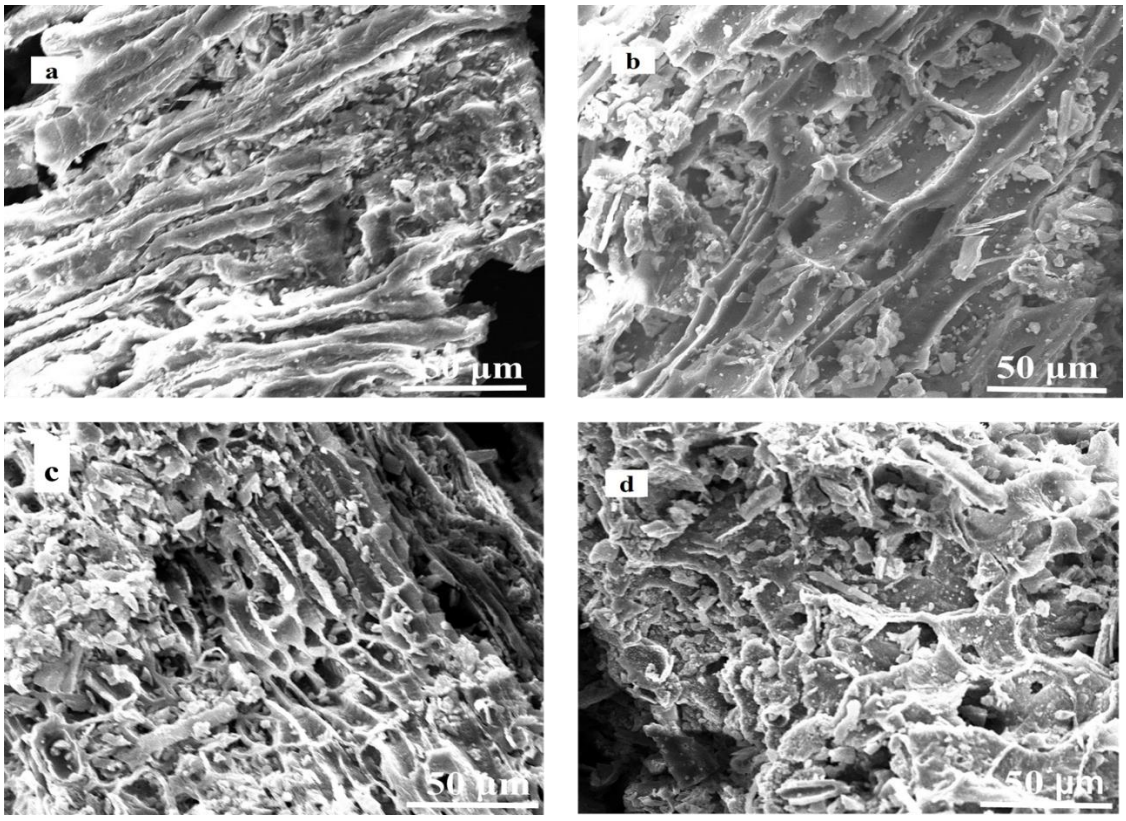

Figure 4.3. SEM images of pristine and activated coffee husk and khat leftover biochar (a) CHB, (b) MnOx-CHBNC, (c) KLB and (d) MnOx-KLBNC.

FTIR spectra of pristine and activated biochar are shown in Figure 4.4a for CHB and MnOx-CHBNC; 4.4b for KLB, and MnOx-KLBNC. The spectra of both pristine and activated biochars showed the presence of functional groups such as O-H (3417-3426 cm^{-1}), C-H (2853-2920 cm^{-1}), C=C (1611-1622 cm^{-1}), and C-O (1411-1466 cm^{-1}) as also reported in other literature [13, 29, 114, 168, 183, 184]. These functional groups may take part in the adsorption of MB through electrostatic interaction [185]. The observed broad bands of O-H in MnOx-CHB and MnOx-KLBNC spectra could be due to the additional source of the OH group from the moisture [52].

Additionally, the broadening peaks with decreased intensity around 3425 cm^{-1} in the MB-adsorbed MnOx-CHBNC and MnOx-KLBNC FTIR spectra shown in Figure 4.4a and b suggest that there may be chemisorption on the surface of biochar, leading to the

formation of new compounds. The two main mechanisms of MB adsorption on biochar are electrostatic attraction of cationic MB by the large number of OH groups in the solution at higher pH and hydrogen bond formation between the oxygen present in MB and the OH group of biochar. Furthermore, through surface complexation, oxygen-containing functional groups also form complexes with MB molecules, which lead to MB adsorption on the adsorbents. Then, following adsorption, the peaks at 1624, 1617 and 1386 cm^{-1} changed and the peak intensity increased, indicating a rise in the quantity of -C=C bonds caused by the cyclic alkene, most likely as a result of the MB adsorption.

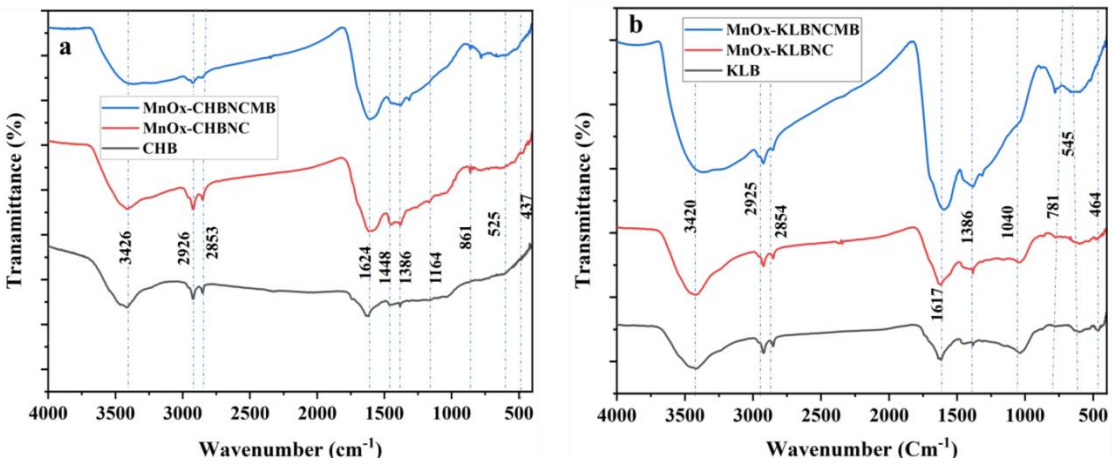

Figure 4.4. FTIR spectra of (a) CHB, MnOx-CHBNC and MnOx-CHBNCMB and (b) KLB, MnOx-KLBNC, and MnOx-KLBNCMB.

Figure 4.5a-d shows the adsorption-desorption isotherm, and BET analysis plots for the CHB, KLB, MnOx-KLBNC and MnOx-CHBNC. Based on the results of BET analysis, specific surface area, pore size and pore volume for the CHB were reported as 0.519 m^2 g^{-1}, 32.804 nm, 0.004 cm^3 g^{-1}, for MnOx-KLBNC 1.03 m^2 g^{-1}, 19.511nm , 0.006 cm^3 g^{-1}, for KLB 0.826 m^2 g^{-1}, 27.626 nm, 0.005 cm^3 g^{-1}, for MnOx-CHBNC 1.289 m^2 g^{-1}, 21.218 nm, and 0.006 cm^3 g^{-1} respectively. The results showed that MnOx-CHBNC and MnOx-KLBNC have larger specific areas, total pore volumes, and smaller pore diameters than virgin biochars. Also, the adsorption-desorption isotherm and BET analysis revealed that the adsorbents have mesoporous architectures [162].

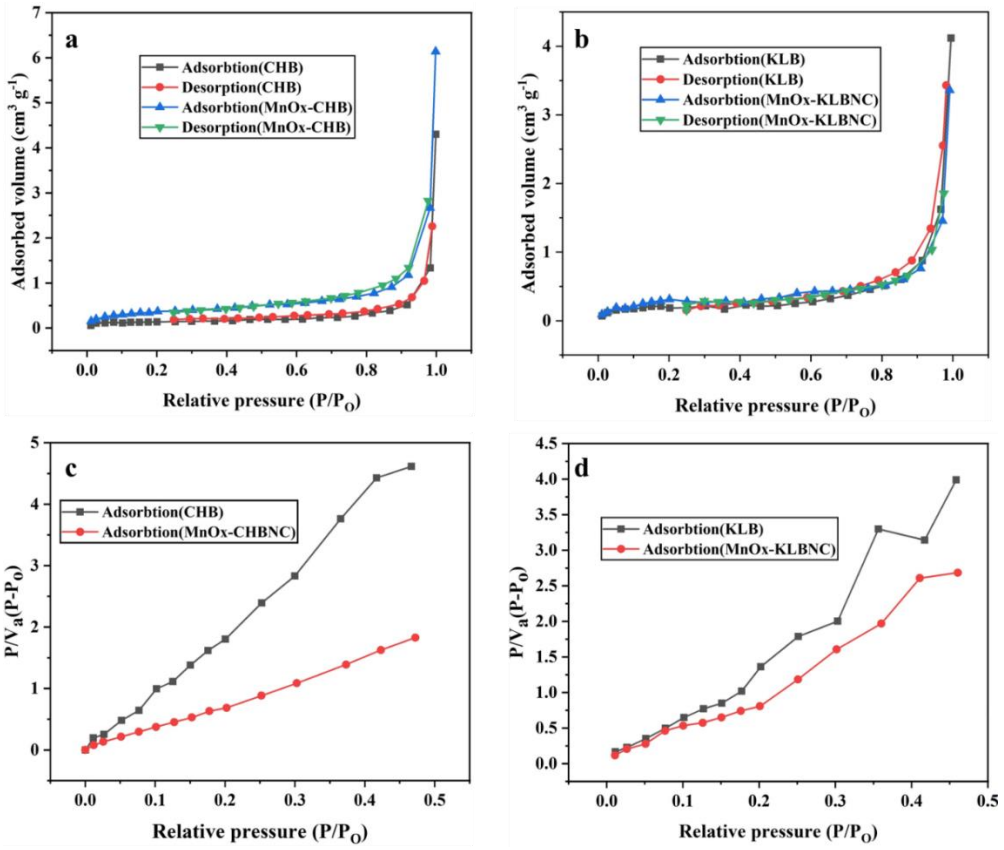

Figure 4.5. Adsorption-desorption isotherm of nitrogen on (a) CHB and MnOx-CHBNC, (b) KLB and MnOx-KLBNC, and BET analysis plot of (c) CHB and MnOx-CHBNC and (d) KLB and MnOx-KLBNC.

4.3.3. pH of point of zero charge

An adsorbent's pH of point of zero charge (pH_{PZC}) is determined by the chemical and electrical characteristics of its surface functional groups. Figure 4.6 shows the pH_{PZC} values for MnOx-CHBNC and MnOx-KLBNC. The pH_{PZC} values were estimated at pH 7.82 (MnOx-KLBNC) and 8.43 (MnOx-CHBNC). As a result, pH values should be kept above these levels to guarantee that negatively charged surfaces promote adsorption via electrostatic interaction between the adsorbents and the cation (MB).

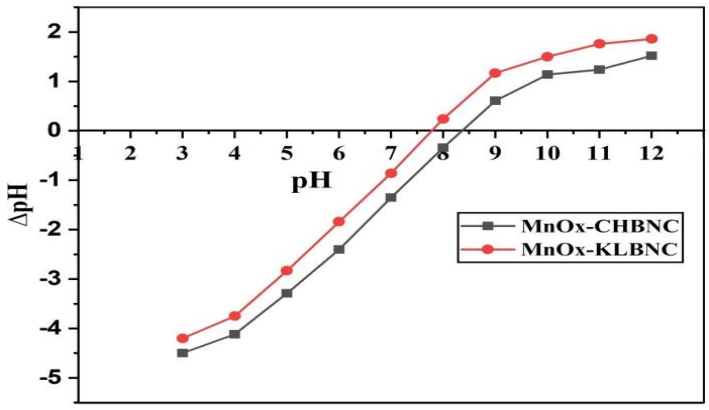

Figure 4.6. pH_{PZC} of MnOx-CHBNC and MnOx-KLBNC.

4.3.4. Batch adsorption studies

Out of the 30 different adsorbents that were prepared in this study, MnOx-CHBNC and MnOx-KLBNC are selected based on the result of the preliminary adsorbent selection experiment which was conducted in section 2.3, and it is discussed under section 3.3 (Table 4.1 and Figure 4.1). The parameters that can affect the adsorption efficiency of MnOx-CHBNC and MnOx-KLBNC have been investigated at constant temperature (25±1 ℃).

4.3.4.1. The effect of contact time

Contact time is one of the factors affecting adsorption efficiency. The effect of time was investigated from 5-180 min. In this study, the dose was 0.2 g per 20 mL, the pH was 7.5, and the initial concentration was 20 mg L^{-1}. Figure 4.7 showed that MB adsorption was found to be fast during the initial stages of the adsorption. It then slowed down after 60 min and began to remain slightly constant after 60 min for adsorbents. Adsorption was initially fast due to the availability of active surface, but it gradually decreased over time until equilibrium was reached. The remaining adsorption sites face challenges to sustained adsorption due to repulsive interactions between solute molecules adsorbed on the solid and bulk phases [53]. Kumar and coworkers also reported that the removal efficiency of an alkaline-treated banana stem biochar for MB dye increases with an increase in contact time [185]. Based on the result 60 min was taken as optimum contact time for the subsequent studies.

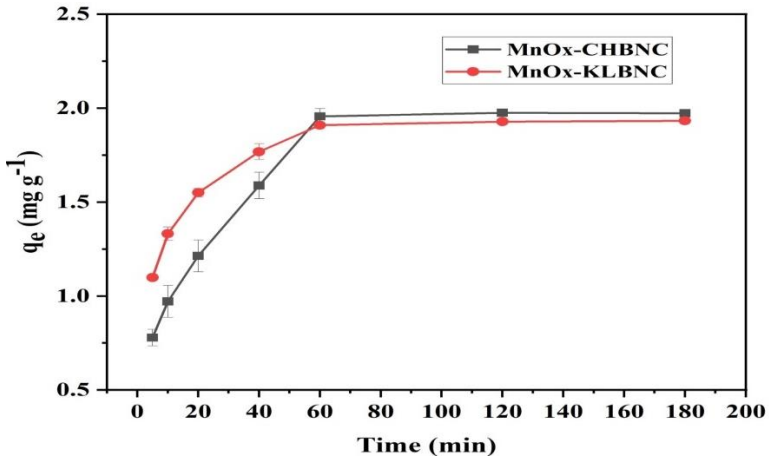

Figure 4.7. The effect of contact time on MB adsorption capacity.

4.3.4.2. The effect of adsorbent dose.

Figure 4.8a demonstrates that the removal efficiency of MB varied with the dosages of MnOx-CHBNC and MnOx-KLBNC. The effects of the adsorbent dose was studied using 0.1, 0.15, 0.2, 0.3, 0.4, and 0.5 g per 20 mL for both MnOx-CHBNC and MnOx-KLBNC, with all other parameters held constant (pH 7.5, initial concentration 20 mg L^{-1}, and contact time 60 min). Figure 8a and b shows that increasing the dose of MnOx-CHBNC from 0.1 g to 0.2 g enhanced MB removal efficiency by 4.34% while increasing the dose of MnOx-KLBNC from 0.1 g to 0.15 g increased removal efficiency by 2.83%. These improvements were observed because of the increased number of available adsorption sites. These results agreed with the study reported by Le and coworkers [55]. The adsorption of MB slightly increased when the dose was raised to more than 0.15 g for MnOx-KLBNC and 0.2 g for MnOx-CHBNC because the adsorbent surface would eventually reach a saturation state. Although the removal efficiency of MB slightly decreased to 97.74% when the MnOx-CHBNC dose was more than 0.3 g, this may be due to the aggregation of adsorbents, which hinders accessible binding sites. Also, a similar phenomenon reported by Fakhri agrees with this result [56].

However, the adsorbent dosage had a detrimental impact on the adsorption capacity (Figure 4.8a and b). When the dosages of MnOx-CHBNC and MnOx-KLBNC were increased from 0.1 to 0.5 g per 20 mL, the value of q_e dropped dramatically. As a result, the slope of the adsorption capacity curve decreased because when the amount of adsorbent is low, the active adsorption sites may quickly mix with adsorbates and

approach saturation. When the quantity of adsorbent surpasses a specific threshold, or when more adsorption sites fail to come into touch with adsorbate molecules [57]. Furthermore, when the number of adsorbents increases, they tend to aggregate, diminishing the sorbents' specific surface area [58]. Finally, based on the results, 0.15 g MnOx-KLBNC and 0.2 g MnOx-CHBNC per 20 mL were chosen for the subsequent studies.

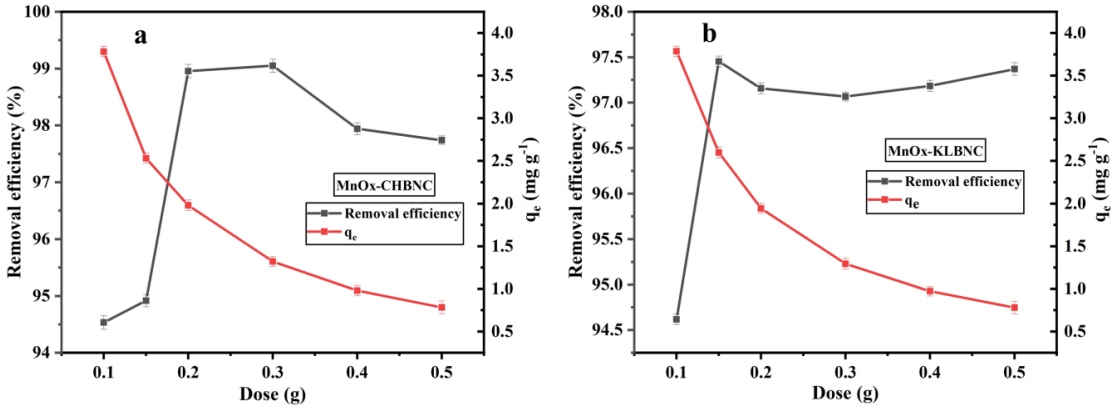

Figure 4.8. The effect of adsorbent dose on the removal efficiency and adsorption capacity of (a) MnOx-CHBNC and (b) MnOx-KLBNC to remove MB from water.

4.3.4.3. Effect of initial concentration

The effect of initial MB concentrations ranging from 20 to 500 mg L^{-1} was investigated. The results demonstrate that the adsorption capacity increased with the concentration of MB (Figure 4.9).

Adsorption of molecules happens more quickly at higher concentrations because a greater driving force is required for the mass transfer of dye molecules. In addition, greater concentrations needed a longer equilibrium time. Because near the end of adsorption most of the sorbate molecules migrate into the porous structure of the adsorbent when the adsorbent surface becomes saturated. The results agree with the report on removing MB by mangosteen peel biochar prepared via hydrothermal carbonization for MB removal [190]. Thus, 20 mg L^{-1} was selected as the optimum initial concentration, from which MnOx-CHBNC and MnOx-KLBNC removed about 99.27% and 98.20%, respectively. Also, Figure 4.9 shows that at the optimum condition, 0.2 g of MnOx-CHBNC can remove 93.87% of MB from 20 mL of 40 mg L^{-1} solution and 0.15 g of MnOx-KLBNC 94% of MB from 20 mL of 80 mg L^{-1} aqueous solution.

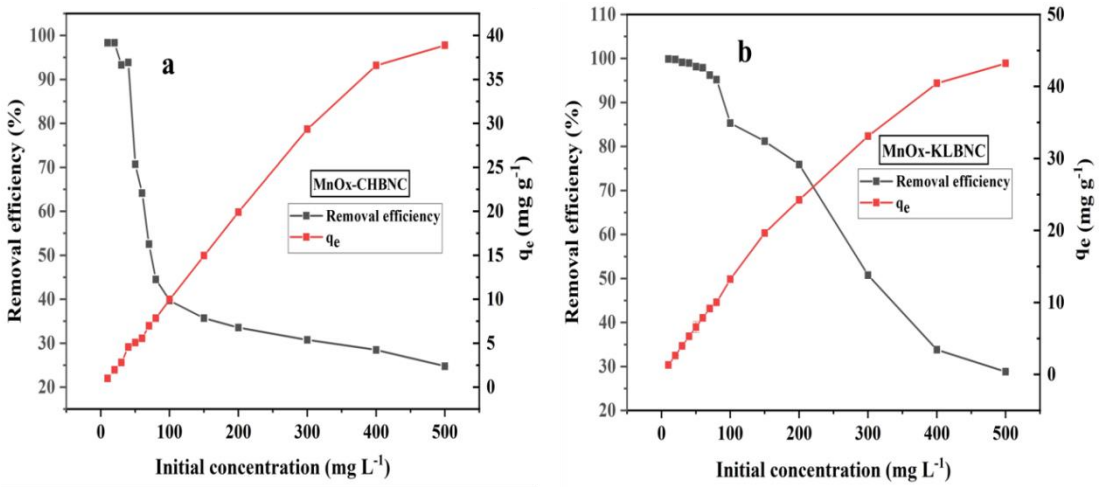

Figure 4.9. The effect of initial concentration on the removal efficiency, and the adsorption capacity of (a) MnOx-CHBNC and (b) MnOx –KLBNC to remove MB from water.

4.3.4.4. Effect of pH

The pH of the solution affects the adsorption processes because the functional groups of the adsorbent and ionizable organic dye molecules can change the surface charge of the adsorbent [51]. The pH determines the competition between cationic dyes with adsorbent and extra OH^-/H^+ ions in the solution resulting in fluctuation of MB adsorption capacity.

In this study, the effect of pH was evaluated from 3 - 12 by adjusting to the required pH value using 0.10 M HNO_3 and 0.10 M NaOH solutions. Figure 4.10 shows the effect of the pH of the solution on the MB adsorption capacity of the MnOx-CHBNC and MnOx-KLBNC. The initial MB concentration in the study was 20 mg L^{-1}, adsorbent doses were 0.2 g for MnOx-CHBNC and 0.15 g for MnOx-KLBN, and contact times were 60 min. The results showed that the adsorption capacity of MnOx-CHBNC increased (1.93-1.97 mg g^{-1}) in the pH ranging from 2 to 8 pH and that of MnOx-KLBNC increased (2.56-2.61 mg g^{-1}) in the pH range of 2 to 8. Then after the pH value get higher than 8, the adsorption capacity was slightly constant. This is because the MB dye molecules, which are cationic, generate a strong electrostatic repulsion on the surface of biochar with a high concentration of H^+ ions under an acidic environment. In addition, according to Islam and coworkers [52], the presence of the OH group on an adsorbent surface triggers the protonation of the OH group and creates a competition between H^+ ions and dye molecules to bind with the active sites, leading to low uptake of sorbate molecules.

Generally, for both adsorbents, the differences between the lowest adsorption capacities at pH 2 and the maximum adsorption capacities at pH 12 are insignificant, and the minimum removal efficiency is above 96%. This means the adsorbents form the buffer system, which can resist the pH changes. Therefore, MnOx-CHBNC and MnOx-KLBNC can be used to remove MB in both acidic and alkaline media. Finally, based on the result pH 8 was chosen as an optimum pH for the subsequent studies.

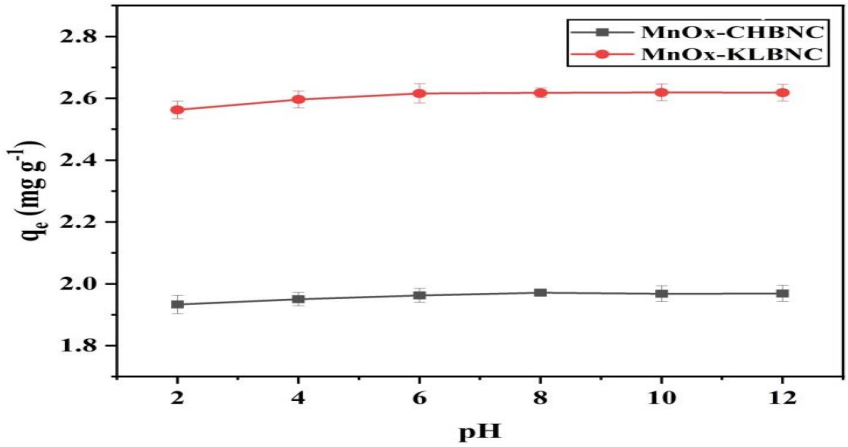

Figure 4.10. The effect of pH on MB adsorption capacity of MnOx-CHBNC and MnOx-KLBNC.

4.3.4.5. The effect of temperature and thermodynamics study

The study investigated the impact of temperature on the efficiency of MB adsorption using two different adsorbents, MnOx-CHBNC and MnOx-KLBNC, at three different temperatures: 25°C, 35°C, and 45°C. The results indicated that the efficiency of both adsorbents decreased with an increase in temperature, suggesting that the adsorption process is exothermic. Also, this has been confirmed by the negative ΔH obtained from the thermodynamic analysis. Table 4.2 presents the thermodynamic parameters, such as ΔH, ΔG, and ΔS, which were analyzed using a plot of 1/T on the x-axis versus ln(K_L) on the y-axis. The slope and intercept of the plot were equal to ΔS/R and –ΔH/R, respectively [30]. Here, T represents the temperature in Kelvin, K_L is a ratio (q_e/c_e) of the concentration of MB in the solid and liquid phases, and R is the universal gas constant. ΔG represents the change in free energy, ΔH represents the change in enthalpy, and ΔS represents the change in entropy. The negative value of ΔG indicates that the adsorption process is spontaneous.

Table 4.2. Thermodynamic behavior of adsorption of MB on MnOx-CHBNC and MnOx-KLBNC.

	Temp. (K)	**K_L**	**ΔG (KJ /mol^{-1})**	**ΔH (KJ mol^{-1})**	**ΔS (KJ K^{-1} mol^{-1})**	**R^2**
MnOx-CHBNC	298	6.032	-4.452	-49.635	-1.522	0.951
	303	2.465	-2.310			
	318	1.720	-1.434			
MnOx-KLBNC	298	12.17	-6.191	-87.131	-2.73	0.946
	303	2.465	-2.311			
	318	1.346	-0.785			

4.3.4.6. Adsorption isotherm and kinetics model

Adsorption isotherms describe the adsorbate concentration and adsorption capacity at a given adsorbent dosage and temperature [7]. The analysis of these isotherms also helps to better understand the adsorption processes, which are influenced by characteristics such as surface polarity, surface area, and porosity. Linear forms of Langmuir and Freundlich isotherm models can be used to quantify the equilibrium adsorption data (Equations 4.3 and 4.4) [59]. The Langmuir isotherm (Equation 4.3) describes monolayer adsorption on a homogeneous surface with uniform active sites**.** The adsorption equilibrium was studied by fitting the experimental data to the linear equations of Langmuir and Freundlich isotherm models [6].

Langmuir isotherm model: $$\frac{C_e}{q_e} = \frac{1}{K_L q_m} + \frac{C_e}{q_m} \quad (4.3)$$

Freundlich isotherm model: $$\log q_e = \log K_F + \frac{1}{n}\log C_e \quad (4.4)$$

Where q_e (mg g^{-1}) is the amount of MB adsorbed; C_e (mg L^{-1}) is the adsorbate concentration in the solution at equilibrium; K_L is the Langmuir adsorption constant, and q_m (mg g^{-1}) is the maximum adsorption capacity for monolayer formation on the adsorbent [60]. The value of K_F is the adsorption or distribution coefficient, which represents the number of ions adsorbed onto the beads. The value of 1/n indicates surface heterogeneity; as its value gets closer to zero, the surface becomes more heterogeneous [61]. A fundamental characteristic of the Langmuir isotherm is to predict the affinity

between adsorbate and sorbent using a dimensionless constant, known as separation factor R_L, which can be calculated by Equation 4.5:

$$R_L = \frac{1}{1+K_L C_o} \quad (4.5)$$

Where C_o (mg L^{-1}) is the adsorbate initial concentration. The value of R_L stands between 0 and 1 for favorable adsorption, while $R_L > 1$ represents unfavorable adsorption, $R_L = 1$ represents linear adsorption, and $R_L = 0$ for irreversible adsorption processes [61].

The Langmuir and Freundlich isotherm parameters are investigated using the initial concentrations ranging from 20 – 500 mg L^{-1}, and their results are presented in Figure 4.11a – d. The Langmuir and Freundlich isotherm parameters and related correlation coefficients (Figure 4.11a – d) are summarized in Table 4.3. A higher correlation coefficient (R^2) indicates greater applicability of the Langmuir model (R^2 = 0.999 for MnOx-CHBNC and R^2= 0.991 for MnOx-KLBNC), demonstrates the monolayer adsorption on a specific site of a homogeneous surface of the adsorbent [9]. The Langmuir isotherm predicts that adsorption energy is uniform on the adsorbent surface and no interaction exists between the adsorbed molecules [13]. The low separation factor values (R_L = 0.080 for MnOx-CHBNC and R_L=0.048 for MnOx-KLBNC) imply a favorable physical adsorption process. Freundlich isotherm demonstrates the multilayered adsorption for heterogeneous surfaces or surface-supporting sites of different affinities [184]. The calculated value of n falling in the range of 0 to 1, indicates favorable adsorption. Furthermore, the Langmuir isotherm model has a higher regression coefficient R^2 than the Freundlich model (Table 4.3), showing Langmuir model provides a better description, and these results suggest monolayer adsorption of MB on the surface of MnOx-CHBNC and MnOx-KLBNC.

In terms of non-linearity isotherms of Langmuir and Freundlich Figure 4.11 also shows that the adsorbed amount of MB on both MnOx-CHBNC and MnOx-KLBNC increases with increasing concentration, but not linearly. Especially, Figure 4.11 b and c show that the adsorption capacity will attain a plateau (saturation) at higher concentrations, especially for MnOx-CHBNC [57]. This suggests that there are a limited number of binding sights available on the adsorbent surface, which are eventually occupied and there is no binding interaction between the MB molecules with each other to form a

multilayer. This is consistent with the monolayer adsorption of Langmuir isotherm model, a common non-linear adsorption at the very high concentrations [195, 196]. The non-linearity behavior suggests that the adsorption process is not only a physical interaction between the MB and the adsorbent surface. There might be chemical interactions involved. MnOx-KLBNC appears to have a higher capacity for MB as compared to MnOx-CHBNC at different initial concentrations.

Table 4.3. Langmuir and Freundlich isotherm constants for adsorption of MB.

Isotherm model	**MnOx-CHBNC**	**MnOx-KLBCN**
Langmuir	y = 0.0253x + 0.0442	y = 0.023x + 0.1281
q_m	39.526	43.478
K_L	0.572	1.000
R_L	0.080	0.048
R^2	0.999	0.991
Freundlich	y = 0.3421x + 2.4149	y = 0.3117x + 2.2975
n	2.923	3.208
K_F	11.189	9.949
R^2	0.679	0.812

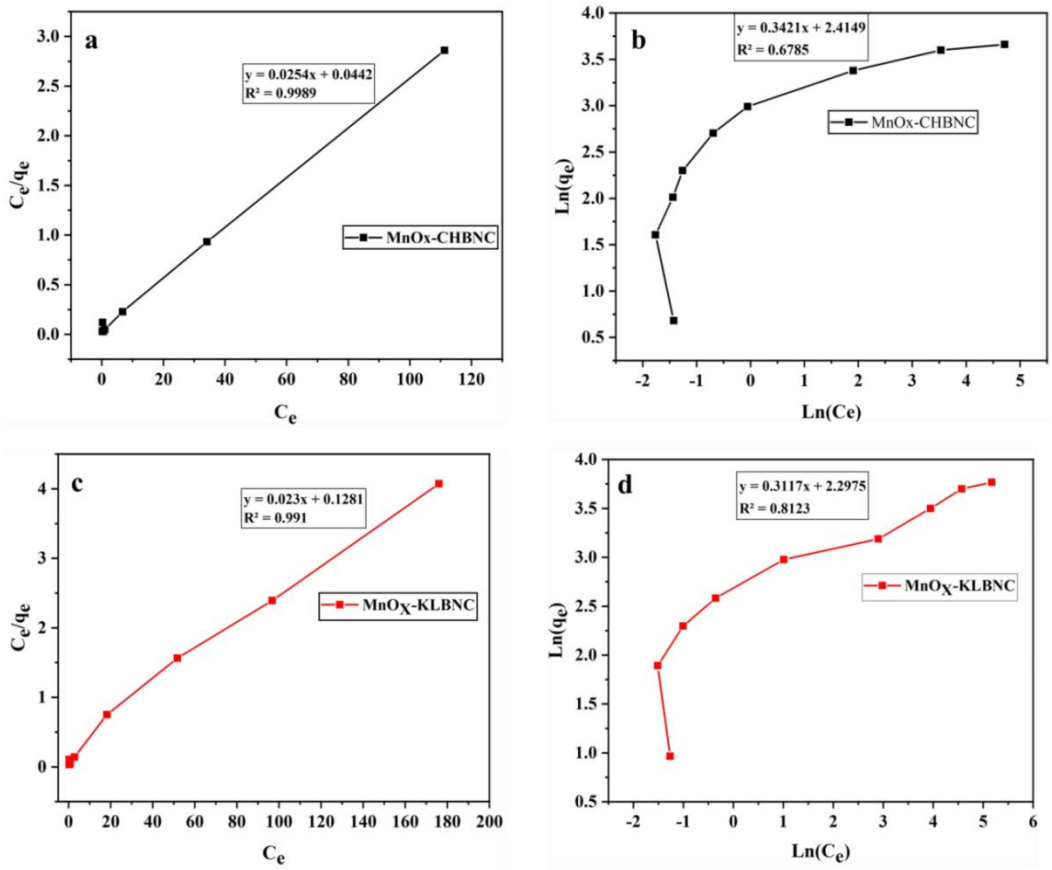

Figure 4.11. (a) Langmuir isotherm for MnOx-CHBNC, (b) Freundlich isotherm MnOx-CHBNC (c) Langmuir isotherm for MnOx-KLBNC (d) Freundlich isotherm MnOx-KLBNC.

Kinetic studies were carried out using 20.0 mL of MB solution with initial concentrations of 20 mg L^{-1}, pH 8, 0.2 g of MnOx-CHBNC, and 0.15 g for MnOx-KLBNC, which was shaken for 5, 10, 20, 30, 40, 60, 80, 120, 180 and 240 min at 200 rpm (25 ºC) following the procedure reported in the literature [54]. Finally, the solutions were centrifuged, and the concentrations of MB in the supernatant were determined. The amount of MB adsorbed onto MnOx-CHBNC and MnOx-KLBNC at time t (q_t) was then calculated as follows:

$$q_t = \frac{(C_o - C_t)V}{m} \qquad (4.6)$$

Where C_o is the initial concentration (mg L^{-1}), C_t is the concentration at time t (mg L^{-1}), V is the volume (L), and m is the mass of adsorbent (g). The following equations are used in the adsorption kinetics models. For the pseudo-first-order adsorption kinetics:

$$\ln(q_e - q_t) = \ln(q_e) - K_1 t \quad (4.7)$$

Where q_e and q_t are the quantities of MB adsorbed (mg g^{-1}) at equilibrium and time t (min), respectively, and K_1 is the pseudo-first-order kinetics rate constant. For pseudo-second-order kinetics

$$\frac{t}{q_t} = \frac{1}{K_2 q_t^{\,2}} + \frac{t}{q_e} \quad (4.8)$$

K_2 represents the rate constant for the pseudo-second-order kinetic adsorption model. Adsorption characteristics, including R^2 and other constants, were determined for both models and are shown in Table 4.4. In this study, the adsorption mechanism was represented by the pseudo-second-order model.

Table 4.4. Constants of pseudo-first and second-order adsorption kinetic models.

Kinetic Model	MnOx-CHBNC	MnOx-KLBNC
$q_{exp.}$	1.976	2.629
Pseudo-first order		
q_e	1.048	1.546
K_1	3.44×10^{-2}	4.20×10^{-3}
R^2	0.886	0.908
Pseudo-second order		
q_e	2.085	2.068
K_2	5.261×10^{-2}	3.458×10^{-2}
R^2	0.998	0.997

4.3.4.7. Comparison of the result with other similar studies

The maximum MB adsorption capacities of some reported adsorbents are described in Table 4.5. The adsorption capacities achieved by the manganese oxide-biochar nanocomposites prepared in this work were higher than some adsorbents reported in previous studies. As a result, MnOx-CHBNC and MnOx-KLBNC are effective adsorbents for removing MB from aqueous solutions. Furthermore, manufacturing biochar nanocomposites from CH and KL is an effective technique to remove potential contaminants from water. CH and KL are alternate, low-cost biomass for biochar

manufacturing, and the process is an appropriate solution for resource recovery and environmental protection. $KMnO_4$ activated biochar production process is more advantageous in terms of its shorter activation time at room temperature, mild reaction with organic materials, forming less ash content biochar, and being more environmentally friendly than other activation processes. So, despite their relatively lower removal efficiencies than the others, MnOx-CHBNC, and MnOx-KLBNC are environmentally preferable.

Table 4.5. Comparison of the MB removal efficiency of some adsorbents from aqueous solution.

Adsorbent	C_o (mg L^{-1})	V_o (mL)	m (g)	q_m (mg g^{-1})	R (%)	Ref.
Fe_3O_4/SDB nanocomposite	30.00	30.00	0.25	25.33	75.00	[8]
H_3PO_4-treated beli biochar	10.00	50.00	0.30	12.32	90.00	[13]
Torrified-*Acacia nilotica* biochar	50.00	50.00	2.00	158.30	ND	[13]
Acacia nilotica biochar	50.00	50.00	2.00	85.68	ND	[13]
Fe_3O_4@C core-shell comp.	20.00	40.00	0.20	42.11	ND	[47]
NaOH-treated coffee husk	37.78	50.00	0.74	200.00	93.52	[183]
NaOH-treated banana stem	25.00	50.00	0.80	0.47	96.59	[185]
Fe_3O_4 nano-powder	20.00	25.00	2.00	25.54	99.69	[164]
Wheat straw-biochar	100.00	10.00	0.60	12.03	ND	[92]
KOH activated CHBC	50	500	0.5	357.38	ND	[197]
MnOx-CHBNC	20.00	20.00	0.20	39.52	99.26	This study
MnOx-KLBNC	20.00	20.00	0.15	43.47	98.20	

4.3.5. Regeneration studies

The result revealed that one advantage of the proposed biochar-nanocomposite adsorbents is easy separation from soluble waste and reusability. The study results are shown in Figure 4.12a and b. Both MnOx-CHBNC and MnOx-KLBNC show a decrease in removal efficiency over multiple cycles. However, MnOx-CHBNC's removal efficiency decreases significantly after three cycles, whereas MnOx-KLBNC's removal efficiency shows a negligible reduction up to six cycles. The difference in reusability may be due to the difference in material properties of CHBNC and KLBNC, which likely refers to different components within the biochar-nanocomposite adsorbents. KLBNC might have a stable structure or more favorable interaction with the target nanomaterial (MnOx) compared to CHBNC, leading to better retention during multiple adsorption/desorption cycles. CHBNC might degrade or leach out during the cycling, reducing the number of binding sites available for MB. KLBNC, on the other hand, might be more resistant to such degradation. Therefore, MnOx-KLBNC better reusability compared to the other adsorbent.

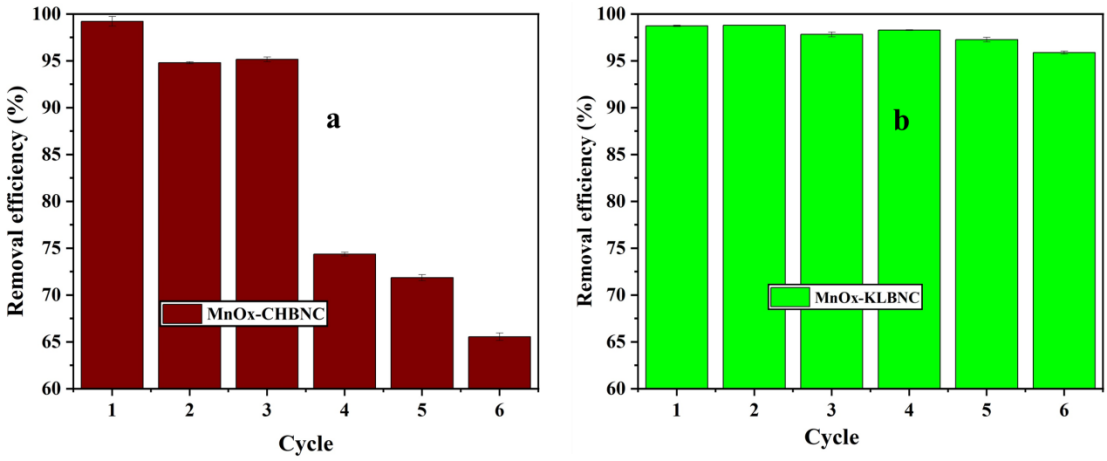

Figure 4.12. Regeneration of (a) MnOx-CHBNC and (b) MnOx-KLBNC for removal of MB from aqueous solution.

4.4. Summary

In this work, CH and KL, biochar-based MnOx nanocomposites (MnOx-CHBNC and MnOx-KBNC) were prepared by pyrolysis and used to remove MB from an aqueous solution. When 25 g of each biomass was pretreated with 12.5 mmol of $KMnO_4$ (2:1 g $mmol^{-1}$ ratio) and pyrolyzed at 300 ℃ for 1 h, they showed the highest MB removal

efficiency. The Pristine biochars (CHB and KLB) and their corresponding MnOx-CHBNC and MnOx-KLBNC are porous, amorphous structures. Nonetheless, MnOx-activated BNCs exhibit more porous structures, larger specific areas, total pore volumes, and smaller pore diameters than their pure biochar counterpart. The functional groups in Pristine and MnOx-activated biochars include O-H, C-H, C=C, and C-O, which may engage in adsorption via electrostatic interaction. The adsorption-desorption isotherm and BET measurements demonstrated that the adsorbents have a mesoporous structure.

Various parameters affecting the adsorption efficiencies of MnOx-CHBNC and MnOx-KLBNC including, contact time, adsorbent dose, initial concentration, and pH, were also studied. We observed that the pH of a solution had an insignificant effect on the adsorption efficiencies of the adsorbents; thus, pH 8 was used for running the experiment. The optimum settings for other parameters were contact time, 60 min, and adsorbent dose, 0.15 g for MnOx-KLBNC and 0.2 g for MnOx-CHBNC.

The equilibrium adsorption investigations revealed that MnOx-CHBNC and MnOx-KLBNC provided the greatest fit for the Langmuir isotherm model. The kinetic studies result also revealed that the adsorption mechanism of MB on both adsorbents followed the pseudo-second-order model. Compared to MnOx-CHBNC, MnOx-KLBNC demonstrated better stability, showing little change in relative adsorption efficiency up to six cycles.

In general, based on the benefits of MnOx-CHBNC and MnOx-KLBNC, such as their ease of manufacture, cheap cost, regeneration cycle, and environmental friendliness, they may be employed as an alternative MB removal adsorbent. Furthermore, this finding might provide preliminary support to the scientific community, who are interested in investigations to increase the removal effectiveness of MB using MnOx-CHBNC and MnOx-KLBNC.

CHAPTER FIVE

5. MnOx-COFFEE HUSK AND KHAT LEFTOVER BIOCHAR NANOCOMPOSITES FOR REMOVAL OF CHROMIUM (VI) FROM WATER

5.1. Introduction

Toxic heavy metal emissions from industries such as tanneries, textiles, breweries, metallurgy, dyeing factories, and agro-processing pollute surface water, groundwater, agricultural soils, and food crops, posing severe and chronic health dangers to the population via various ways [3]. The United States Environmental Protection Agency (US EPA) considers chromium to be a priority pollutant [21]. In nature, Cr occurs primarily as Cr(III) and Cr(VI), with Cr(VI) being significantly more toxic, soluble in water, and mobile than Cr(III). Furthermore, hydrophytes can absorb Cr(VI) and leak it into groundwater, causing hazardous and negative repercussions for humans [22]. Therefore, it is vital to use suitable treatment processes before dumping industrial effluents into the environment.

Several physical and chemical approaches have been employed to remove Cr(VI) from wastewater, including electrochemical [25], ultrafiltration [38], ion exchange [26], chemical precipitation [40], coagulation [42], and adsorption [30]. However, each approach has inherent drawbacks, including high energy consumption, expense, hazardous sludge formation, partial treatment, and reagent usage [7]. Adsorption, among existing technologies, is a potential strategy to remove heavy metal ions from contaminated water because of its low cost, high removal efficiency, and simplicity of regeneration [31].

This study evaluated the effectiveness of MnOx-KLBNC and MnOx-CHBNC, which were synthesized and characterized according to the procedures stated in Chapter 4. The study examined the Cr(VI) adsorption capacities of two adsorbents by analyzing the effects of contact time, adsorbent dose, concentration, and pH, as well as the kinetics and adsorption isotherms. Furthermore, the study performed desorption tests of Cr(VI) from MnOx-CHBNC and MnOx-KLBNC to investigate the adsorbents' regeneration or reusability.

Kochito, J.; Femi, O. E; Beyene, T. T.; Abdissa, N.; Gure, A. Manganese oxide-coffee husk and khat (*Catha edulis)* leftover biochar nanocomposites for removal of Cr (VI) from wastewater. *Bull. Chem. Soc. Ethiop.* **2024**, 38(5) *(accepted to be published)*

5.2. Experimental

5.2.1. Batch adsorption studies

Preliminary adsorption experiments were conducted to examine the effectiveness of four adsorbents, KLB, CHB, MnOx-KLBNC, and MnOx-CHBNC in removing Cr(VI) from an aqueous solution following the procedure described in the literature [176].

During the analysis, five concentrations of Cr(VI) were prepared by diluting the 1000 mg L^{-1} stock standard solution of Cr(VI) that had been previously prepared by dissolving 2.83 g of $K_2Cr_2O_7$ in deionized water [198]. To conduct the isotherm studies, a solution containing initial Cr(VI) concentrations ranging from 10 to 100 mg L^{-1} was mixed with 0.10 g of the adsorbent materials. The kinetics were studied using initial concentrations of 20, mg L^{-1} of Cr(VI) at pH 2, using 0.1 g of each MnOx-CHBNC and MnOx-KLBNC separately. After shaking the mixture on the horizontal shaker at 200 rpm, the content was filtered using Whatman filter paper. Then, 1 mL of DPC solution, which had been prepared earlier by dissolving 0.25 g of DPC in 50 mL acetone and diluting to 100 mL with deionized water [153], was added to the filtrate and kept for 10 min. The absorbance of the solutions was then determined using a UV-Vis spectrophotometer at the monitoring wavelength of 540 nm [39, 76, 199].

The Cr(VI) removal efficiency (R) for each adsorbent was calculated using Equation 4.1, and the adsorption capacity (q_e) was determined employing Equation 4.2 as described in section 4.2.2.

5.2.2. Reusability of the adsorbents

Six successive adsorption-desorption cycles at 25±1 ℃ were conducted to assess the adsorbents' reusable nature [200]. Adsorption was carried out in each cycle by shaking 2 g of MnOx-KLBNC and MnOx-CHBNC dispersion in 250 mL of Cr(VI) solution with an initial concentration of 20 mg L^{-1} for 120 min at pH 2. For desorption, Cr(VI) loaded adsorbent was spread in 100 mL of 0.1M KOH, agitated for 120 min, and filtered. After each adsorption-desorption cycle, MnOx-KLBNC and MnOx-CHBNC adsorbents were rinsed with deionized water, dried at 70 ℃ for 2 h, and applied for the next round [44].

5.3. Results and Discussion

5.3.1. Adsorbent characterization

FTIR spectroscopy was used to detect the presence of various surface functional groups, such as amino, carbonyl, carboxyl, and so on [201]. Figures 5.1a and b show the results of the FTIR tests for CHB, MnOx-CHBNC, KLB, and MnOx-KLBNC. The findings indicate that functional groupings such as O-H (3417-3426 Cm^{-1}), C-H (2853-2920 Cm^{-1}), C=C (1611-1622 Cm^{-1}), and C-O (1411-1466 Cm^{-1}) are detected [29, 168, 184]. The peaks at 437 and 525 cm^{-1} in MnOx-CHBNC, as well as strong peaks at 464, 545, and 781 cm-1 in MnOx-KLBNC, characterize the bonds in R-MnOx, confirming the presence of MnOx in activated biochar [202]. It implies that the functional groups are involved in Cr(VI) adsorption due to their electrostatic interaction [203]. The broader peaks of O-H observed in MnOx-CHB and MnOx-KLBNC are due to the detection of the -OH group in moisture [52].

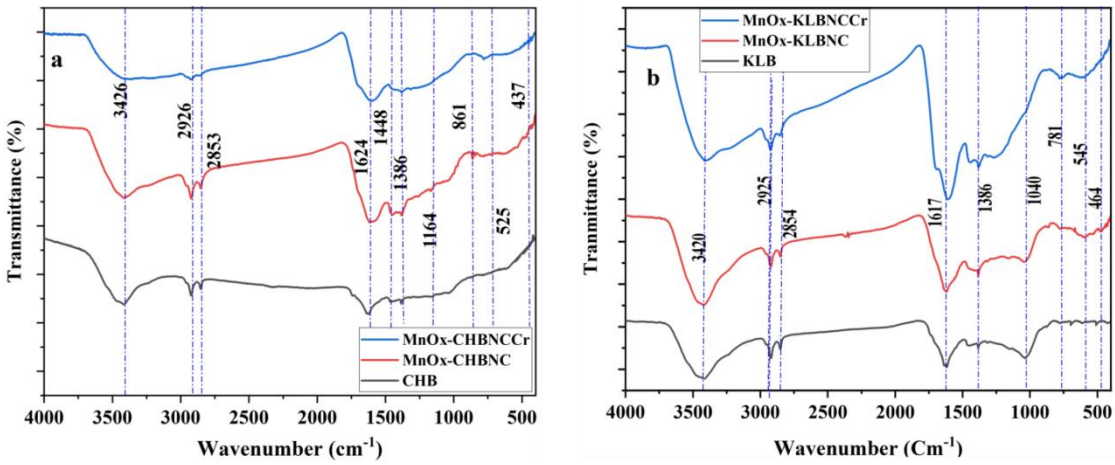

Figure 5.1. FTIR spectra of (a) CHB, MnOx-CHBNC and MnOx-CHBNCCr and (b) KLB, MnOx-KLBNC and MnOx-KLBNCCr.

5.3.2. Batch adsorption studies

Preliminary tests were conducted to select an adsorbent for removing Cr(VI) from an aqueous solution. The results showed that CH, KL, MnOx-CHBNC, and MnOx-KLBNC exhibited varying efficiencies in removing Cr(VI). The Cr(VI) removal efficiencies of CH and KL biochars were lower than those of their MnOx-nanocomposites: MnOx-CHBNC, and MnOx-KLBNC, which removed 74.98% and 84.78% of Cr (VI) from the

aqueous solution respectively. Therefore, MnOx-CHBNC and MnOx-KLBNC were chosen for removing Cr(VI) from water. The parameters that can affect the Cr(VI) adsorption capacity of MnOx-CHBNC and MnOx-KLBNC were investigated at a constant temperature of 25±1 ℃.

5.3.2.1. Effect of contact time

Contact time is one of the variables that influence adsorption capacity. According to reports, as contact duration increases, so does the adsorption capacity [203]. Figure 5.2 demonstrates that Cr(VI) adsorption on the prepared materials proceeded quickly in the early phases. It then gradually increased after 20 min and stayed rather steady after 60 min for both MnOx-CHBNC and MnOx-KLBNC. The results indicate that adsorption takes place rapidly at the beginning due to the availability of sufficient adsorption surface sites, but the rate slows down over time up to equilibrium is reached. The remaining adsorption sites face barriers to ongoing adsorption due to repulsive interactions between solute molecules adsorbed on the adsorbent and in the bulk solution phase [163]. Based on Figure 5.2, the optimal contact time was 60 min, which was subsequently used for further studies.

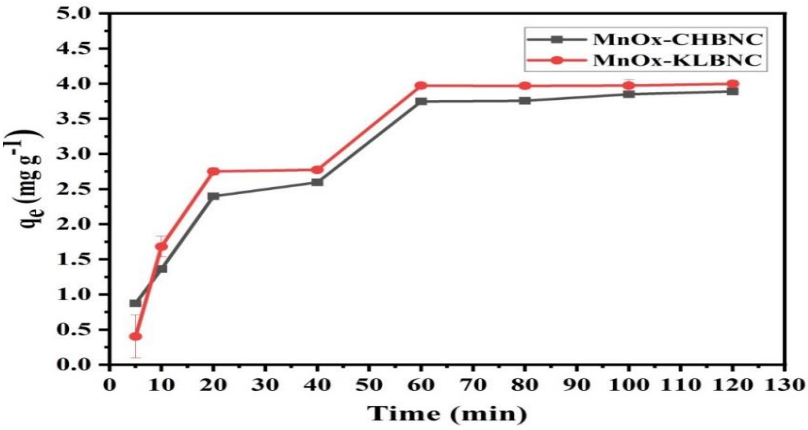

Figure 5.2. The effect of contact time on the adsorption capacity of MnOx-CHBNC and MnOx-KLBNC to remove Cr(VI) from water.

5.3.2.2. The effect of adsorbent dose

The impact of dosage on the capacities of the adsorbents to remove Cr(VI) was investigated using 0.05, 0.1, 0.15, 0.2, 0.25, 0.3, 0.4, and 0.5 grams of adsorbent per 20

mL of the solution [204]. Figures 5.3a and b indicate that the removal efficiencies of Cr(VI) and adsorption capacity vary significantly with the doses of MnOx-CHBNC and MnOx-KLBNC. It can be observed that increasing the dose of MnOx-KLBNC and MnOx-CHBNC from 0.05 to 0.10 g resulted in a considerable improvement in Cr(VI) removal efficiency, which remained relatively uniform above 0.10 g. The rise in removal efficacy with increasing adsorbent dose is because of the availability of new binding sites for Cr(VI) adsorption, which achieves saturation at a specific dosage level. Thus, 0.10 g of MnOx-KLBNC and MnOx-CHBNC per 20 mL, were chosen for the subsequent investigations.

Adsorption capacity decreased as the adsorbent dose increased (Figure 5.3a and b). When the doses of MnOx-CHBNC and MnOx-KLBNC were raised from 0.05 to 0.5 g per 20 mL, the q_e value fell drastically. As a result, the slope of the adsorption capacity curve was reduced. Because when the amount of adsorbent is minimal, active adsorption sites interact fast with adsorbates, approaching saturation. When the amount of adsorbent exceeds a certain limit, more adsorption sites fail to establish contact with adsorbate molecules [188]. Furthermore, when the number of adsorbents increases, they are more likely to combine, diminishing the adsorbents' specific surface area [187].

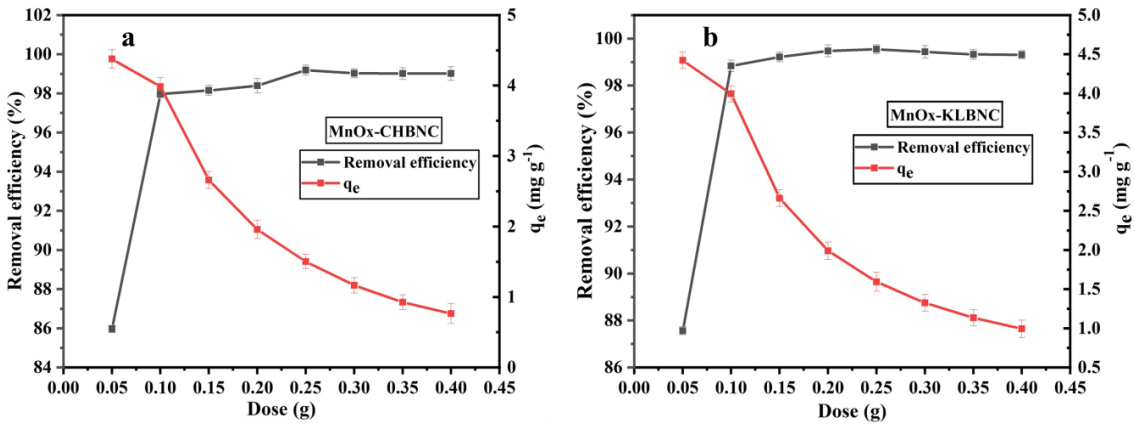

Figure 5.3. The effect of adsorbent dose on the removal efficiency, and the adsorption capacity of (a) MnOx-CHBNC and (b) MnOx -KLBNC to remove Cr(VI) from water.

5.3.2.3. The effect of initial concentration

The study investigated the effect of initial concentration and isotherm models on concentrations ranging from 10-100 mg L^{-1}. The remaining conditions were fixed (pH 2,

adsorbent dosage 0.1 g, and contact period 60 min). Figure 5.4a shows how the adsorption effectiveness varies with the initial Cr(VI) concentration. The results demonstrated that the adsorbents' Cr(VI) adsorption capability increased as the starting Cr(VI) concentration rose. The adsorption capacity of MnOx-CHBNC increased from 3.97-11.55 mg g^{-1}, while that of MnOx-KLBNC from 3.97 - 15.15 mg g^{-1}. It seems that the adsorption of ions occurs more rapidly when the starting concentration is higher. This is due to the greater driving force required for the mass transfer of Cr(VI) ions. Additionally, solutions with high initial concentrations required a longer time to reach equilibrium. Because, towards the end of the adsorption process, most sorbate ions penetrate the porous structure of the adsorbent as its surface becomes saturated [205].

Conversely, when the concentration of Cr(VI) increases, the removal efficiency falls. At optimum adsorption parameters, MnOx-CHBNC and MnOx-KLBNC removed about 99.63% and 99.84%, respectively. At Cr(VI) concentrations greater than 20 mg L^{-1}, the removal efficiency of MnOx-CHBNC and MnOx-KLBNC decreased dramatically. MnOx-KLBNC removed Cr(VI) more efficiently than MnOx-CHBNC, especially at higher starting concentrations. Removal effectiveness increases with lower Cr(VI) concentrations due to greater ion mobility in dilute solutions. Meanwhile, when the initial concentration has been elevated with the constant adsorbent mass, the drop in adsorption effectiveness might be caused by the scarcity of active sites for binding Cr(VI) [30].

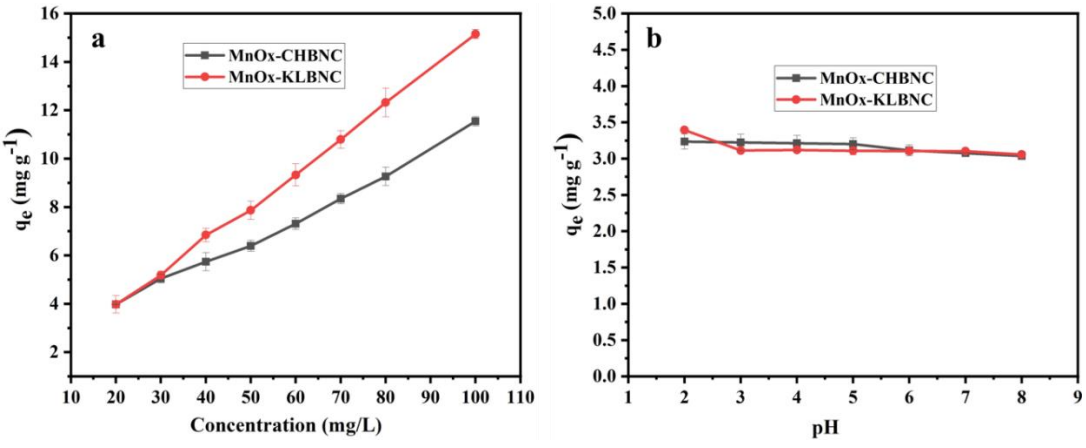

Figure 5.4. The effect of (a) initial concentration and (b) pH on the Cr(VI) adsorption capacity of MnOx-CHBNC and MnOx-KLBNC.

5.3.2.4. The effect of pH

In general, the pH of the solution influences adsorption processes, which is the result of functional groups of the adsorbent, and changes in the absorbent's surface charge [191]. The influence of pH on Cr(VI) adsorption was studied across the pH range of 2 to 8. The solutions' pH was adjusted using 0.10 M HNO_3 and 0.10 M NaOH solutions [14]. Figure 5.4b shows how the pH affects the Cr(VI) adsorption capability of MnOx-CHBNC and MnOx-KLBNC. The investigation used an initial Cr(VI) content of 20 mg L^{-1}, an adsorbent dosage of 0.10 g for MnOx-CHBNC and MnOx-KLBNC per 20 mL, at a temperature of 25$\pm$1 ℃, and a contact time of an h. The results showed that the adsorption capacity is sensitive to pH changes and relatively the highest values were observed when the pH of the Cr(VI) solution was 2. Thus, pH 2 was chosen as the optimum value in further studies. The pH of the solution influences the competition between Cr(VI) ions with adsorbent and additional OH^-/H^+ ions in the solution, resulting in fluctuations in Cr(VI) adsorption capacity.

5.3.2.5. Effect of temperature and thermodynamics study

The study aimed to explore how temperature affects the efficiency of Cr(VI) adsorption by two different adsorbents, MnOx-CHBNC and MnOx-KLBNC, at three different temperatures: 25°C, 35°C, and 45°C. The findings show that the efficiency of both adsorbents decreased as the temperature increased, indicating that the adsorption process is exothermic. This conclusion was confirmed by the negative ΔH obtained from the thermodynamic analysis. Table 5.1 presents the thermodynamic parameters, such as ΔH, ΔG, and ΔS, which were analyzed using a plot of 1/T on the x-axis versus $\ln(K_L)$ on the y-axis. The slope and intercept of the plot were equal to ΔS/R and –ΔH/R, respectively. Here, T represents the temperature in Kelvin, K_L is a ratio (q_e/c_e) of the concentration of Cr(VI) in the solid and liquid phases, and R is the universal gas constant. ΔG represents the change in free energy, ΔH represents the change in enthalpy, and ΔS represents the change in entropy. The negative value of ΔG indicates that the adsorption process is spontaneous.

Table 5.1. Thermodynamic behavior of adsorption of Cr(VI) on MnOx-CHBNC and MnOx –KLBNC.

	Temp. (K)	**K_L**	**ΔG (KJ /mol^{-1})**	**ΔH (KJ mol^{-1})**	**ΔS (KJ K^{-1} mol^{-1})**	**R^2**
MnOx-CHBNC	298	29.25	-8.364	-99.835	-3.079	0.971
	303	5.444	-4.339			
	318	2.340	-2.472			
MnOx-KLBNC	298	23.53	-7.825	-84.553	-2.582	0.981
	303	5.978	-4.579			
	318	2.767	-2.690			

5.3.2.6. Adsorption isotherm and kinetics model

The adsorption equilibrium was examined by fitting the experimental data to the linear equations of the Langmuir (Equation 4.3) and Freundlich (Equation 4.4) isotherm models [6], as indicated in section 4.3.4.6. The adsorption or distribution coefficient (K_F) measures the number of ions adsorbed onto the surface of the adsorbent particle. The value of 1/n represents surface heterogeneity, which increases as the number approaches zero [194]. The Langmuir isotherm predicts the affinity between adsorbate and sorbent using a dimensionless constant known as the separation factor R_L, as shown in Equation 4.5 as described in section 4.3.4.6. The value of R_L ranges from 0 to 1 for favorable adsorption, whereas $R_L > 1$ indicates unfavorable adsorption, $R_L = 1$ indicates linear adsorption, and $R_L = 0$ indicates irreversible adsorption [194].

Adsorption isotherms describe the adsorbate concentration and capacity at a given adsorbent dosage and temperature [7]. Evaluation of these isotherms also leads to a better understanding of adsorption processes, which are affected by properties like surface polarity, surface area, and porosity. The linear versions of the Langmuir and Freundlich isotherm models were employed to quantify the equilibrium adsorption data [193]. The Langmuir isotherm represents monolayer adsorption on a homogenous surface with consistent active sites.

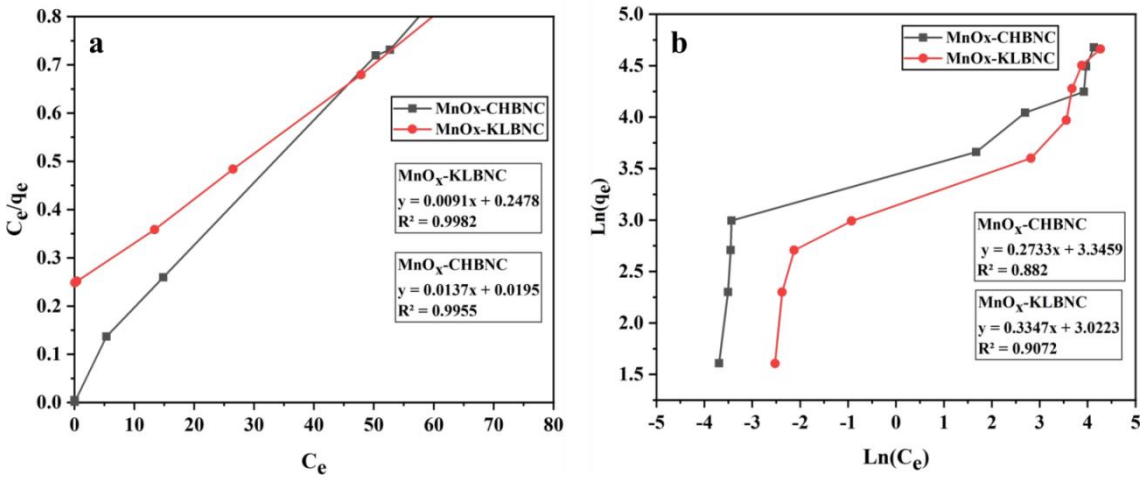

Figure 5.5. (a**)** Langmuir isotherm for MnOx-CHBNC and MnOx-KLBNC and **(**b) Freundlich isotherm MnOx-CHBNC and MnOx-KLBNC.

Figure 5.5 and Table 5.2 illustrate the Langmuir and Freundlich isotherm parameters, as well as their correlation coefficients. A higher correlation coefficient (R^2) implies that the Langmuir model is more applicable (R^2 = 0.996 for MnOx-CHBNC and R^2 = 0.998 for MnOx-KLBNC), demonstrating monolayer adsorption on a particular spot of the adsorbent's homogenous surface [9]. The Langmuir isotherm predicts that adsorption energy is homogenous on the adsorbent surface and that the adsorbed molecules do not interact [13]. The low separation factor values (R_L = 0.258 for MnOx-CHBNC and R_L = 0.520 for MnOx-KLBNC) point to a favorable physical adsorption process. The Freundlich isotherm displays multilayer adsorption for heterogeneous surfaces or surface-supporting locations with varying affinities [184]. The computed n values, which range from 1 to 10, suggest favorable sorption. Furthermore, the Langmuir isotherm model has a higher regression coefficient R^2 than the Freundlich model (Figures 5.5a and b), indicating that the Langmuir model gives a better description, and these findings point to monolayer Cr(VI) adsorption on the surfaces of both adsorbents.

Table 5.2. Langmuir and Freundlich isotherm constants for adsorption of Cr(VI).

Isotherm model	MnOx-CHBNC	MnOx-KLBNC
Langmuir	y = 0.0137x + 0.0195	y = 0.0091x + 0.2478
q_m	72.993	109.890
K_L	0.144	0.037
R_L	0.258	0.520
R^2	0.996	0.998
Freundlich	y = 0.2733x + 3.3459	y = 0.3134x + 2.9906
n	3.659	3.191
K_F	28.386	19.898
R^2	0.882	0.9268

Kinetic tests were conducted on the solution at initial concentrations of 20 mg L^{-1} at pH 2 with 0.1 g of MnOx-CHBNC, and MnOx-KLBNC per 20 mL. The study investigated the effects of time over a period ranging from 5 to 240 min. The solutions were filtered after shaking at 200 rpm for the appropriate duration, and their Cr(VI) concentrations were measured. Equation 4.6 indicated in section 4.3.4.6 was used to compute the adsorbed quantity of Cr(VI) on CHBNC and KBNC at time t (q_t).

The adsorption kinetics models were analyzed based on the Equation 4.7 described at section 4.3.4.6 depicts the pseudo-first-order adsorption kinetics, while Equation 4.8 was used to evaluate the pseudo-second-order kinetics.

Table 5.3 shows the adsorption parameters for both models, including R^2 and other constants. In this study, the adsorption mechanism was better described by the pseudo-first-order model. It implies that the rate-limiting step in the adsorption is the mass transfer from the bulk solution to the adsorption sites on the adsorbent surface. The adsorption rate depends on the concentration difference between the adsorbate in solution and the unoccupied sites on the adsorbent. The model is more associated with physisorption than chemisorption [30].

Table 5.3. Constants of pseudo-first and second-order adsorption kinetic models.

Kinetic Model	MnOx-CHBNC	MnOx-KLBNC
$q_{exp.}$	3.985	3.993
Pseudo-first order		
q_e	3.878	3.755
K_1	5.10×10^{-2}	2.51×10^{-2}
R^2	0.985	0.998
Pseudo-second order		
q_e	4.364	3.987
K_2	3.90×10^{-1}	6.613×10^{-1}
R^2	0.783	0.969

5.3.2.7. Comparison with other similar studies

Table 5.4 describes the maximal adsorption capacity and Cr(VI) removal efficiency of various previously reported adsorbents. The MnOx-CHBNC and MnOx-KLBNC produced in this study have better adsorption capabilities than some adsorbents but lower than others. However, the comparison shows that the amount (mass) of adsorbents employed in this study is lower than in the prior publications shown in Table 5.4. As a result, the MnOx-CHBNC and MnOx-KLBNC are viable adsorbents for removing Cr(VI) from aqueous solutions. Preparing biochar-nanocomposites from the CH and KL is an effective technique to remove potential contaminants and create valuable treatment products. CH and KL are the most cost-effective feedstock for biochar manufacturing, and the technology is appropriate for resource recovery and environmental conservation.

Table 5.4. Comparison of the Cr(VI) removal efficiency of some adsorbents from aqueous solution.

Adsorbent	C_o (mg g^{-1})	Volume (mL)	m (g)	q_m (mg g^{-1})	% Removal	Ref.
ZnO-bagasse biochar	50.00	50.00	0.10	102.66	92	[21]
FeS-wheat straw biochar	50.00	42.00	0.72	150.00	95	[153]
Magnetic woodchip biochar	10.00	50.00	0.50	80.96	95	[200]
Activated shaddock biochar	20.00	25.00	0.05	9.95	99.2	[205]
Modified corn stalk biochar	50.00	50.00	0.10	25.68	ND	[31]
Clay-$MnFe_3O_4$ composite	10.00	25.00	0.10	178.60	98.65	[162]
MnOx-CHBNC	20.00	20.00	0.10	72.99	99.63	This
MnOx-KLBNC	20.00	20.00	0.10	109.84	99.89	study

5.3.2.8. Reusability of the adsorbents

The suggested biochar-nanocomposite adsorbents have the advantage of being easily separated from soluble waste and reusable. The findings of this investigation are shown in Figures 5.6a and b. The study found that in the recycling of the sorbent after the first use, the relative adsorbent capacity of MnOx-CHBNC was 99.37% and 99.83% for MnOx-KLBNC. After six cycles, the results dropped marginally to 95.12%. The results indicate that MnOx-CHBNC and MnOx-KLBNC show promising Cr(VI) adsorption capabilities during the sixth cycle. Due to their affordability, ease of preparation, and ability to be multiple times reusable, both adsorbents could be utilized for Cr(VI) removal.

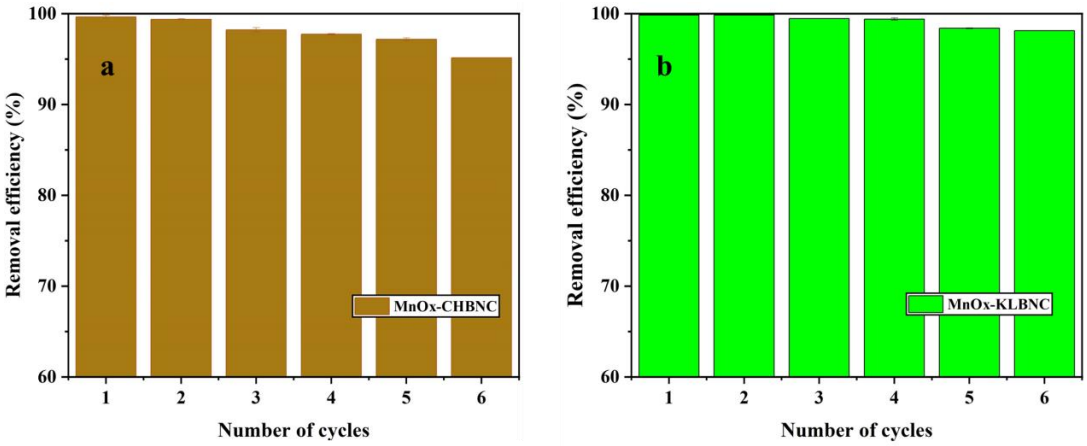

Figure 5.6. Reusability of (a) MnOx-CHBNC and (b) MnOx-KLBNC to remove Cr(VI) from aqueous solution.

5.4. Summary

Pristine biochar of CH, generated by pyrolysis of biomass at 300 ℃, eliminates 74.98%, whereas that of KL removes 84.78% Cr(VI) from 20 mgL^{-1} aqueous solutions. MnOx-CHBNC and MnOx-KLBNC, synthesized by pretreating every 25 grams of dried biomass with 12.5 mmol of $KMnO_4$ and pyrolyzed at 300 ℃ for an h, had an efficiency of 99.63% and 99.84%, respectively, to remove Cr(VI) from 20 mgL^{-1} aqueous solution by employing each 0.1 g of MnOx-CHBNC and MnOx-KLBNC in 120 min. The highest removal efficiencies and adsorption capacities were examined by optimizing factors such as the adsorbent dosage, pH, contact time, and initial concentration.

Equilibrium results fit well into the Langmuir isotherm equation, demonstrating that the monolayer adsorption mechanism of Cr(VI) onto adsorbents is dominant. The linearity of the graphs has been evaluated for the Langmuir and Freundlich isotherms in both adsorbents. The Langmuir isotherm has R_L values ranging from zero to one, indicating favorable adsorption. Cr(VI) adsorption was determined to follow a pseudo-first-order model in which adsorption is dependent on adsorption site availability. The findings of this study validated the effectiveness of the suggested approach for recycling coffee husk and khat waste and preparing low-cost carbon materials. This lab-scale data can serve as baseline data for further study to design improved treatment facilities to clear effluents containing Cr(VI).

CHAPTER SIX

6. MAGNETIC IRON-OXIDE COFFEE HUSK AND KHAT WASTE BIOCHAR NANOCOMPOSITES FOR REMOVAL OF METHYLENE BLUE FROM AQUEOUS SOLUTION

6.1. Introduction

MB is an organic dye widely used for coloring paper, printing cotton, dyeing leather, and plastics [12, 14, 16]. However, prolonged exposure to MB can have harmful effects, and the discharge of untreated industrial effluents containing dyes can pose significant environmental threats. In Chapter 4, we discussed various methods used in the past for removing MB from water and their limitations. Adsorption is the appropriate and beneficial method to remove MB from water. The efficiency of the adsorption process largely depends on the type of adsorbent material used [34].

Some reports show that magnetic iron oxide is used to improve the MB adsorption properties of biochar [138, 160, 161]. For instance, Fe_3O_4 biochar nanocomposites of sawdust, rice husk, and palm oil empty fruit bunch are investigated with higher removal efficiency than their pristine biochar. Also, Fe_3O_4 nanocomposite of activated carbon [10, 161], carbon core-shell [164], and besides this metal-free activated spent coffee ground [162, 163], are employed for MB removal. However, any investigation has not reported about employing Fe_3O_4-CHBNC and Fe_3O_4-CHBNC biochar nanocomposites for MB removal.

The objective of this study was to evaluate the conversion of coffee husk and khat leftovers into useful products, providing dual advantages. These products can remove toxic pollutants from water and economically dispose of biomass waste. Fe_3O_4-CHBNC and Fe_3O_4-KLBNC were produced, and characterized. Then their MB removal efficiencies were evaluated. The study evaluated the impact of contact time, adsorbent dosage, initial concentration, and pH on the adsorption capacity of Fe_3O_4-CHBNC and Fe_3O_4-KLBNC for MB, and assessed the kinetics and adsorption isotherms. Desorption studies of MB from the Fe_3O_4-CHBNC and Fe_3O_4-KLBNC were conducted to evaluate the regeneration or reusability of the adsorbents.

Kochito, J.; Gure, A.; Abdisa, N.; Tadesse, T.; Femi, O. E. Magnetic Iron-oxide Coffee Husk and Khat Waste Biochar Nanocomposites for Removal of Methylene Blue from Aqueous Solution. *Sep. Sci. Plus.*, **2024**, 2300246.

Finally, it was concluded that the findings of this study supported the effectiveness of the suggested approach for recycling KL and CH as well as for preparing low-cost carbon material. The result of batch adsorption and lab-scale data can serve as preliminary support for the scientific community interested in conducting studies such as continuous column adsorption and at designing treatment plants that effectively remove MB dye-containing effluents.

6.2. Experimental

6.2.1. Synthesizing magnetic biochar nanocomposites from CH and coffee KL

The KL was chopped into small pieces, cleaned with tap water, rinsed with distilled water, dried at 105 °C for 24 hs, ground into 2 mm powder, and stored [138, 172]. Similarly, the CH was cleaned, dried, ground, and preserved.

The modified method described by Chen, Zhang, Fang, Zheng, and their colleagues were used to synthesize biochar nanocomposite materials. Note that, 25 g of each biomass powder was submerged in 300 mL of an aqueous solution containing each 12.5 mmol of FeS and $FeCl_3$ with a 1:1 molar ratio [136, 172–175]. The mixture was stirred for one h at 30 °C, and then the water was evaporated completely in an oven at 80 °C until the weight remained constant. After being dried, the sample was placed in a crucible container, covered with aluminum foil, and placed inside a muffle furnace that had been preheated to 110 °C. It was kept at 110 °C for 30 min, the sample was heated to 300 °C using a heating ramp of 10 °C per min. Ultimately, it was pyrolyzed for one h at 300°C. Next, the biochar-metal oxide or hydroxide composite was cooled to room temperature, ground, and sieved using a mesh size of 0.2 mm. Similarly, a 25 g sample of dried biomass powder was used to synthesize pristine biochar. Lastly, distilled water was used to clean up soluble materials. It was then oven-dried at 80 °C and stored in a plastic container that was tightly sealed. The labels CHB, KLB, Fe_3O_4-CHBNC, and Fe_3O_4-KLBNC were used for the prepared pure biochar and nanocomposites.

6.2.2. Batch adsorption studies

To evaluate the MB removal efficiencies of CHB, KLB, Fe_3O_4-CHBNC, and Fe_3O_4-KLBNC, preliminary adsorption tests were carried out [176]. The rate and adsorption equilibrium phenomena associated with MB adsorptions were assessed through batch experiments. One gram of MB was dissolved in deionized water to prepare the stock solution of 1000 mg L^{-1} MB. Different concentrations of MB were then prepared for the following investigations [177, 193]. To conduct the isotherm tests, 0.10 g of biochar was added to the initial MB concentration solution, which ranged from 10 to 500 mg L^{-1}. The Kinetics studies were conducted at 25± °C with a 20 mg L^{-1} MB solution. The horizontal shaker was used to shake the adsorbent-solution mixtures at 200 rpm. The concentration of MB in the supernatant solutions was then measured by centrifuging the mixtures and utilizing the absorbance response UV-Vis spectrophotometer at λ = 665 nm. The efficiency (R) of MB removal for each adsorbent was computed using equation (4.1), and the materials' MB adsorption capacity (q_e) was ascertained using equation (4.2) as described in section 4.2.2 [177].

6.2.3. Regeneration of the adsorbents.

To assess the regeneration of the adsorbents, six cycles of recurrent adsorption and desorption processes were done at 25±1 °C following the adapted experimental design reported by Păcurariu and coworkers [8]. For each cycle, 2 g of Fe_3O_4-CHBNC and Fe_3O_4-KLBNC were separately dispersed in 200 mL of 20 mg L^{-1} MB solution by shaking for 120 min at pH 7.5. Then it was centrifuged, and the concentrations of MB in the supernatant were analyzed. For desorption, 2 g of the MB-loaded adsorbents were dispersed in 50 mL of 50% ethanol at a pH of 6.5. Following each series, the Fe_3O_4-CHBNC and Fe_3O_4-KLBNC adsorbents were cleaned with distilled water, dried for 2 h at 70 °C, and then recycled for the next procedure.

6.3. Results and Discussion

6.3.1. Adsorbent characterizations

The patterns of XRD diffraction for Fe_3O_4-KLBNC, Fe_3O_4-CHBNC, KLB, and CHB are shown in Figure 6.1. According to the result, the biochar's broad peak and non-plane pattern verify that it contains lignin, natural cellulose, and non-crystalline hemicelluloses. The diffraction peak that was assigned to natural cellulose at 22.4º and appeared at 2θ = 16.1º confirms this [137]. Previous studies verify that C=O-C, C-O, and OH groups in the biochar, as well as unconverted cellulose, are the causes of the large d-spacing in the XRD peaks of the biochar [153]. According to the study reported by An and coworkers, the peaks observed at 33.5º, and 35.6º in Fe_3O_4-CHBNC and Fe_3O_4-KLBNC revealed the presence of Fe_3O_4 [31]. Therefore, the more straight nature of the XRD diffraction patterns of Fe_3O_4-CHBNC and Fe_3O_4-KLBNC than that of CHB and KLB is due to the presence of Fe_3O_4. In general, this result shows that both pure and magnetized CH and KL biochar are amorphous.

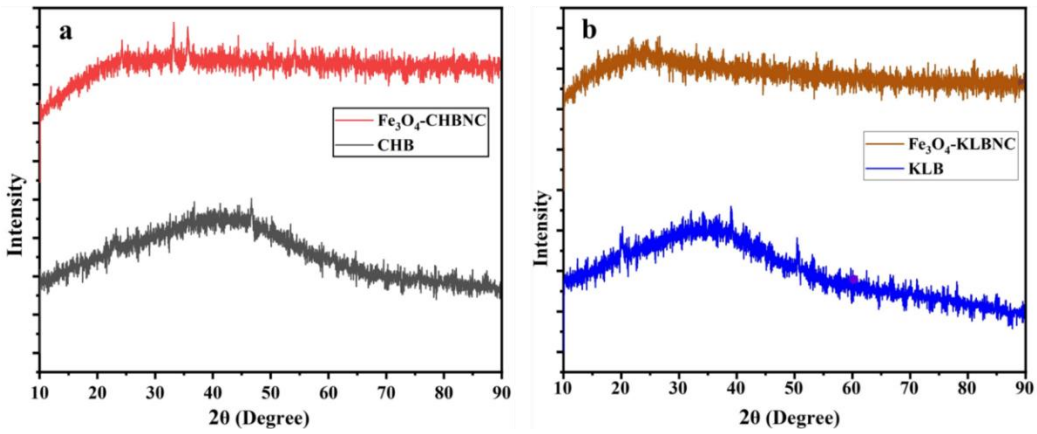

Figure 6.1. XRD patterns of (a) CHB and Fe_3O_4-CHBNC and (b) KB and Fe_3O_4-KLBNC.

Figure 6.2 displays the SEM images that were obtained to examine the morphological changes and textural characteristics of the pristine and activated biochar synthesized from KL and CH. These images verified the heterogeneous and amorphous structures of the biochar. Porosity was seen in every biochar sample. The pyrolysis process resulted in the formation of channel structures and the escape of volatile substances, which led to the formation of pores [182]. Figures 6.2b and d show that pore structure formations are more

noticeable in Fe_3O_4-CHBNC and Fe_3O_4-KLBNC. It is well-known and expected that activation broadens the diameter of the smaller pores formed during pyrolysis and increases porosities [123].

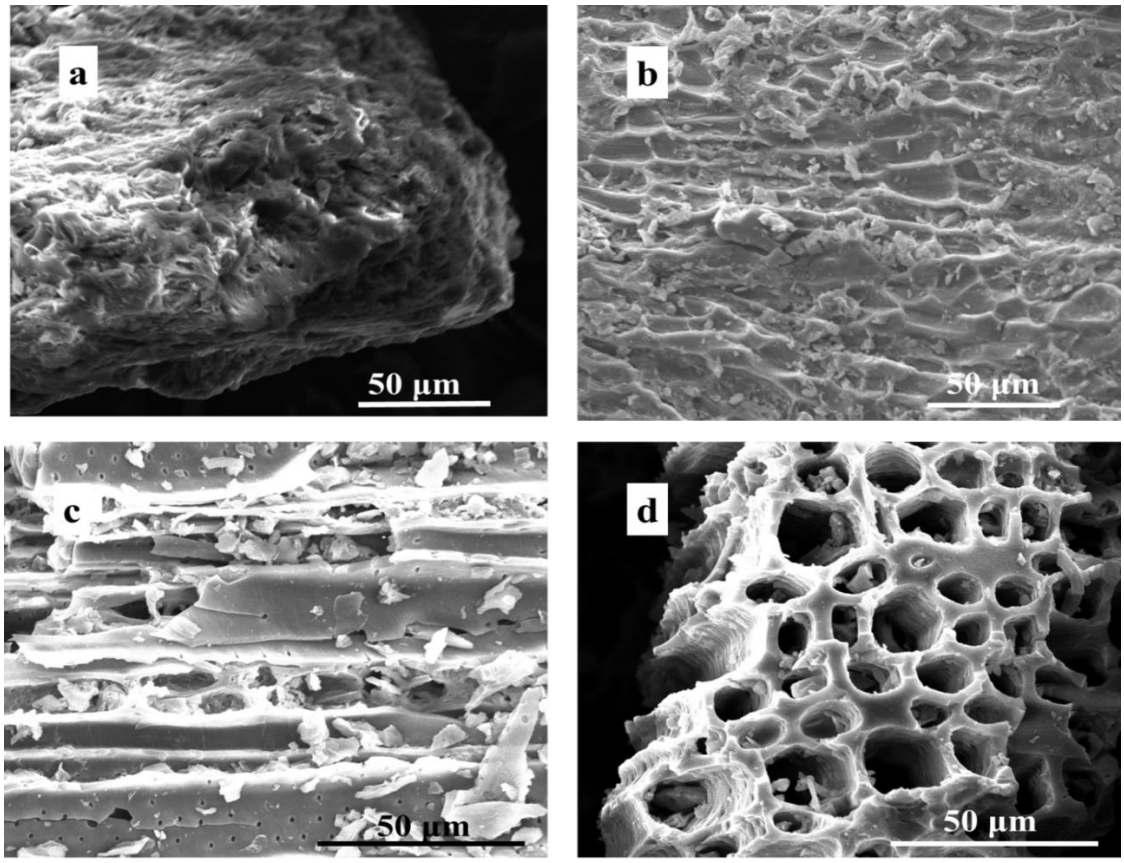

Figure 6.2. SEM images of (a) CHB, (b) Fe_3O_4-CHBNC, (c) KB and (d) Fe_3O_4-KLBNC.

With the help of FTIR spectroscopy, it is possible to examine a compound's chemical structure by observing its rotation and vibration, including that of different surface functional groups like carboxyl, amino, and carbonyl [201]. The FTIR analyses of CHB, Fe_3O_4-CHBNC, Fe_3O_4-CHBNCMB (MB loaded), KLB, Fe_3O_4-KLBNC, and Fe_3O_4-KLBNCMB (MB-loaded) are presented in Figure 6.3a and b. Table 6.1 presents a comprehensive examination of FTIR spectra along with the wavenumber assignments. It is evident from the result that functional groupings such as C-O, C=C, O-H, and C-H have significant intensities [13, 29, 114, 168, 183, 184]. This reveals that the groups are suitable for MB adsorption through electrostatic interaction [185]. Furthermore, the peak at 546 cm^{-1} represents the Fe-O bond, suggesting that Fe_3O_4 is embedded in the activated biochars. The broad peaks of O-H seen in the pristine and Fe_3O_4-biochar nanocomposites are due to the further cause of the OH group from the moisture [52].

Furthermore, the broadening peaks with decreasing intensity at 3425 and 3424 cm^{-1} in the MB-adsorbed Fe_3O_4-CHBNC and Fe_3O_4-KLBNC FTIR spectra shown in Figures 6.3a and b indicate that chemisorption may occur on the surface of biochar, resulting in the formation of new compounds. The two main mechanisms of MB adsorption on biochar are the electrostatic attraction of cationic MB by the large number of OH groups in the solution at higher pH and the creation of hydrogen bonds between the oxygen in MB and the OH group of biochar. Additionally, surface complexation causes oxygen-containing functional groups to form complexes with MB molecules, resulting in MB adsorption on adsorbents. Then, upon adsorption, the peaks at 1620, 1621, 1384, and 1382 cm^{-1} shifted and the peak intensity rose, showing an increase in the number of -C = C bonds induced by the cyclic alkene, most likely as a result of the MB adsorption.

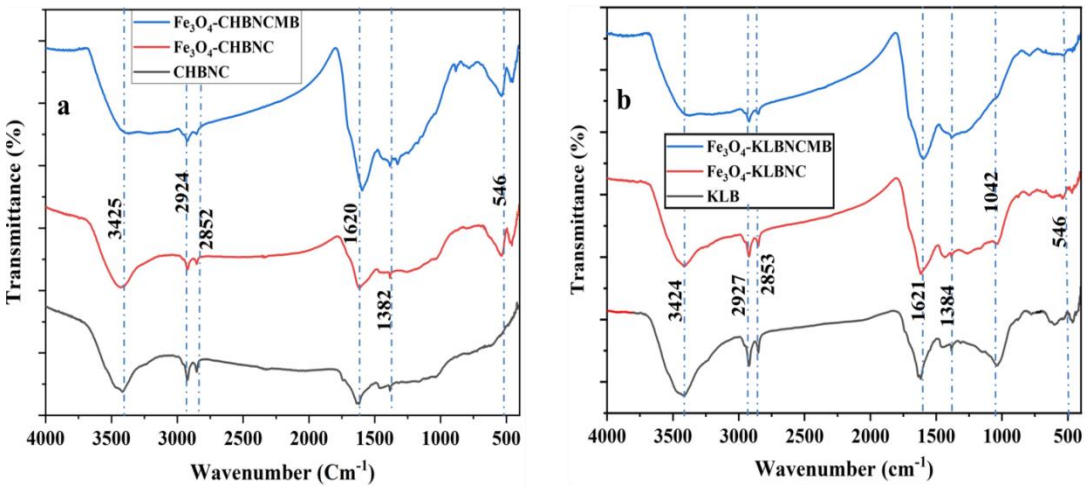

Figure 6.3. FTIR spectra of (a) CHB, Fe_3O_4-CHBNC and Fe_3O_4-CHBNCMB and (b) KLB, Fe_3O_4-KLBNC, Fe_3O_4-KLBNCMB.

Table 6.1. FTIR spectrum and peak assignment of CHB, Fe_3O_4-CHBNC, KB and Fe_3O_4-KLBNC.

CHB	Fe_3O_4-CHBNC	KLB	Fe_3O_4-KLBNC	Assigned functional groups	Ref.
3426	3429	3408	3417	O-H stretching	[13, 29, 168, 174]
2920	2922	2923	2922	Aliphatic C-H stretching	[13, 114, 168, 174]
2853	2851	2849	2854	Aromatic C-H stretching	[29, 168, 174]
1622	1611	1614	1617	C=C bending	[13, 29, 168, 174]
1459	1411	1463	1466	C-O carboxyl stretching	[13, 168]
1384	1308	1382	1383	C-H bending	[114, 168, 174]
1259	1280	1156-1305	1089	O-H and C-O bending	[29, 174]
804	861	841	864	C-H in the aromatic ring	[13, 168]
-	546	-	546	Fe-O bending	[136, 137]

Plots of BET analysis and the adsorption-desorption isotherm for the CHB, Fe_3O_4-CHBNC, KLB, and Fe_3O_4-KLBNC are shown in Figure 6.4. Based on the findings of the BET analysis, Table 6.2 presents an overview of the adsorbents' pore size, surface area, and pore volume. The findings showed that compared to their pristine biochar, Fe_3O_4-CHBNC, and Fe_3O_4-KLBNC had larger specific areas, larger total pore volumes, and smaller pore sizes. Additionally, as per IUPAC, the adsorbents displayed mesoporous structures, as demonstrated by the BET analysis and the adsorption-desorption isotherm [162].

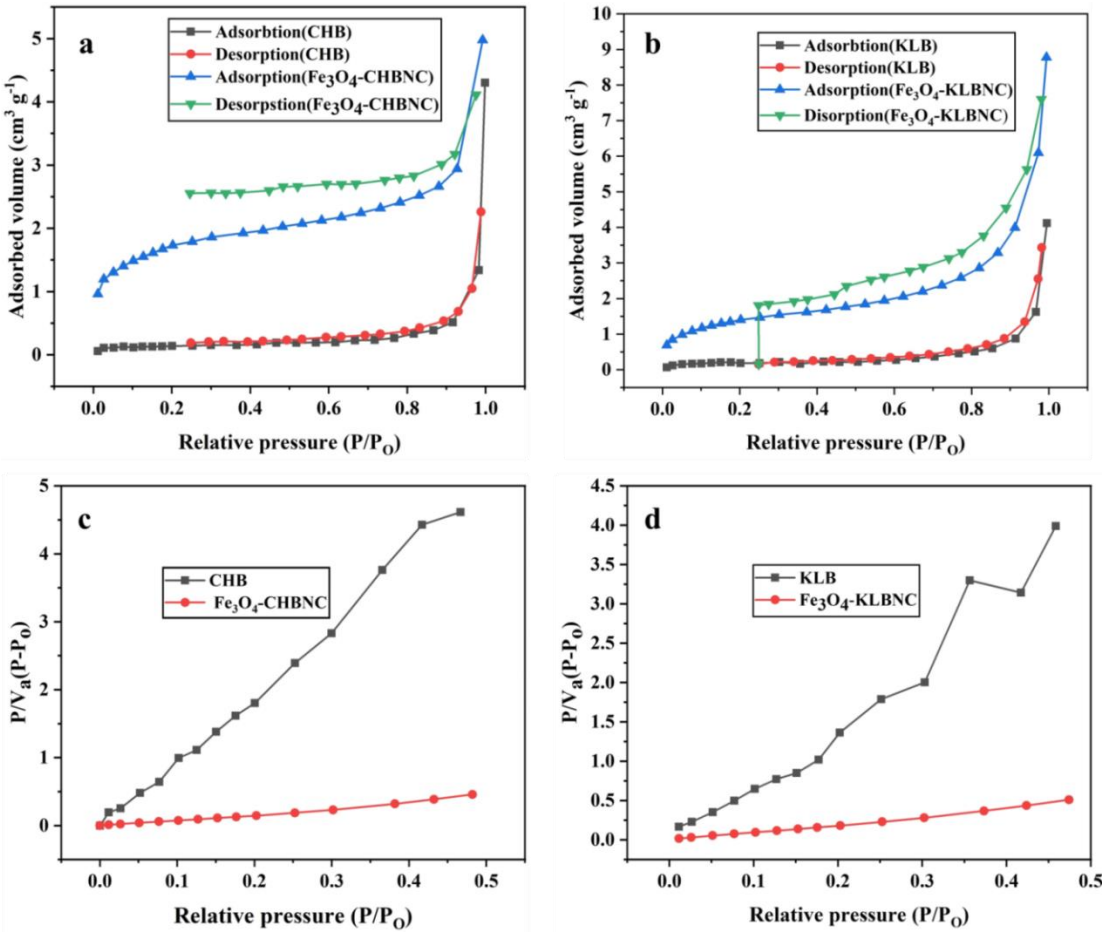

Figure 6.4. Adsorption-desorption isotherm of nitrogen on (a) CHB and Fe_3O_4-CHBNC, (b) KLB and Fe_3O_4-KLBNC, (c) BET analysis plot of CHB and Fe_3O_4-CHBNC, (d) BET analysis plot of KLB and Fe_3O_4-KLBNC.

Table 6.2. BET characteristics of CHB, KLB, Fe_3O_4-CHBNC, and Fe_3O_4-KLBNC.

Adsorbent	Surface area ($m^2\ g^{-1}$)	Pore volume ($cm^3\ g^{-1}$)	Pore size (nm)
CHB	0.519	0.004	32.804
Fe_3O_4-CHBNC	6.17	0.007	4.921
KLB	0.826	0.005	27.626
Fe_3O_4-KLBNC	4.197	0.013	10.423

6.3.2. pH of point of zero charge

An adsorbent's pH_{PZC} is determined by the electrical and chemical properties of its functional groups on the surface. The pH_{PZC} determination results are displayed in Figure 6.5. The values were approximated at pH 7.20 for Fe_3O_4-CHBNC, and 7.42 for Fe_3O_4-KLBNC. To guarantee that the negatively charged surfaces promote adsorption through electrostatic attraction between the adsorbents and the cation (MB), pH values should be kept above these values.

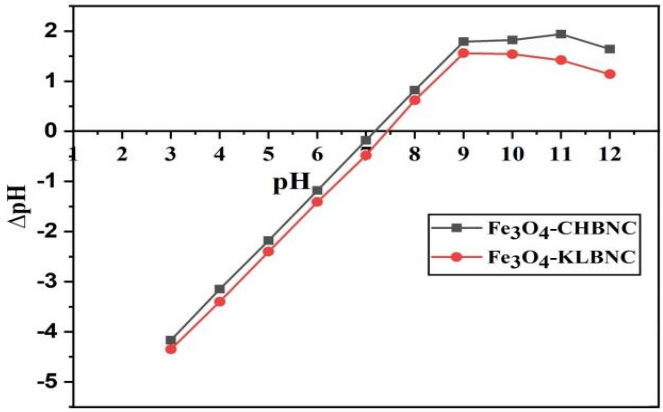

Figure 6.5. The pH_{PZC} of Fe_3O_4-CHBNC and Fe_3O_4-KLBNC.

6.3.3. Batch adsorption studies

The batch adsorption tests on pristine and Fe_3O_4 nanocomposites of CH and KL showed that Fe_3O_4-CHBNC and Fe_3O_4-KLBNC have better efficiency in removing MB from aqueous solutions than the pristine biochars. Then the parameters that can affect the capacity of Fe_3O_4-CHBNC and Fe_3O_4-KLBNC to adsorb MB have been investigated as follows:

6.3.3.1. The effect of contact time

One of the variables influencing adsorption capacity is contact time [185]. The effect of time was investigated from 5 to 240 min. In this investigation, the dose was 0.1 g per 20 mL, the pH was 7.5, and the concentration was 20 mg L^{-1}. As observed in Figure 6.6, early measurements revealed that MB adsorption on the samples was quick. Then the rate slowed down after 20 min and remained constant later than 100 min for both Fe_3O_4-CHBNC and Fe_3O_4-KLBNC. The results show that, at the start, adsorption occurs fast

due to the accessibility of an adequate adsorption surface, and then the rate of adsorption decreases as time increases until an equilibrium point is attained. Because of repulsive forces between solute molecules adsorbed on the solid and in the bulk phase, the remaining adsorption sites are unable to support continuous adsorption [163]. This result also coincides with Kumar and coworkers' reported study on the efficient removal of MB dye by alkaline-treated banana stem biochar through adsorption, which revealed that the adsorption capacity and removal efficiency increase with an increase in contact time [206]. Finally, the result showed that the optimum contact time was 100 min.

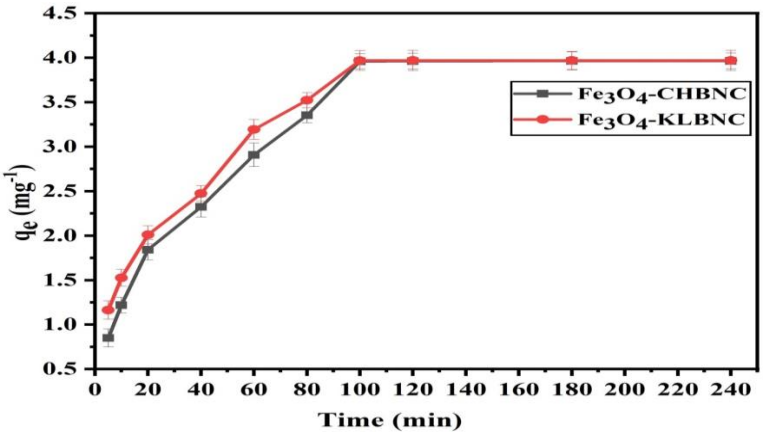

Figure 6.6. The effect of contact time on the adsorption capacity of Fe_3O_4-CHBNC and Fe_3O_4-KLBNC to remove MB.

6.3.3.2. The effect of adsorbent dose

Figure 6.7a and b shows that at various doses of each Fe_3O_4-CHBNC and Fe_3O_4-KLBNC, there were variations in the removal efficiency of MB. The impact of adsorbent dosage was evaluated using 0.10, 0.15, 0.20, 0.25, 0.30, 0.35, 0.40 and 0.45 g per 20 mL for both Fe_3O_4-CHBNC and Fe_3O_4-KLBNC, and the other parameters were set constant (pH 7.5, concentration of 20 mg L^{-1}, and duration of contact: 100 min). It is clear that when the dosages of Fe_3O_4-CHBNC and Fe_3O_4-KLBNC were increased from 0.1 g to 0.2 g, the removal efficiency of MB increased as well. When the doses were between 0.2 and 0.3 g, the removal efficiency of MB became constant. The improvements were attributed to the increased number of accessible adsorption sites. This result agreed with the study reported by Le and coworker [186]. Although the efficiency of the adsorbents to remove MB slightly decreased to 98.69% when the Fe_3O_4-CHBNC dose was greater than 0.3 g, this may be due to the aggregation of adsorbents, which hinders accessible binding sites

and the change in viscosity of the solution, which prevents the free movement of MB molecules. Also, the similar phenomenon reported by Fakhri agrees with this result [187].

As shown in Figure 6.7a and b, the adsorption capacity was adversely affected by the adsorbent dose. With the Fe_3O_4-CHBNC and Fe_3O_4-KLBNC doses increasing from 0.1 to 0.5 g L^{-1}, the value of q_e dropped off quickly. Because the active sites of adsorption can quickly bind with adsorbate and lines to saturation when the amount of adsorbent is low, the slope of the adsorption capacity curve subsequently decreases. When the quantity of adsorbent goes above a certain value, an increasing number of adsorption sites fail to come into contact with adsorbate molecules [188]. In addition, as the amounts of adsorbents increase, the aggregation of adsorbents becomes easier, which decreases the sorbents' surface area [189]. It is important to note that simply increasing the amount of adsorbent used may not always lead to better results. This is because not all parts of the adsorbent are equally effective or accessible. As the adsorption process takes place, the most easily accessible sites get filled up first. Additional adsorbent added may have fewer accessible sites left, which can result in a decrease in the efficiency of the adsorption process. Therefore, it is crucial to carefully consider the amount of adsorbent required for optimal results. Figure 6.7 showed the optimum dose was 0.1 g per 20 mL for both adsorbents and used for subsequent studies.

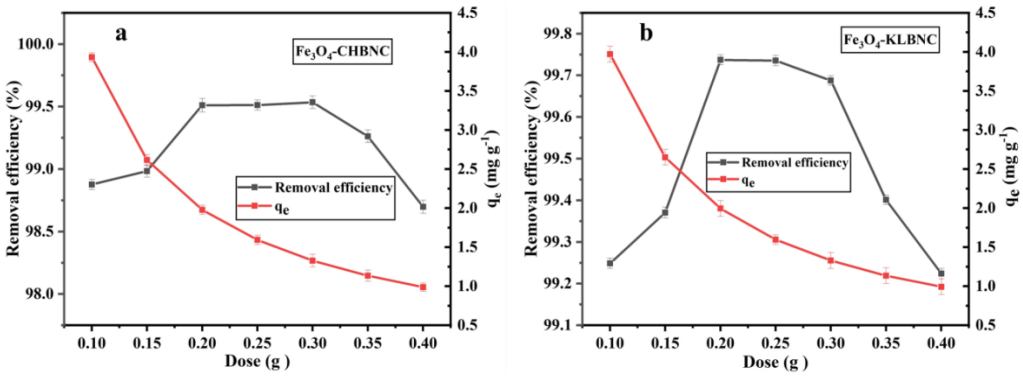

Figure 6.7. The effect of adsorbent dose on the removal efficiency, and the adsorption capacity of (a) Fe_3O_4-CHBNC and (b) Fe_3O_4-KLBNC to remove MB from water.

6.3.3.3. Effect of initial concentration

The influence of the change in concentration of MB was studied from 10 to 80 mg L^{-1} (Figure 6.8a). The other factors were constant (pH was 7.5, the adsorbent dose was 0.10 g

per 20 mL for both Fe_3O_4-CHBNC and Fe_3O_4-KLBNC and contact time was 100 min). It was observed that the adsorption capacity increased as an initial concentration of MB increased from 10 - 100 mg L^{-1}. The adsorption capacity of Fe_3O_4-CHBNC increased from 1.98 - 16.31 mg g^{-1}, while that of Fe_3O_4-KLBNC rose from 1.98 to 14.53 mg g^{-1}.

In general, the adsorption of molecules seems to happen more easily at higher concentrations because a larger driving force is needed for mass transfer. Furthermore, solutions with high initial concentrations need a longer equilibrium time. This is because the adsorbent surface becomes saturated during the last stage of adsorption, causing the majority of the sorbate molecules to diffuse into the porous structure of the adsorbent. This investigation is in agreement with the finding reported by Hamid and coworkers on the removal of MB by mangosteen peel biochar prepared via hydrothermal carbonization [190].

During the optimal adsorption settings, Fe_3O_4-CHBNC and Fe_3O_4-KLBNC removed about 99.10% and 99.27% respectively. Finally, the result showed that at the higher concentrations, the removal efficiencies decreased significantly. The greater mobility of dye molecules in the diluted solutions might be the cause of the higher removal efficiency at the lower MB concentrations. Conversely, a lack of active sites for binding MB molecules may be the reason for the decrease in adsorption efficiency when the initial concentration is increased and the adsorbent dose is constant.

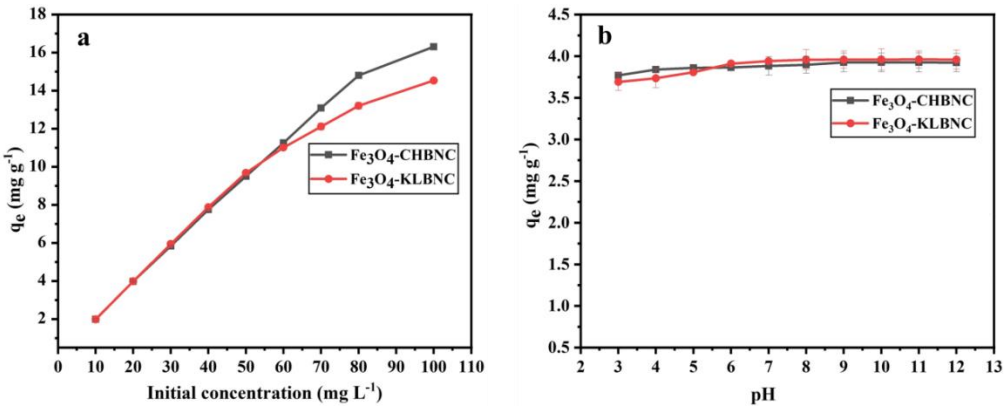

Figure 6.8. The effect of the initial concentration and pH on the adsorption capacity of Fe_3O_4-CHBNC and Fe_3O_4-KLBNC to remove MB from water.

6.3.3.4. Effect of pH

Changes in pH affect the adsorption processes. This occurs as a result of the functional groups of the organic molecules of the dye and the adsorbent dissociating, which changes charges on the surface of the absorbent [191]. Also, the competition between adsorbent cationic dyes and excess OH^- or H^+ ions is dictated by pH, which causes a variation in the MB adsorption capacity.

In this study, the influence of pH was evaluated from 3 to 12 by adjusting to the required pH value by 0.10 M solutions of HNO_3 and NaOH solutions. The impact of solution pH variations on the MB adsorption capacity of Fe_3O_4-CHBNC and Fe_3O_4-KLBNC is explained in Figure 6.8b. The concentration of MB in the experiment was 20 mg L^{-1}, adsorbent doses were 0.1 g per 20 mL, and contact time was 100 min. The results revealed that the adsorption capacity of Fe_3O_4-CHBNC increased (3.76–3.88 mg g^{-1}) in the pH ranges 2–8, and that of Fe_3O_4-KLBNC increased (3.69–3.94 mg g^{-1}) in the range 3–7. This is because the MB dye molecules, which are cationic, generate electrostatic repulsion on the surface of biochar with a high concentration of H^+ ions in an acidic environment. In addition, according to the study reported by Islam and coworkers [192], the presence of OH groups on the adsorbent surface triggers the protonation of the OH group and creates a competition between H^+ ions and dye molecules to bind with the active sites, leading to low uptake of sorbate molecules.

Generally, for both adsorbents, the differences between the lowest adsorption capacities at pH 3 and the maximum adsorption capacities at pH 12 are insignificant, and the minimum removal efficiencies of Fe_3O_4-CHBNC and Fe_3O_4-KLBNC are 92.22% and 94.27%, respectively, at pH 3. This means the adsorbents form the buffer system, which can resist pH changes. Therefore, Fe_3O_4-CHBNC and Fe_3O_4-KLBNC can be used to remove MB in both acidic and alkaline media.

6.3.3.5. The effect of temperature and thermodynamic

The effect of temperature on the MB adsorption efficiency Fe_3O_4-CHBNC and Fe_3O_4-KLBNC was examined using three different temperatures 25 ℃, 35 ℃ and 45 ℃. The removal efficiency of both adsorbents decreases with an increase in temperature shows the adsorption process is exothermic which was also confirmed by the negative ΔH from

the thermodynamic analysis. Table 6.3 represents the thermodynamic parameters such as ΔH, ΔG and ΔS were analyzed using the plot 1/T on x-axis versus ln(K_L) on y-axis results in slope and intercept equal to ΔS/R and –ΔH/R respectively [30]. Where T is temperature in Kelvin, K_L is a ratio (q_e/c_e) of the concentration of MB in solid and liquid phase, R is universal gas constant, ΔG is change in free energy, ΔH, change in enthalpy and ΔS is the change in entropy. The negative value of ΔG reveals that the adsorption processes is spontaneous.

Table 6.3. Thermodynamic behavior of adsorption of MB on Fe_3O_4-CHBNC and Fe_3O_4-KLBNC.

	Temp. (K)	**K_L**	**ΔG (KJ mol^{-1})**	**ΔH (KJ mol^{-1})**	**ΔS (KJ K^{-1} mol^{-1})**	**R^2**
	298	7.802	-5.090			
Fe_3O_4-CHBNC	303	7.127	-4.947	-40.682	-1.188	0.971
	318	2.918	-2.832			
	298	3.997	-3.432			
Fe_3O_4-KLBNC	303	2.107	-1.908	-41.738	-1.288	0.989
	318	1.388	-0.867			

6.3.3.6. Adsorption isotherm and kinetics model

The adsorbate concentration and adsorption capacity at a particular temperature and adsorbent dose are related by adsorption isotherms [7]. The adsorption mechanisms, which rely on variables like surface polarity, surface area, and porosity, are also better understood through analysis of these isotherms. The equilibrium adsorption data were quantified using linear forms of the Freundlich and Langmuir isotherm models [193]. The Langmuir isotherm characterizes monolayer adsorption on a homogeneous surface with uniform active sites (Equation 4.3, see section 4.3.4.6). By fitting the experimental data to the linear equations of the Freundlich (Equation 4.4, see section 4.3.4.6), Langmuir and Temkin (Equation 6.1) isotherm models, the adsorption equilibrium was investigated [6].

Temkin isotherm model: $q_e = \frac{RT}{b} \ln A_T + \frac{RT}{b} \ln C_e$ (6.1)

Where C_e (mg L^{-1}) is the concentration of adsorbate in the solution at equilibrium, q_e (mg g^{-1}) is the amount of MB adsorbed per gram of adsorbent, b is Temkin isotherm constant related to heat of adsorption (J mol^{-1}), A_T (L g^{-1}) affinity of the sorbent for adsorbent [88, 206]. The number of ions adsorbed onto the beads is represented by the value K_F, which is also known as the adsorption or distribution coefficient. Surface heterogeneity is represented by the value of 1/n, which becomes increasingly heterogeneous as it approaches zero [194]. One important property of the Langmuir isotherm is its ability to predict the affinity between the sorbent and adsorbate using a dimensionless quantity known as the separation factor (R_L), which has calculated using Equation 4.5 as indicated in section 4.3.4.6 [194]. The Langmuir and Freundlich isotherm parameters are investigated using the concentrations of 20–500 mg L^{-1} as presented in Figure 6.8a–d.

Table 6.4 provides an overview of the Langmuir, Freundlich and Temkin isotherm parameters along with the corresponding correlation coefficients (Figures 6.9a–d and Figure 6.9a-b). Higher correlation coefficients (R^2), which show monolayer adsorption on a particular site of a homogeneous surface of the adsorbent, indicate greater applicability of the Langmuir model (R^2 = 0.999 for Fe_3O_4-CHBNC and Fe_3O_4-KLBNC) [9]. The Langmuir isotherm predicts that there will be no interaction between the adsorbed molecules and that adsorption energy will be uniform on the adsorbent surface [13]. Fe_3O_4-CHBNC and Fe_3O_4-KLBNC have low separation factor values (R_L = 0.059 and R_L = 0.123, respectively), suggesting the successful physical adsorption process. For heterogeneous surfaces or surface-supporting sites with varying affinities, the Freundlich isotherm illustrates multilayered adsorption [184]. Favorable sorption is indicated by a computed value of n that falls between 1 and 10. Additionally, Table 6.4 indicates that the regression coefficient R^2 is higher for the Langmuir isotherm model than for the Freundlich model, suggesting that the Langmuir model provides a more accurate description. These findings imply that MB is adsorbed in monolayers on the surfaces of Fe_3O_4-CHBNC and Fe_3O_4-KLBNC.

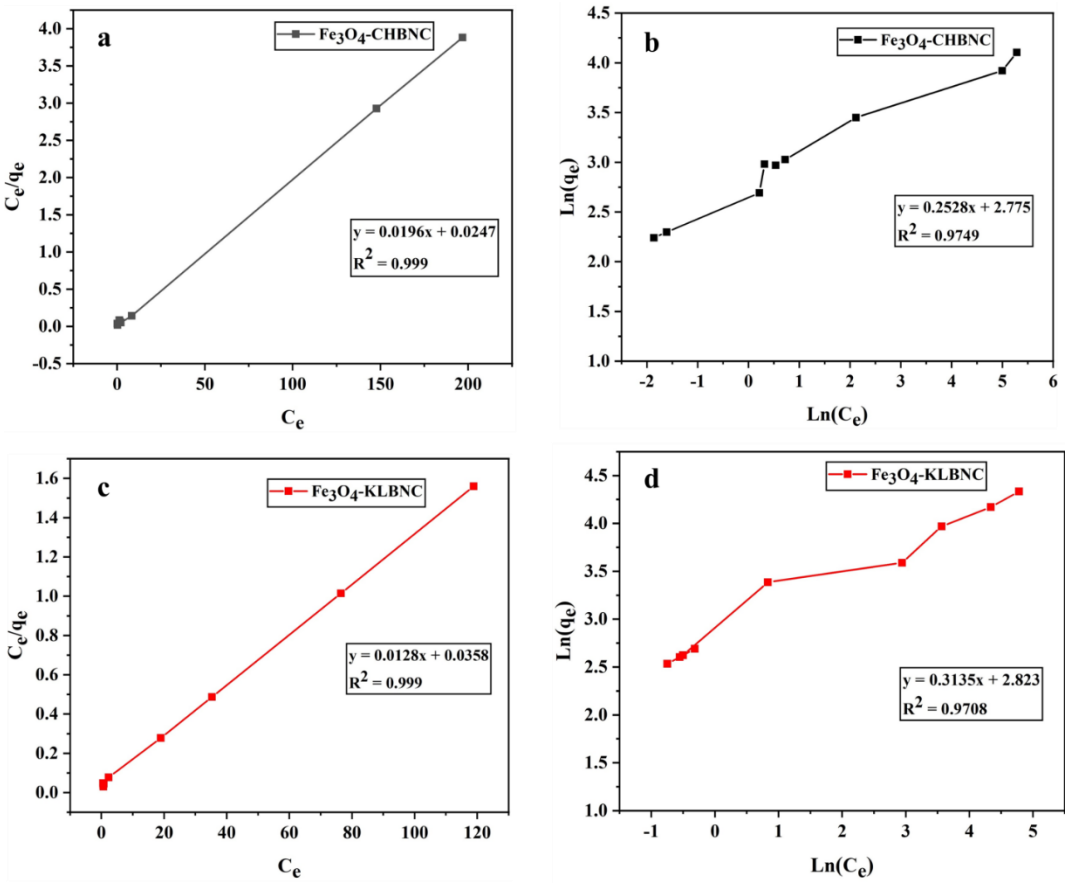

Figure 6.9. (a) Langmuir isotherm for Fe_3O_4-CHBNC, (b) Freundlich isotherm Fe_3O_4-CHBNC, (c) Langmuir isotherm for Fe_3O_4-KLBNC, and (d) Freundlich isotherm Fe_3O_4-KLBNC.

The Temkin isotherm model assumes an interaction between the adsorbent and adsorbate [207]. According to this model, the heat of adsorption of all molecules in a certain layer decreases linearly with surface coverage. The Temkin model agreements were found to be R^2 = 0.929 for Fe_3O_4-CHBNC and R^2 = 0.977 for Fe_3O_4-KLBNC, with b values of 0.910 KJ mol^{-1} and 1.177 KJ mol^{-1}, respectively. These values are lower than 8.0 KJ mol^{-1}, which is associated with the dominant physisorption of the dye on the adsorbents [91]. Moreover, the positive values of b indicate that the adsorption process is exothermic, and the result is in agreement with the thermodynamic analysis.

Table 6.4. Langmuir, Freundlich and Temkin isotherm constants for adsorption of MB.

Isotherm model	Fe_3O_4-CHBNC	Fe_3O_4-KLBCN
Langmuir	y = 0.0196x + 0.0247	y = 0.0128x + 0.0358
q_m	51.020	78.125
K_L	0.794	0.358
R_L	0.059	0.123
R^2	0.999	0.999
Freundlich	y = 0.2528x + 2.775	y = 0.3135x + 2.823
n	2.293	2.743
K_F	16.542	13.701
R^2	0.9749	0.9708
Temkin	y = 2.5645x + 8.3922	y = 1.9634x + 8.1098
A_T	27.521	62.136
b_T	909.957	1176.829
R^2	0.929	0.977

The kinetic studies were carried out using 20.0 mL of MB solution with initial concentration of 20 mg L^{-1}, pH 7.5, 0.1 g of Fe_3O_4-CHBNC and Fe_3O_4-KLBNC, which had shaken for 5, 10, 20, 30, 40, 60, 80, 120, 180 and 240 min at 200 rpm (25 ºC) following the procedures described by Hamid and coworkers [190]. After shaking, the solutions were centrifuged, and the concentrations of MB in the supernatant were determined. The amount of MB adsorbed onto Fe_3O_4-CHBNC and Fe_3O_4-KLBNC at time t (q_t) was calculated using Equation 4.6 which is indicated in section 4.3.4.6.

The adsorption kinetics models employed Equations 4.7 for the pseudo-first-order and pseudo-second-order adsorption kinetics was evaluated using Equation 4.8 as described in section 4.3.4.6. Finally, intraparticle diffusion was evaluated using Equation 6.2.

$$q_t = K_{di} t^{1/2} + c \qquad (6.2)$$

Where, q_t represent the amounts of MB adsorbed (mg g^{-1}) at time t (min), K_{di} (mg g^{-1} $min^{1/2}$) and C are the intraparticle diffusion rate constant and intercept, respectively. Table 6.5 lists the adsorption parameters, which were computed for pseudo-first-order kinetic, pseudo-second-order kinetic and intraparticle diffusion models including R^2 and

other constants. The pseudo-second-order model was determined to be a more appropriate representation of the adsorption kinetics in this work. In general, the pseudo-first-order model: mainly assumes that the diffusion step dominates the adsorption process. The pseudo-second-order model assumes that the chemisorption mechanism controls the adsorption rate. Two mechanisms usually occur in the adsorption process, and the slightly higher R^2 of pseudo-second-order model indicates the decisive phase could be chemical sorption [178]. Figure 6.8c and d shows that initial adsorption rate was rapid during the first contact time durations around 20 min. the presence of free active sites on the surface of the adsorbent may be the cause of greater rate of initial adsorption. However, after 20 min the adsorption rate stayed constantly attributing to the adsorbent surface becoming saturated with the dye and achieving the equilibrium.

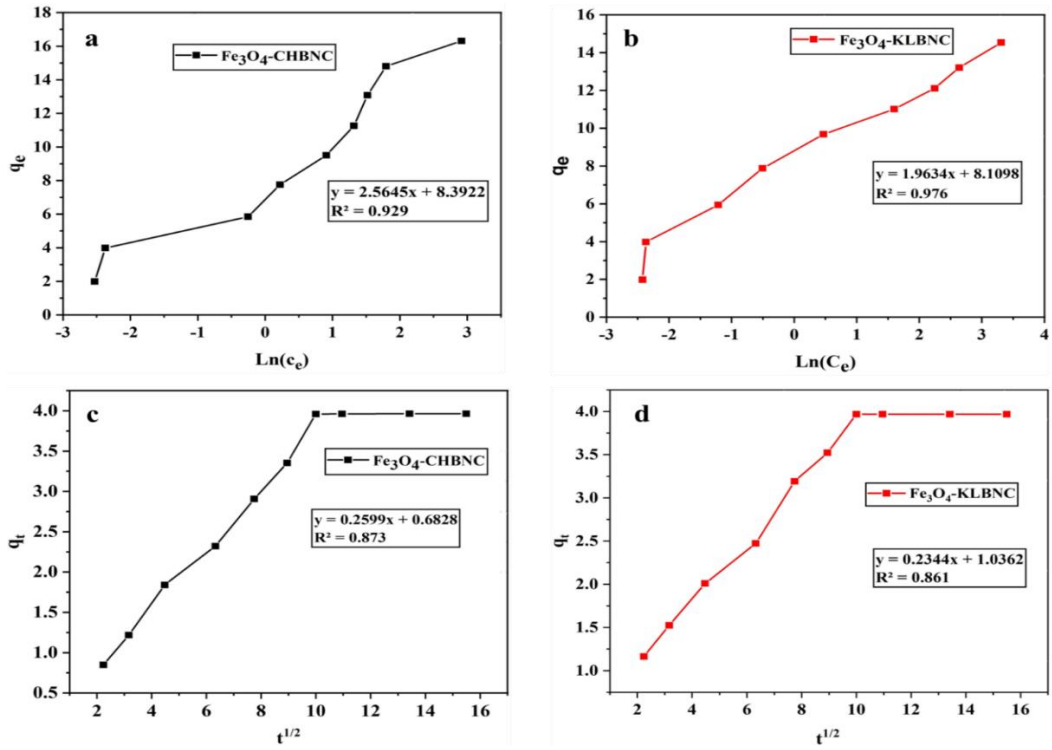

Figure 6.10. (a) Temkin isotherm for Fe_3O_4-CHBNC, (b) Temkin isotherm for Fe_3O_4-KLBNC, (c) Intraparticle diffusion model for Fe_3O_4-CHBNC and (d) intraparticle diffusion model Fe_3O_4-KLBNC.

The intraparticle diffusion model determines the diffusion mechanism and rate limiting step in the adsorption. The estimated intraparticle diffusion model curves (Fig. 6.10c and d), comprises of three linear parts and do not transverse origin showing the adsorption is a multi-process [208]. The k_{diff} values for both Fe_3O_4-CHBNC (0.234) and Fe_3O_4-KLBNC

(0.260) are suggesting comparable rate of inter-particle diffusion. Overall, the data suggests that inter-particle diffusion plays a significant role in the adsorption of MB onto the adsorbents. The presence of two linear regions indicates a multi-step adsorption process with both surface adsorption and intraparticle diffusion mechanisms. Furthermore, the analysis of Boyd model was applied using a linear plot of ln $(1 - q_t/q_e)$ versus t for the adsorption of MB onto Fe_3O_4-CHBNC and Fe_3O_4-KLBNC. If the plot passes through the origin and exhibits linearity, then the rate determining step in the adsorption process is controlled by intraparticle diffusion [178]. However, the lines of the equations $y = -0.0635x + 0.9821$ with $R^2 = 0.9002$ for Fe_3O_4-CHBNC and $y = -0.0784x + 1.2268$ with $R^2 = 0.894$ for Fe_3O_4-KLBNC do not pass through the origin, indicating that the film diffusion mechanism primarily controls the overall adsorption rate.

Table 6.5. Constants of pseudo-first, second-order adsorption kinetic and intraparticle diffusion models.

Kinetic Model	**Fe_3O_4-CHBNC**	**Fe_3O_4-KLBNC**
$q_{experimental}$	3.964	3.968
Pseudo-first order		
q_e	13.51	13.650
K_1	6.90×10^{-2}	7.860×10^{-2}
R^2	0.949	0.894
Pseudo-second order		
q_e	4.523	4.378
K_2	8.259×10^{-2}	1.56×10^{-2}
R^2	0.991	0.994
Intraparticle diffusion		
K_{diff}	0.260	0.234
C	0.683	1.036
R^2	0.874	0.861

6.3.3.7. Comparison of the result with other similar studies

The maximum adsorption capacities and MB removal efficiencies of some adsorbents from previously reported studies are described in Table 6.6. The Fe_3O_4-biochar

nanocomposites made in this work had higher adsorption capacities than some of the adsorbents mentioned in the previous studies. It follows that Fe_3O_4-CHBNC and Fe_3O_4-KLBNC are effective adsorbents for removing MB from an aqueous solution. Additionally, by synthesizing value-added treatment products, biochar-nanocomposites made from biomass such as KL and CH provided an efficient way to get rid of possible pollutants. CH and KL are alternative, cost-free biomass for biochar production, and the method is a suitable approach for resource recovery and environmental protection.

Table 6.6. Comparison of the result with MB removal efficiency of some adsorbents from aqueous solution.

Adsorbent	C_o (mg L^{-1})	Volume (mL)	m (g)	q_m (mg g^{-1})	R (%)	Ref.
Fe_3O_4 nano-powder	20.00	25.00	2.00	25.54	99.69	[8]
Acacia nilotica BC	50.00	50.00	2.00	85.68	ND	[13]
Torified-*Acacia nilotica* BC	50.00	50.00	2.00	158.30	ND	[13]
Wheat straw-biochar	100.00	10.00	0.60	12.03	ND	[47]
Fe_3O_4@C core-shell comp.	20.00	40.00	0.20	42.11	ND	[164]
NaOH-treated coffee husk	37.78	50.00	0.74	200.00	93.52	[183]
NaOH-treated banana stem	25.00	50.00	0.80	0.47	96.59	[185]
Fe_3O_4/SDB nanocomposite	30.00	30.00	0.25	25.33	75.00	[140]
H_3PO_4-treated beli biochar	10.00	50.00	0.30	12.32	90.00	[92]
Fe_3O_4-CHBNC	20.00	20.00	0.10	51.02	99.10	This study
Fe_3O_4-KLBNC	20.00	20.00	0.10	78.13	99.23	

6.3.3.8. Reusability of the Adsorbents

One benefit of the suggested biochar-nanocomposite adsorbents is their reusability and ease of separation from soluble waste. The results of this study are shown in Figure 6.11a, b. According to the study, the relative adsorbent efficiencies of Fe_3O_4-CHBNC and Fe_3O_4-KLBNC after their first use in the sorbent recycling process were 98.86% and 99.16%, respectively. After six series, the values decreased to 77.57% for Fe_3O_4-CHBNC and 83.49% for Fe_3O_4-KLBNC. The result revealed that at the sixth succession, the MB adsorption capacity Fe_3O_4-KLBNC was 83.49%, and based on the low cost, ease of

synthesis, and better regeneration cycles, Fe_3O_4-KLBNC could be a better adsorbent for dye removal.

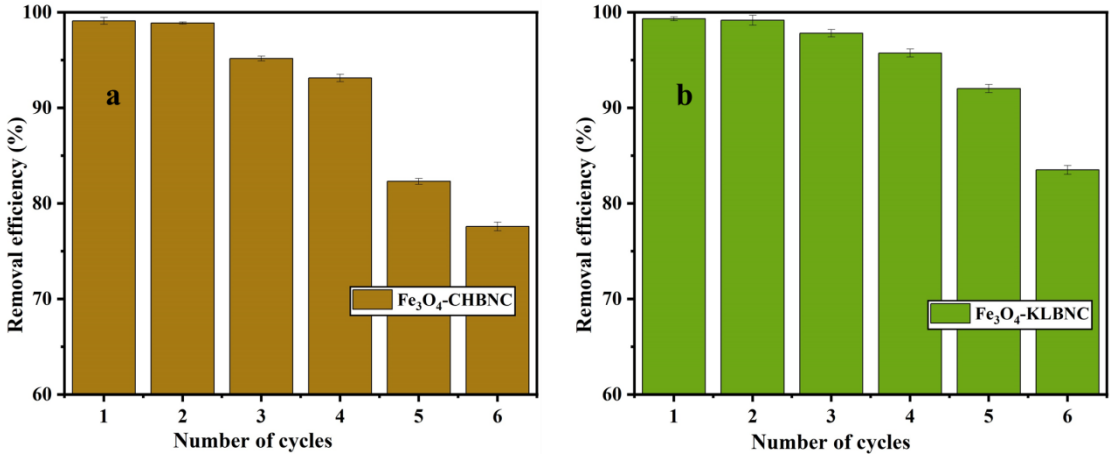

Figure 6.11. Reusability of (a) Fe_3O_4-CHBNC and (b) Fe_3O_4-KLBNC to remove MB from the aqueous solution.

6.4. Summary

Pristine biochar of CH, prepared by carbonization of biomass at 300 °C, removes 44.73%, and KL removes 75.26% MB from 20 mg L^{-1} aqueous solutions. Treating the biomass before pyrolysis with $FeCl_3$ increased MB removal efficiencies of Fe_3O_4-CHBNC and Fe_3O_4-KLBNC. The removal of MB from 20 mg L^{-1} aqueous solutions using 0.1 g of both Fe_3O_4-CHBNC and Fe_3O_4-KLBNC in 120 min has an efficiency of 99.10% and 99.23%, respectively. These materials are prepared by pretreating every 25 g of biomass with 12.5 mmol of FeS and $FeCl_3$ 1:1 molar ratio and carbonized at 300 °C for 1 h. The maximum removal efficiencies can be affected by parameters like the contact time, the adsorbent dose, the initial concentration, and the pH of the solution.

It is confirmed that the monolayer adsorption mechanism of MB onto the adsorbents is more dominant by the excellent fixing of the equilibrium data in the Langmuir isotherm equation. For the Langmuir and Freundlich isotherms in each of the adsorbents, linear plots were created. The value of R_L in the Langmuir isotherm falls between zero and one, signifying favorable adsorption. The MB adsorption had been found to fit a pseudo-second-order model. In addition, the reusability (recycling) study of the sorbents showed that after six cycles, the values decreased to 77.57% for Fe_3O_4-CHBNC and 83.49% for Fe_3O_4-KLBNC. Due to its higher MB adsorption capacity, low cost, ease of preparation,

and number of reusability cycles, Fe_3O_4-KLBNC could be a better adsorbent for dye removal than Fe_3O_4-CHBNC.

The findings of this study supported the effectiveness of the suggested approach for recycling KL and CH as well as for preparing low-cost carbon material. The lab-scale data can be used as a starting point for future research aimed at designing treatment plants that effectively remove MB dye-containing effluents.

CHAPTER SEVEN

7. MAGNETIC BIOCHAR NANOCOMPOSITES OF COFFEE HUSK AND KHAT LEFTOVER FOR REMOVAL OF CHROMIUM (VI) FROM WATER

7.1. Introduction

Chromium is a highly versatile metal with unique properties that make it an essential component in a wide range of industries [209]. It is commonly used in metallurgy, electroplating, and the production of stainless steel, as it enhances the corrosion resistance and durability of the final product. Additionally, chromium compounds find their way into the manufacturing of pigments, dyes, and tanning agents [210]. However, chromium also poses a significant threat to the environment due to its impact on health. The effluents and solid wastes from industries like mining, chrome-plating, leather-tanning, and dye-manufacturing are high in chromium concentration and identified as health hazards due to pollution. Industrial waste often gets used in landfilling, which can cause seepage. This leaching of toxic chromium from soil into water bodies can cause a threat to the environment [211]. The ferrochrome industry is one of the contributors to chromium pollution in water bodies. It is crucial to treat industrial effluents before releasing them by appropriate methods. In Chapter 5, we discussed various techniques that have been used in the past to remove Cr(VI) from water and examined their limitations. We concluded that adsorption is a relatively suitable and advantageous method for removing Cr(VI) from water. The effectiveness of the adsorption process is highly dependent on the type of adsorbent material used [34].

Some reports show that magnetic iron oxide is utilized to enhance the adsorption of Cr(VI) properties of biochar [88, 212–215]. For instance, Fe_3O_4 biochar nanocomposites of sewage sludge and woodchips, Vine shoots, burley tobacco stems, peanut husk and bagasse are investigated with higher efficiency than their pristine biochar. Also, Fe_3O_4 nanocomposite of activated carbon [165, 166] and graphene [167] are employed for Cr(VI) removal. However, to the best of our knowledge there is no reported study about employing Fe_3O_4 coffee husk and khat leftover biochar nanocomposites for Cr(VI) removal.

This study was carried out to evaluate the conversion of khat leftover and coffee husk into valuable goods with dual benefits. These include eliminating hazardous contaminants

Kochito, J.; Gure, A.; Abdisa, N.; Tadesse, T.; Femi, O. E. Magnetic Biochar Nanocomposites of Coffee Husk and Khat (Catha Edulis) Leftover for Removal of Cr(VI) from Wastewater. *Curr. Res. Green Sustain. Chem.*, **2024**, *8*, 100403.

from wastewater and economically discarding biomass wastes. The Fe_3O_4-CHB and Fe_3O_4-KLBNC) were produced, characterized and their Cr(VI) removal efficiencies were evaluated. Both adsorbents' capacities for removing Cr(VI) were examined, along with the effects of adsorbent dose, initial concentration, pH, and contact time. Adsorption isotherms and kinetics were also assessed. Finally, to assess the regeneration or reusability of the adsorbents, desorption studies of Cr(VI) from the Fe_3O_4-CHBNC and Fe_3O_4-KLBNC were carried out.

7.2. Experimental

7.2.1. Batch adsorption studies

To evaluate the Cr(VI) removal efficiencies of CHB, KLB, Fe_3O_4-CHBNC, and Fe_3O_4-KLBNC, preliminary adsorption tests were carried out [176]. The rate and adsorption equilibrium phenomena associated with Cr(VI) adsorptions were assessed through batch experiments. A 1000 L^{-1} Cr(VI) stock solution of Cr (VI) was prepared by dissolving $K_2Cr_2O_7$ in deionized water [138, 175]. For the subsequent investigations, different concentrations of Cr(VI) were prepared from the stock solution. To conduct the isotherm studies, the solution containing the initial Cr(VI) concentration, which varied from 10 to 500 mg L^{-1}, was mixed with 0.10 g of biochar. The kinetics were studied using a 20 mg L^{-1} Cr(VI) solution and were conducted at 25 ± 1 °C. The adsorbent-solution mixtures were shaken at 200 rpm, and then the amount of Cr(VI) left in the solutions was filtered, and it was analyzed using the UV-Vis spectrophotometer at a maximum wave length of 540 nm. As indicated in section 4.3.4.6, Equation 4.1 was utilized to calculate the Cr(VI) removal efficiency (R) for every adsorbent, while Equation 4.2 was employed to ascertain the adsorption capacity (q_e) [173].

7.2.2. Reusability of the adsorbents

At 25±1 ℃, six successive cycles of adsorption-desorption were performed to assess the adsorbents' reusability [136, 174]. A 2 g sample of each Fe_3O_4-CHBNC and Fe_3O_4-KLBNC was added in 250 mL of Cr(VI) solution, and the sample was shaken for 120 min at pH 2 to initiate adsorption for each cycle. After being mixed with 100 mL of 0.1M KOH, the Cr(VI)-loaded adsorbent was shaken for 120 min and filtered to separate it. Following every cycle of adsorption-desorption, the Fe_3O_4-CHBNC and Fe_3O_4-KLBNC

were cleaned using distilled water, dried for 2 h at 70 °C, and then recovered for the subsequent cycle [176].

7.3. Results and Discussion

7.3.1.Adsorbent characterization

The FTIR analyses of Fe_3O_4-CHBNC, KLB, Fe_3O_4-KLBNC, Cr(VI)-loaded Fe_3O_4-CHBNC (Fe_3O_4-KLBNCCr), CHB, and Fe_3O_4-KLBNC are presented in Figure 7.1a and b. Table 6.3, section 6.3.3, shows that functional groups such as C-O, C=C, O-H, and C-H have substantial intensities [13, 29, 114, 168, 183, 184]. This demonstrates that the groups are appropriate for Cr(VI) adsorption via electrostatic interaction [185]. Additionally, the peak at 546 cm^{-1} represents the Fe-O bond, demonstrating that Fe_3O_4 is contained in the activated biochar. The large O-H bands seen in the virgin and Fe_3O_4-biochar nanocomposites are owing to the addition of the OH group from moisture [52]. After Cr(VI) ions were adsorbed on the Fe_3O_4-CHBNC and Fe_3O_4-KLBNC, there was a significant decrease in the peak intensities of the FTIR spectra in the 3408–3429 cm^{-1} range and around 546 cm^{-1}. The observed differences in peak intensity at the specified range could potentially be attributed by the interactions between Cr(VI) ions and functional groups on the adsorbents.

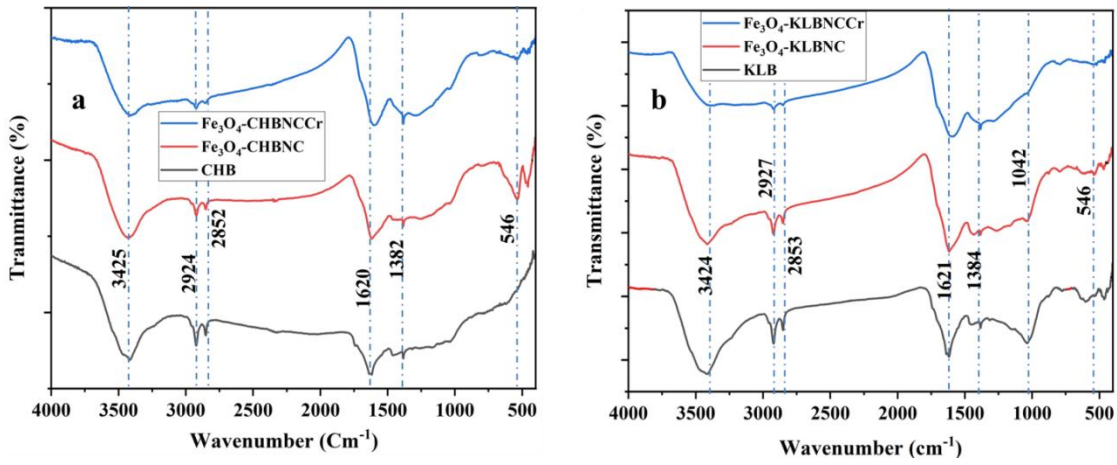

Figure 7.1. FTIR spectra of (a) CHB, Fe_3O_4-CHBNC and Fe_3O_4-CHBNCCr (b) KLB, Fe_3O_4-KLBNC and Fe_3O_4-KLBNCCr.

7.3.2. Batch adsorption studies

The parameters that can affect the Cr(VI) adsorption efficiency of Fe_3O_4-CHBNC and Fe_3O_4-KLBNC were investigated at constant temperature (25±1 ℃) as follows*;*

7.3.2.1. Effect of contact time

Contact time is one of the factors affecting adsorption capacity. Studies indicate that as contact time increases, so does the adsorption capacity [168]. Figure 7.2 illustrates that the initial stages of Cr(VI) adsorption on the samples were found to be rapid. After 80 min, it started to gradually increase, and after 100 min, it started to stay relatively constant for both Fe_3O_4-CHBNC and Fe_3O_4-KLBNC. According to the results, adsorption starts out quickly because there is a large enough adsorption sites available, but it gradually slows down until equilibrium is reached. Because of repulsive forces between solute molecules adsorbed on the solid and the bulk phase, the remaining adsorption sites are unable to support continuous adsorption [163].

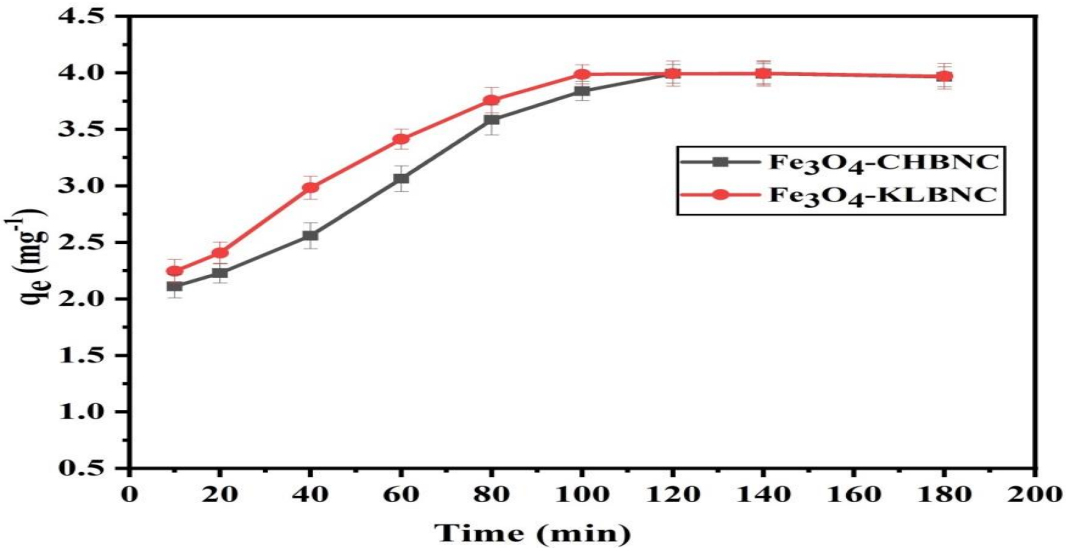

Figure 7.2. The effect of contact time on the adsorption capacity of Fe_3O_4-CHBNC and Fe_3O_4-KLBNC to remove Cr(VI) from water.

7.3.2.2. The effect of adsorbent dose

The adsorbent doses of 0.05, 0.1, 0.15, 0.2, 0.25, 0.3, and 0.35 g per 20 mL were tested to determine the effect of adsorbent dose [204]. Figure 7.3a and b show that at the various dosages of Fe_3O_4-CHBNC and Fe_3O_4-KLBNC, there are significant variations in the

efficiency of Cr(VI) removal and the capacities of adsorption. As the dosage of Fe_3O_4-CHBNC and Fe_3O_4-KLBNC was raised from 0.05 g to 0.10 g, the efficiency of Cr(VI) removal showed a significant increase and remained slightly constant above 0.10 g and above. There are more binding sites available for Cr(VI) adsorption at higher adsorbent doses, which causes the removal efficiency to rise until the dosage reaches saturation. Therefore, for both Fe_3O_4-KLBNC and Fe_3O_4-CHBNC, 0.10 g per 20 mL has been chosen for the subsequent studies.

The adsorbent dose negatively influenced the adsorption capacity (Figure 7.3a and b). The value of q_e decreased rapidly when the Fe_3O_4-CHBNC and Fe_3O_4-KLBNC doses changed from 0.05 to 0.35 g L^{-1}. Because the active adsorption sites can be quickly covered by adsorbates and approach maximum capacity when the amount of adsorbent is low, the slope of the adsorption capacity curve subsequently decreases. When the amount of adsorbent rises to a certain value, more and more sites of adsorption are unable to make contact with some particles of adsorbate [188]. Furthermore, the specific surface area of the adsorbents decreases as their amounts rise because it becomes easier for them to aggregate [187].

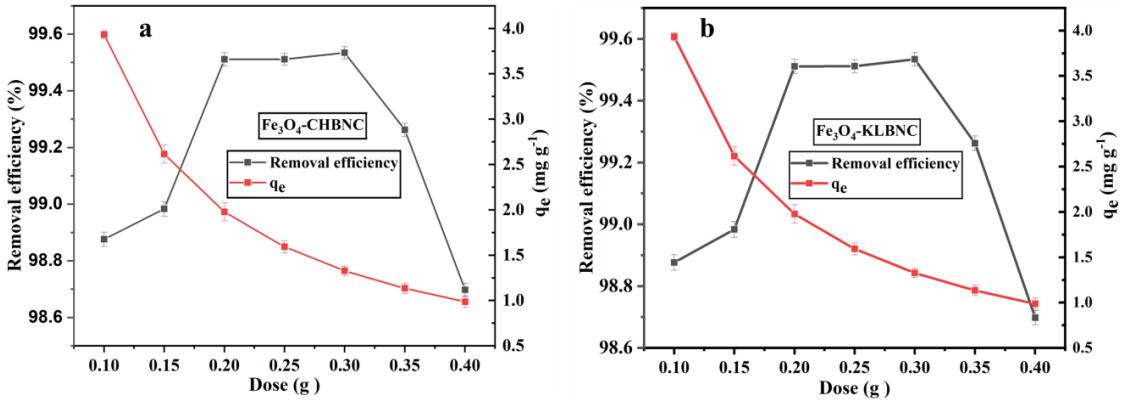

Figure 7.3. The effect of adsorbent dose on the removal efficiency, and the adsorption capacity of (a) Fe_3O_4-CHBNC and (b) Fe_3O_4-KLBNC to remove Cr(VI) from water.

7.3.2.3. The effect of initial concentration

The effect of initial concentration and isotherm model was studied using the initial concentrations 10-100 mg L^{-1}. The other parameters were kept constant (pH 2, adsorbent dose 0.1 g, and contact time 120 min). Figure 7.4a describes how the adsorption efficiency depends on the initial Cr(VI) concentration. The result showed that the Cr(VI)

adsorption capacity of the adsorbents increased with increasing the initial concentration of Cr(VI). In the initial concentration ranges between 10 and 100 mg L^{-1}, the adsorption capacity of Fe_3O_4-CHBNC changed from 3.98-16.90 mg g^{-1}, while that of Fe_3O_4-CHBNC changed from 3.99-18.34 mg g^{-1}. Generally, the adsorption of ions appears to happen more easily at higher initial concentrations because a higher driving force is needed for the mass transfer of Cr(VI). It also shows that solutions with high initial concentrations need a longer equilibrium time. This is because, as the adsorbent surface becomes saturated during the last stage of adsorption, the majority of the sorbate ions diffuse into the porous structure of the adsorbent.

Conversely, an increase in Cr(VI) concentration results in a decrease in removal efficiency. At the optimum adsorption conditions, Fe_3O_4-CHBNC and Fe_3O_4-KLBNC removed about 99.83% and 99.86% respectively. At the Cr(VI) concentration higher than 20 mg L^{-1}, the removal efficiency had significantly reduced for both Fe_3O_4-CHBNC and Fe_3O_4-KLBNC. However, Fe_3O_4-KLBNC has higher Cr(VI) removal efficiency than CHBNC at higher initial concentrations. One possible explanation for the increased removal efficiency at lower Cr(VI) concentrations could be the increased ion mobility in the diluted solutions. In the meantime, a lack of active sites for binding Cr(VI) may be the cause of the decrease in efficiency of adsorption when the initial concentration rises while maintaining a constant adsorbent mass.

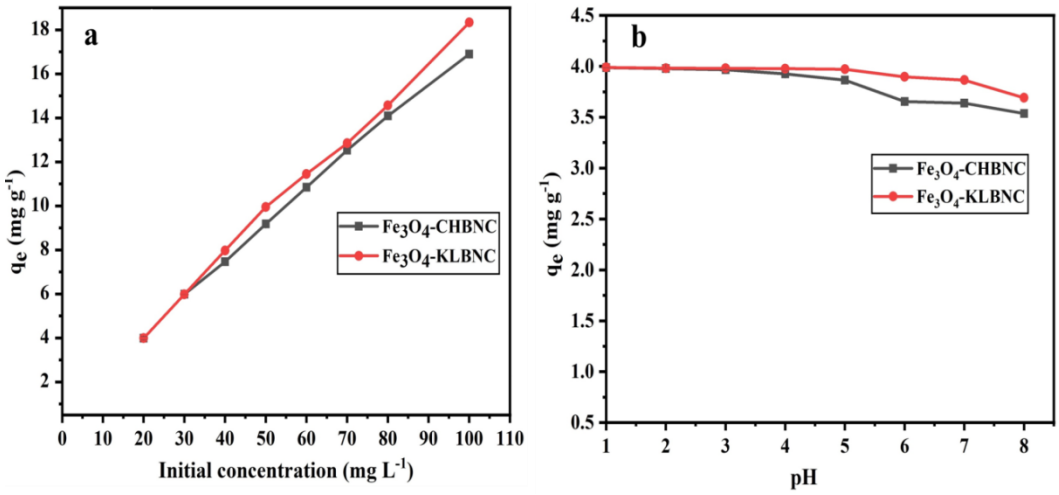

Figure 7.4. The effect of (a) concentration and (b) pH on the Cr(VI) adsorption capacity of Fe_3O_4-CHBNC and Fe_3O_4-KLBNC.

7.3.2.4. The effect of pH

In general, pH of the solution affects the adsorption processes, results from the functional groups on the adsorbent and changes in the surface charge of the absorbent [184]. The pH range of 1–8 was used to assess the impact of pH changes on the capacity of adsorption. The pH of the solutions was adjusted using 0.10 M solutions of HNO_3 and NaOH solutions [14]. The influence of pH change on the capacity of Fe_3O_4-CHBNC and Fe_3O_4-KLBNC for Cr(VI) adsorption is presented in Figure **7.4**b. The concentration of adsorbate for the study was 20 mg L^{-1}, the adsorbent dose was 0.1 g per 20 mL for both Fe_3O_4-CHBNC and Fe_3O_4-KLBNC, the temperature was 25±1 ℃, and the time for adsorption was 120 min. The results indicated that the capacity of adsorption is dependent on pH changes, and the highest values observed at the pH of the Cr(VI) solutions were 2. However, when the pH values were greater than 5, the adsorption capacity decreased significantly. The competition between the Cr(VI) ion and the extra OH^-/H^+ ions in the solution towards the adsorbent is determined by the pH in the system, which causes a variation in Cr(VI) adsorption capacity.

7.3.2.5. Effect of temperature and thermodynamics studies

The purpose of the study was to investigate how temperature affects the efficiency of Cr(VI) adsorption using two different adsorbents, Fe_3O_4-CHBNC and Fe_3O_4-KLBNC, at three different temperatures: 25°C, 35°C, and 45°C. The results revealed that as the temperature increased, the efficiency of both adsorbents decreased, indicating that the adsorption process is exothermic. The negative ΔH value supports the conclusion obtained from the thermodynamic analysis. Table 7.1 displays the thermodynamic parameters, such as ΔH, ΔG, and ΔS, which were analyzed using a plot of 1/T on the x-axis versus $\ln(K_L)$ on the y-axis. The slope and intercept of the plot were equal to ΔS/R and –ΔH/R, respectively [30]. Here, T represents the temperature in Kelvin, K_L is a ratio (q_e/c_e) of the concentrations of Cr(VI) in the solid and liquid phases, and R is the universal gas constant. ΔG represents the change in free energy, ΔH represents the change in enthalpy, and ΔS represents the change in entropy. The negative value of ΔG indicates that the adsorption process occurs spontaneously.

Table 7.1. Thermodynamic behavior of adsorption of Cr(VI) on Fe_3O_4-CHBNC and Fe_3O_4 -KLBNC.

	Temp. (K)	**K_L**	**ΔG (KJ /mol^{-1})**	**ΔH (KJ mol^{-1})**	**ΔS (KJ K^{-1} mol^{-1})**	**R^2**
Fe_3O_4-CHBNC	298	69.88	-10.522	-96.409	-0.289	0.971
	303	12.51	-6.471			
	318	6.11	-4.784			
Fe_3O_4 –KLBNC	298	70.86	-10.556	-116.662	-0.358	0.989
	303	6.379	-4.745			
	318	2.767	-3.485			

7.3.2.6. Adsorption isotherm and kinetics model

The adsorption equilibrium was investigated by fitting the experimental data to the linear equations of the Freundlich (Equation 4.3) and Langmuir (Equation (4.4) isotherm models, as indicated in section 4.3.4.6. One of the main features of the Langmuir isotherm is its ability to predict the affinity between the sorbent and the adsorbate using a dimensionless constant called the separation factor R_L, which is represented by Equation 4.5. In the case of favorable adsorption, R_L ranges from 0 to 1, whereas $R_L > 1$ denotes unfavorable adsorption, $R_L = 1$ denotes linear adsorption, and $R_L = 0$ denotes irreversible adsorption processes [194].

The adsorbate concentration and adsorption capacity at a particular temperature and adsorbent dose are related by adsorption isotherms [7]. The adsorption mechanisms, which rely on variables like surface polarity, surface area, and porosity, are also better understood through the analysis of isotherms. To quantify the equilibrium adsorption data, linear forms of the Freundlich and Langmuir isotherm models were employed [193]. Equation 4.3 represents the Langmuir isotherm for monolayer adsorption on uniform, active sites of homogeneous surfaces.

Figure 7.5 and Table 7.2 display the data for the Langmuir and Freundlich isotherms along with the corresponding correlation coefficients. The Langmuir isotherm model, which depicts monolayer adsorption on a particular site of a homogeneous surface of the adsorbent, is more applicable when the correlation coefficient (R^2) is higher ($R^2 = 0.999$ for Fe_3O_4-CHBNC and $R^2 = 0.998$ for Fe_3O_4-KLBNC) [9].

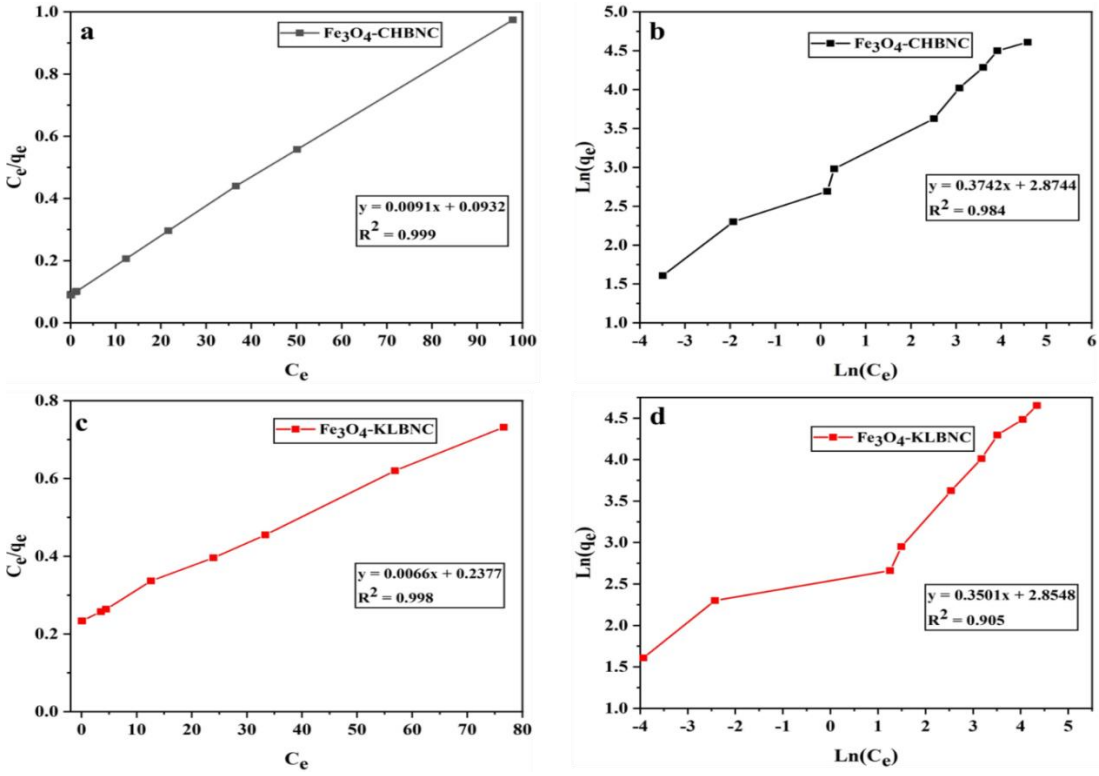

Figure 7.5. (a**)** Langmuir isotherm for Fe_3O_4-CHBNC, **(**b) Freundlich isotherm Fe_3O_4-CHBNC, (c) Langmuir isotherm for Fe_3O_4-KLBNC and (d) Freundlich isotherm Fe_3O_4-KLBNC.

According to the Langmuir isotherm, adsorption energy on the adsorbent surface is expected to be uniform, and there should be no interaction between the adsorbed molecules [13]. The low separation factor values (R_L = 0.339 for Fe_3O_4-CHBNC and R_L= 0.643 for Fe_3O_4-KLBNC) imply a favorable adsorption process. However, multilayered adsorption on heterogeneous surfaces or surface-supporting sites with varying affinities is demonstrated by the Freundlich isotherm [184]**.** The calculated values of *n* falling in the range of 1-10 indicate favorable sorption. Furthermore, the Langmuir isotherm model has a higher regression coefficient R^2 than the Freundlich model (Figure 7.5a and b), showing these results imply monolayer adsorption of Cr(VI) on the surface of both adsorbents, and the Langmuir model offers a better description.

Table 7.2. Langmuir and Freundlich isotherm constants for adsorption of Cr(VI).

Isotherm model	Fe_3O_4-CHBNC	Fe_3O_4-KLBNC
Langmuir	y = 0.0091x + 0.0932	y = 0.0066x + 0.2377
q_m	109.890	151.515
K_L	0.098	0.028
R_L	0.339	0.643
R^2	0.999	0.998
Freundlich	y = 0.3742x + 2.8744	y = 0.350x + 2.8548
n	2.672	2.857
K_F	17.715	17.371
R^2	0.984	0.905

Kinetic studies were conducted using the solution containing 0.1 g of Fe_3O_4-CHBNC and Fe_3O_4-KLBNC separately at a constant concentration of 20 mg L^{-1} at pH 2. The impact of adsorption time was studied for 5–180 min. After shaking at 200 rpm for the specified time, the solutions were filtered, and the concentrations of Cr(VI) were determined. As indicated in section 4.3.4.6, Equation 4.6 was utilized to analyze the adsorbed amount (q_t) of Cr(VI) onto Fe_3O_4-CHBNC and Fe_3O_4-KLBNC at time t. The adsorption kinetics models were evaluated using Equation 4.7 from Section 4.3.4.6, representing the pseudo-first-order kinetics, and Equation 4.8, describing the pseudo-second-order kinetics. Table 7.3 lists the adsorption parameters (R^2 and other constants) that were computed for each of the two models. In this work, the comparison between experimental and calculated q_e values, as well as the higher R^2 values, showed that the adsorption mechanism was found to be better represented by the pseudo-second-order kinetic model. This assumes that the rate limiting step is chemisorption.

Table 7.3. Pseudo-first and second-order adsorption kinetic model constants.

Kinetic Model	Fe_3O_4-CHBNC	Fe_3O_4-KLBNC
$q_{experimental}$	3.995	3.968
Pseudo-first order		
q_e	7.483	3.887
K_1	4.96×10^{-2}	5.06×10^{-2}
R^2	0.901	0.915
Pseudo-second order		
q_e	4.498	4.355
K_2	1.10×10^{-2}	1.70×10^{-2}
R^2	0.989	0.990

7.3.3.7. Comparison of the result with other similar studies

Table 7.4 lists the maximal adsorption capacity and Cr(VI) removal efficiencies of various reported adsorbents. The iron oxide-coffee husk and khat leftover biochar nanocomposites prepared in this study had adsorption capabilities that were higher than some adsorbents and lower than others. The comparison shows that the quantity (mass) of adsorbents utilized in this study is less than that of the earlier studies reported in Table 7.4. This indicates that Fe_3O_4-KLBNC and Fe_3O_4-CHBNC are substitute adsorbents that have the potential to extract Cr(VI) from water solution. Additionally, producing biochar-nanocomposites from coffee husk and khat leftovers provides a useful technique to get rid of potential pollutants by creating value-added treatment products. Coffee husk and khat leftovers are ideal, the cheapest (cost free) biomass for biochar production, and the method is a suitable approach for recourse recovery and environmental protection.

Table 7.4. Comparison of the findings of this study with the Cr(VI) removal effectiveness of a few adsorbents from earlier investigations.

Adsorbent	C_o (mg L^{-1})	Volume (mL)	m (g)	q_m (mg g^{-1})	R (%)	Ref.
ZnO-bagasse biochar	50.00	50.00	0.10	102.66	92	[21]
Modified corn stalk biochar	50.00	50.00	0.10	25.68	ND	[31]
Magnetic woodchip biochar	10.00	50.00	0.50	80.96	95	[88]
Fe_3O_4-Tobaco stem biochar	50	20	0.02	58.74	ND	[212]
Fe_3O_4-Vine shoot biochar	50	15	0.6	305.5	90	[215]
FeS-wheat straw biochar	50.00	42.00	0.72	150.00	95	[153]
Clay-$MnFe_3O_4$ composite	10.00	25.00	0.10	178.60	98.65	[162]
Activated shaddock biochar	20.00	25.00	0.05	9.95	99.2	[205]
Fe_3O_4-CHBNC	20.00	20.00	0.10	109.89	99.83	This
Fe_3O_4-KLBNC	20.00	20.00	0.10	151.52	99.86	study

7.3.3.8 Reusability of the adsorbents

The suggested biochar-nanocomposite adsorbents have the benefits of being reusable and easily separated from soluble waste. Figure 7.6a and b display the reusability test results. According to this study, when the sorbent is recycled for primary use, the comparative adsorption capacity of Fe_3O_4-CHBNC was 99.83% and 99.86% for Fe_3O_4-KLBNC. After six cycles, the values decreased to 84.52% for Fe_3O_4-CHBNC and 89.60% for Fe_3O_4-KLBNC. The result revealed that in the six-cycle process, the adsorption capacities of both adsorbents are promising. Therefore based on the low cost, ease of preparation, and better reusability cycles, Fe_3O_4-CHBNC and Fe_3O_4-KLBNC could be used for Cr(VI) removal.

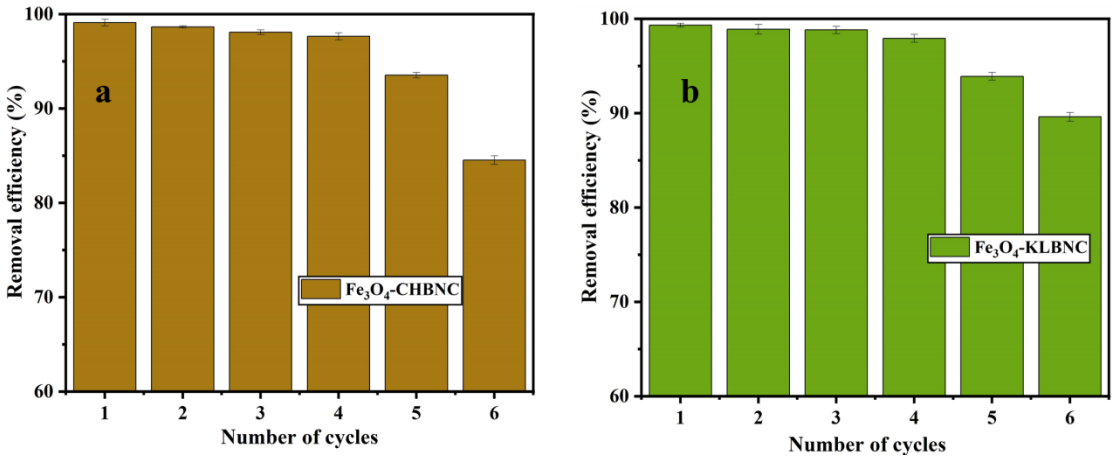

Figure 7.6. Reusability of (a) Fe_3O_4-CHBNC and (b) Fe_3O_4-KLBNC to remove Cr(VI) from aqueous solution.

7.3.4 Summary

Pristine biochar of KL removes 84.78% of Cr(VI) from 20 mg L^{-1} aqueous solutions, while pure biochar of CH, produced by pyrolyzing biomass at 300 °C , removes 74.98%. After pretreating every 25 g of dried biomass with 12.5 mmol of FeS and $FeCl_3$ at a molar ratio of 1:1 and pyrolyzing at 300 °C for one h, each 0.1 g of Fe_3O_4-CHBNC and Fe_3O_4-KLBNC had a 99.83% and 99.86% efficiency in the removal of Cr(VI) from 20 mg L^{-1} aqueous solution, respectively. The maximum removal efficiencies and adsorption capacities were investigated by optimizing parameters like adsorbent dose, pH, contact time, and the initial concentration of the solution.

Equilibrium observations confirmed the monolayer adsorption mechanism of Cr(VI) onto the adsorbents is more dominant and fixed extremely well in the Langmuir isotherm equation. Linear plots were drawn for the Langmuir and Freundlich isotherms in both adsorbents. The value of R_L in the Langmuir isotherm ranges from zero to one, indicating favorable adsorption. A pseudo-second-order model was found to fit the Cr(VI) adsorption data. The findings of this study supported the effectiveness of the suggested method for the production of low-cost carbon materials and the recycling of coffee husk and khat leftovers. This laboratory-scale data can be used as a starting point to conduct studies for designing treatment facilities to remove Cr(VI) from effluents using magnetic iron oxide coffee husk and khat leftover biochar nanocomposites.

CHAPTER EIGHT

8. CONCLUSIONS, RECOMMENDATIONS AND FUTURE PERSPECTIVES

8.1. Conclusions

In this study, MnOx-CHBNC, MnOx-KLBNC, Fe_3O_4-CHBNC, and Fe_3O_4-KLBNC were successfully synthesized using coffee husk, khat leftovers, $KMnO_4$, FeS, and $FeCl_3$. They were characterized, and their efficiency for the removal of MB and Cr(VI) from an aqueous solution was evaluated. The crystallographic structures of the synthesized MnOx-BNC and Fe_3O_4-BNC were analyzed by XRD spectroscopy. Due to the higher amount of carbonaceous composition and non-uniform distribution of metal oxide nanoparticles, the XRD analysis data shows that the adsorbents are amorphous. The functional groups found on the surface of the adsorbents were examined by FTIR spectroscopy and the results revealed that the presence of C-C, C=C, O-H, and C-H are common, but R-MnO_2 and Fe-O were observed in MnOx-BNC and Fe_3O_4-BNC, respectively. Additionally, the results of the FTIR analysis showed that after the adsorption of MB and Cr(VI), significant changes were observed in the peak intensity of some functional groups, indicating that the functional groups are involved in the adsorption process. Based on the BET analysis results, all of the synthesized metal oxide biochars used in this work have pore sizes between 2 and 50 nm, which suggests that the adsorbents have mesoporous structures as defined by IUPAC.

Batch adsorption experiments were conducted to evaluate the effectiveness and adsorption capacities of MnOx-CHBNC, MnOx-KLBNC, Fe_3O_4-CHBNC, and Fe_3O_4-KLBNC in removing MB and Cr(VI) from water.

In one of these studies, the adsorption capacity and removal efficiency of MnOx-CHBNC and MnOx-KLBNC for removing MB from aqueous solution were investigated. The results indicated that both MnOx-CHBNC and MnOx-KLBNC are viable options due to their advantages, such as an easy and fast production process, low cost, higher stability over multiple regeneration cycles, and environmental friendliness. The removal efficiency of MB can be affected by factors such as contact time, adsorbent dose, initial concentration, and temperature. However, changes in pH have an insignificant impact on

the removal efficiency of both adsorbents, making MnOx-CHBNC and MnOx-KLBNC effective for removing MB from both acidic and alkaline solutions.

In another study, the adsorption capacity and removal efficiency of Cr(VI) from an aqueous solution using MnOx-CHBNC and MnOx-KLBNC were evaluated. The results showed that MnOx-CHBNC and MnOx-KLBNC had significantly higher Cr(VI) adsorption capacity and removal efficiency compared to their corresponding unmodified biochars, CHB and KLB. The adsorption process was found to be highly effective at a lower pH, around 2. Comparison with previously reported studies also indicated that MnOx-CHBNC and MnOx-KLBNC could serve as alternative adsorbents for the removal of Cr(VI) from aqueous solutions.

The adsorption capacity and removal efficiency of MB from water using Fe_3O_4-CHBNC and Fe_3O_4-KLBNC as adsorbents were also studied. The results indicated that Fe_3O_4-CHBNC and Fe_3O_4-KLBNC are good options due to their advantages, such as easy and fast production processes, low cost, high stability with several regeneration cycles, and environmentally friendly nature for MB removal. The efficiency of MB removal can be affected by parameters such as contact time, adsorbent dose, initial concentration, and temperature. However, the differences between the lowest and maximum adsorption capacities at pH 3 and 12 are insignificant. The minimum removal efficiencies of Fe_3O_4-CHBNC and Fe_3O_4-KLBNC are 92.22% and 94.27%, respectively, at pH 3. Therefore, Fe_3O_4-CHBNC and Fe_3O_4-KLBNC are more effective in removing MB from acidic and alkaline solutions. The adsorption of MB onto the adsorbents follows the monolayer mechanism, as evidenced by the better fit of the data into the Langmuir isotherm equation. The value of R_L in the Langmuir isotherm equation ranges from zero to one, indicating favorable adsorption.

Furthermore, the adsorption capacity and removal efficiency of Fe_3O_4-CHBNC and Fe_3O_4-KLBNC for the removal of Cr(VI) from water were investigated. The results of the study revealed that Fe_3O_4-CHBNC and Fe_3O_4-KLBNC exhibited significantly higher Cr(VI) adsorption capacity and removal efficiency than their corresponding biochars, CHB and KLB. The results indicated that the adsorption capacity depends on contact time, adsorbent dose, temperature, and pH changes. For effective adsorption, the pH of the solution should be around 2. When the pH value is greater than 5 the adsorption capacity decreases significantly. Cr(VI) adsorption onto adsorbents is monolayer

adsorption and is well defined by the Langmuir isotherm. The R_L value of the Langmuir isotherm ranges from zero to one for favorable adsorption. The Cr(VI) adsorption data fits well with the pseudo-second-order model. The comparison between the reported studies and the Cr(VI) removal efficiency achieved in this study shows that Fe_3O_4-CHBNC and Fe_3O_4-KLBNC can be used as alternative adsorbents to remove Cr(VI) from aqueous solution.

Generally, the findings revealed that MnOx-CHBNC, MnOx-KLBNC, Fe_3O_4-CHBNC, and Fe_3O_4-KLBNC are efficient and effective in removing MB and Cr(VI) from water. The synthesis of these adsorbents offers dual advantages. Firstly, the intensive use of CH and KL in this process will reduce environmental pollution and the hazardous effects of their unattended disposal. Secondly, MnOx-CHBNC, MnOx-KLBNC, Fe_3O_4-CHBNC, and Fe_3O_4-KLBNC can serve as cheap, easily prepared, and environmentally friendly alternative adsorbents for the removal of MB and Cr(VI). Furthermore, Comparison study of the four adsorbents in terms of their efficiency for MB and Cr(VI) removal revealed that Fe_3O_4-KLB is the most effective followed by Fe_3O_4-CHBN.

8.2. Recommendations and Future Perspectives

The application of biochar nanocomposite materials is a viable approach to environmentally friendly water treatment, as it aligns with sustainable environmental principles and green chemistry. While biochar alone serves as an effective adsorbent for the removal of contaminants from water, biochar nanocomposites enhance its performance. By adding of nanoparticles, researchers can increase its surface area and introduce new functionalities. This leads to improved adsorption capacity and efficiency for the removal of target contaminants, such as heavy metals, new compounds, and organic pollutants.

CHBNC and KLBNC materials demonstrate a promising future prospective in water treatment, in line with the principles of green chemistry and environmental sustainability. Pollutants, like Cr(VI) and MB can be efficiently removed from water by using CHBNC and KLBNC, especially when modified with metal oxides and magnetic iron oxide. KH and KL are agricultural byproducts, easily accessible and continuously generated.

Biochar nanocomposite materials offer a sustainable and potentially powerful technology for water treatment, making a significant contribution to green chemistry and a clean environment. However, research is still ongoing to optimize production methods, ensure long-term stability, and assess potential environmental impacts throughout the life cycle of these nanocomposite materials. Therefore, biochar nanocomposites made from CH and KL present a viable environmentally friendly approach for water treatment. These materials can be further improved through additional studies and development, eventually becoming a more well-known and beneficial environmentally friendly alternative.

In Ethiopia, the annual demand for foreign currency and export commodities is increasing annually. Coffee and khat are the primary Ethiopian export products, and their production on the rise. However, the intensive production of CH and KL is causing environmental pollution due to their massive byproducts. Therefore, converting these byproducts into useful materials, such as metal oxide biochar nanocomposites is crucial.

The following are the recommendations for future studies on MnOx-CHBNC, MnOx-KLBNC, Fe_3O_4-CHBNC, and Fe_3O_4-KLBNC:

- Optimization of parameters for the production of Fe_3O_4-CHBNC and Fe_3O_4-KLBNC involves adjusting the pyrolysis process, including the biomass-to-activator ratio, pyrolysis temperature, and residence time.
- Further characterization of the adsorbents using EDX, TEM, and Raman spectroscopy.
- Test for removal efficiency of the adsorbents for other toxic dyes and heavy metals.
- Test for the photo-catalytic effect of these materials on MB and other toxic dyes.
- Study for the catalytic effect of MnOx-CHBNC, MnOx-KLBNC, Fe_3O_4-CHBNC, and Fe_3O_4-KLBNC for Cr(VI).
- Conducting pilot-scale studies and applying them to real wastewater treatments to validate the laboratory-scale findings in practical settings.
- Performing environmental impact assessments, such as life cycle analysis, to quantify the sustainability benefits of the biochar nanocomposites.

REFERENCES

[1] Thompson, L. A.; Darwish, W. S. Environmental chemical contaminants in food: review of a global problem. *J. Toxicol.*, **2019**, *2019*, 1–15.

[2] Ogoyi, D.; Mwita, C.; Nguu, E.; Shiundu, P. Determination of heavy metal content in water, sediment and microalgae from Lake Victoria, East Africa. *Open Environ. Eng. J.*, **2011**, *4* (1), 156–161.

[3] Liang, Y.; Yi, X.; Dang, Z.; Wang, Q.; Luo, H.; Tang, J. heavy metal contamination and health risk assessment in the vicinity of a tailing pond in Guangdong, China. *Int. J. Environ. Res. Public Health*, **2017**, *14*, 1557.

[4] Kacholi, D. S.; Sahu, M. Levels and health risk assessment of heavy metals in soil, water, and vegetables of Dar Es Salaam, Tanzania. *J. Chem.*, **2018**, 1–9.

[5] Yousaf, B.; Liu, G.; Wang, R.; Imtiaz, M.; Zia-ur-Rehman, M.; Munir, M. A. M.; Niu, Z. Bioavailability evaluation, uptake of heavy metals and potential health risks via dietary exposure in urban-industrial areas. *Environ. Sci. Pollut. Res.*, **2016**, *22*, 22443–22453.

[6] De Caprariis, B.; De Filippis, P.; Petrucci, E.; Scarsella, M. Activated biochars used as adsorbents for dyes removal. *Chem. Eng. Trans.*, **2018**, *65*.

[7] Xu, G.; Zhu, Y.; Wang, X.; Wang, S.; Cheng, T.; Ping, R.; Cao, J.; Lv, K. Novel chitosan and laponite based nanocomposite for fast removal of Cd(II), methylene blue and congo red from aqueous solution. *e-Polymers*, **2019**, *19*, 244–256.

[8] Cornelia, P.; Oana, P.; Ianos, R.; Simona, G. M. Effective removal of methylene blue from aqueous solution using a new magnetic iron oxide nanosorbent prepared by combustion synthesis. *Clean Techn Env. Policy*, **2016**, *18*, 705–715.

[9] Swan, N. B.; Zaini, M. A. A. Adsorption of malachite green and congo red dyes from water: recent progress and future outlook. *Ecol. Chem. Eng. S*, **2019**, *26* (1), 119–132.

[10] Khoshsang, H.; Ghaffarinejad, A.; Kazemi, H.; Jabarian, S. Synthesis of Mesoporous Fe_3O_4 and Fe_3O_4/C Nanocomposite for removal of hazardous dye from aqueous media. *J. Water Environ. Nanotechnol*, **2018**, *3* (3), 191–206.

[11] Ruan, W.; Hu, J.; Qi, J.; Hou, Y.; Zhou, C.; Wei, X. Removal of dyes from wastewater by nanomaterials : a review. *Adv. Mater. Lett.*, **2019**, *10* (1), 9–20.

[12] Parakala, S.; Moulik, S.; Sridhar, S. Effective separation of methylene blue dye from aqueous solutions by integration of micellar enhanced ultrafiltration with

vacuum membrane distillation. *Chem. Eng. J.*, **2019**, *375*, 122015.

[13] Singh, S.; Kumar, A.; Jyoti, P.; Chakraborty, P.; Kumar, M. Adsorption potential of biochar obtained from pyrolysis of raw and torrefied *Acacia Nilotica* towards removal of methylene blue dye from synthetic wastewater. *Biomass Convers. Biorefinery*, **2021**.

[14] Maniyam, M. N.; Hari, M. Optimization of culture conditions for improved green biodecolorization of methylene blue by *Rhodococcus Pyridinivorans Strain* UCC 0003. *J. Biotechnol. Comput. Biol. Bionanotechnol.*, **2021**, *102* (2), 125–140.

[15] Reguieg, I.; Diaf, K.; Elbahri, Z. Adsorption rate and capacity assessment of methylene blue removal by biocomposite microparticles using design of experiments. *Int. J. Environ. Res.*, **2022**, *16* (6), 1–14.

[16] Khodabandehloo, A.; Rahbar-Kelishami, A.; Shayesteh, H. methylene blue removal using *Salix Babylonica* (Weeping Willow) leaves powder as a low-cost biosorbent in batch mode: kinetic, equilibrium, and thermodynamic studies. *J. Mol. Liq.*, **2017**, *244*, 540–548.

[17] Momodu, M. A.; Anyakora, C. A. Heavy metal contamination of ground water: the Surulere case study. *Res. J. Environ. Earth Sci.*, **2010**, *2* (1), 39–43.

[18] Gorchev, H. G.; Ozolins, G. Guidelines for drinking-water quality, 3rd edition. In *Who*; 2004; Vol. 1, pp 296–459.

[19] Jaishankar, M.; Tseten, T.; Anbalagan, N.; Mathew, B. B.; Beeregowda, K. N. Toxicity, mechanism and health effects of some heavy metals. *Interdiscip. Toxicol.*, **2014**, *7* (2), 60–72.

[20] WHO. Health risks of heavy metals from long-range trans boundary air pollution,. *WHO*. Denmark 2007, pp 1–85.

[21] Gan, C.; Liu, Y.; Tan, X.; Wang, S.; Zeng, G. Effect of porous zinc – biochar nanocomposites on Cr(VI) adsorption from aqueous solution. *RSC Adv.*, **2015**, *5*, 35107–35115.

[22] Barrera-Díaz, C. E.; Lugo-Lugo, V.; Bilyeu, B. A review of chemical, electrochemical and biological methods for aqueous Cr(VI) Reduction. *J. Hazard. Mater.*, **2012**, *223–224*, 1–12.

[23] Wang, H.; Wang, W.; Zhou, S.; Gao, X. Adsorption mechanism of Cr(VI) on woody-activated carbons. *Heliyon*, **2023**, *9* (2), e13267.

[24] Anjum, A.; Ali, S.; Hashmi, Z.; Sattar, A.; Abro, R.; Waheed, A.; Mujawar, N. A review of novel green adsorbents as a sustainable alternative for the remediation of

chromium (VI) from Water Environments. *Heliyon*, **2023**, *9* (5), e15575.

[25] Marghaki, N. S.; Jonoush, Z. A.; Rezaee, A. Improving the performance of Cr(VI) removal by electrochemical process using microbial cellulose/magnetic nanoparticles electrode. *J. Clean. Prod.*, **2020**, *277*, 123195.

[26] Dharnaik, A. S.; Ghosh, P. K. Hexavalent chromium [Cr(VI)] removal by the electrochemical ion-exchange process. *Environ. Technol.*, **2014**, *35* (18), 2272–2279.

[27] Jouali, A.; Salhi, A.; Aguedach, A.; Aarfane, A.; Ghazzaf, H.; Lhadi, E. K.; El krati, M.; Tahiri, S. Photo-catalytic degradation of methylene blue and reactive blue 21 dyes in dynamic mode using TiO_2 particles immobilized on cellulosic fibers. *J. Photochem. Photobiol. A Chem.*, **2019**, *383*, 112013.

[28] Wang, X.; Liu, X.; Yuan, F.; Wang, B. Selective decolorization of methylene blue from methyl orange in heterogeneous fenton - like reaction. *Int. J. Environ. Res.*, **2023**, *17* (1), 1–13.

[29] Abd-Elhamid, A. I.; Emran, M.; El-Sadek, M. H.; El-Shanshory, A. A.; Soliman, H. M. A.; Akl, M. A.; Rashad, M. Enhanced removal of cationic dye by eco-friendly activated biochar derived from rice straw. *Appl. Water Sci.*, **2020**, *10*, 45.

[30] Singh, S.; Anil, A. G.; Khasnabis, S.; Kumar, V.; Nath, B.; Adiga, V.; Kumar Naik, T. S. S.; Subramanian, S.; Kumar, V.; Singh, J.; et al. Sustainable removal of Cr(VI) using graphene oxide-zinc oxide nanohybrid: adsorption kinetics, isotherms and thermodynamics. *Environ. Res.*, **2022**, *203*, 111891.

[31] An, Q.; Li, X.; Nan, H.; Yu, Y.; Jiang, J. The potential adsorption mechanism of the biochars with different modification processes to Cr (VI). *Environ. Sci. Pollut. Res.*, **2018**, *25*, 31346–31357.

[32] Tan, X. fei; Liu, Y. guo; Gu, Y. ling; Xu, Y.; Zeng, G. ming; Hu, X. jiang; Liu, S. bo; Wang, X.; Liu, S. mian; Li, J. Biochar-based nano-composites for the decontamination of wastewater: a review. *Bioresour. Technol.*, **2016**, *212*, 318–333.

[33] Mohan, D.; Sarswat, A.; Ok, Y. S.; Pittman, C. U. Organic and inorganic contaminants removal from water with biochar, a renewable, low cost and sustainable adsorbent - a critical review. *Bioresour. Technol.*, **2014**, *160*, 191–202.

[34] Tan, X.; Liu, Y.; Zeng, G.; Wang, X.; Hu, X.; Gu, Y.; Yang, Z. Application of biochar for the removal of pollutants from aqueous solutions. *Chemosphere*, **2015**, *125*, 70–85.

[35] Yang, H.; Yan, R.; Chen, H.; Zheng, C.; Lee, D. H.; Uni, V.; V, N. D.; March, R. V; Re, V.; Recei, M. In-depth investigation of biomass pyrolysis based on three major components : hemicellulose , cellulose and lignin. *Energy & Fuels*, **2006**, *20*, 388–393.

[36] Godwin, P. M.; Pan, Y.; Xiao, H.; Afzal, M. T. Progress in preparation and application of modified biochar for improving heavy metal ion removal from wastewater. *J. Bioresour. Bioprod.*, **2019**, *4* (1), 31–42.

[37] Rezaee, M.; Assadi, Y.; Hosseini, M. M. Determination of organic compounds in water using dispersive liquid – liquid microextraction. *J. Chromatogr. A*, **2006**, *1116*, 1–9.

[38] Yao, Z.; Du, S.; Zhang, Y.; Zhu, B.; Zhu, L.; John, A. E. Positively charged membrane for removing low concentration Cr(VI) in ultrafiltration Process. *J. Water Process Eng.*, **2015**, *8*, 99–107.

[39] Chakraborty, S.; Dasgupta, J.; Farooq, U.; Sikder, J.; Drioli, E.; Curcio, S. Experimental analysis, modeling and optimization of chromium (VI) removal from aqueous solutions by polymer-enhanced ultrafiltration. *J. Memb. Sci.*, **2014**, *456*, 139–154.

[40] Verma, B.; Balomajumder, C. Hexavalent chromium reduction from real electroplating wastewater by chemical precipitation. *Bull. Chem. Soc. Ethiop.*, **2020**, *34* (1), 67–74.

[41] Gheju, M.; Balcu, I. Removal of chromium from Cr(VI) polluted wastewaters by reduction with scrap iron and subsequent precipitation of resulted cations. *J. Hazard. Mater.*, **2011**, *196*, 131–138.

[42] Xu, T.; Zhou, Y.; Lei, X.; Hu, B.; Chen, H.; Yu, G. Study on highly efficient Cr(VI) removal from wastewater by sinusoidal alternating current coagulation. *J. Environ. Manage.*, **2019**, *249*, 109322.

[43] Fan, L.; Zhou, Y.; Yang, W.; Chen, G.; Yang, F. Electrochemical degradation of aqueous solution of amaranth azo dye on ACF under potentiostatic model. *Dye. Pigment.*, **2008**, *76*, 440–446.

[44] Pan, J.; Jiang, J.; Xu, R. Adsorption of Cr(III) from acidic solutions by crop straw derived biochars. *J. Environ. Sci.*, **2013**, *25* (10), 1957–1965.

[45] Fradj, A. Ben; Hamouda, S. Ben; Ouni, H.; Lafi, R.; Gzara, L.; Hafiane, A. Removal of methylene blue from aqueous solutions by poly(acrylic acid) and poly(ammonium acrylate) assisted ultrafiltration. *Sep. Purif. Technol.*, **2014**, *133*,

76–81.

[46] Duan, X.; Wu, P.; Pi, K.; Zhang, H.; Liu, D.; Gerson, A. R. Application of modified electrocoagulation for efficient color removal from synthetic methylene blue wastewater. *Int. J. Electrochem. Sci.*, **2018**, *13*, 5575–5588.

[47] Liu, Y.; Zhao, X.; Li, J.; Ma, D.; Han, R. Characterization of bio-char from pyrolysis of wheat straw and its evaluation on methylene blue adsorption. *Desalin. Water Treat.*, **2012**, *46*, 115–123.

[48] Gebremikal, E. T.; Motuma, M. T.; Ayele, A.; Getachew, D. Phycoremediation of synthetic dyes in an aqueous solution using an indigenous oscillatoria Sp., from Ethiopia. *Ethiop. J. Sci. Sustain. Dev.*, **2020**, *7* (2).

[49] Nartey, O. D.; Zhao, B. Biochar preparation, characterization, and adsorptive capacity and its effect on bioavailability of contaminants: an overview. *Adv. Mater. Sci. Eng.*, **2014**, 1–13.

[50] Sakhiya, A. K.; Anand, A.; Kaushal, P. Production, activation, and applications of biochar in recent times. *Biochar*, **2020**, *2* (3), 253–285.

[51] Amamo, A. A. Coffee Production and marketing in Ethiopia. *Eur. J. Bus. Manag.*, **2014**, *6* (37), 109–122.

[52] Kumari, S.; Hari, S.; Annamareddy, K. Treatment of garage wastewater using activated carbon made from khat (*Catha Edulis*) and Neem (*Azadirachta Indica*) leaves. *Environ. Dev. Sustain.*, **2019**.

[53] Ketema, T.; Yohannes, M.; Alemayehu, E.; Ambelu, A. Effect of chronic khat *(Catha Edulis* , Forsk) use on outcome of *Plasmodium Berghe*i ANKA infection in *Swiss Albino* mice. *BMC Infect. Dis.*, **2015**, *15* (170), 1–11.

[54] Hoseini, M.; Cocco, S.; Casucci, C.; Cardelli, V.; Corti, G. Coffee by-products derived resources. a review. *Biomass and Bioenergy*, **2021**, *148*, 106009.

[55] Kebede, T.; Berhe, D. T.; Zergaw, Y. Combustion characteristics of briquette fuel produced from biomass residues and binding materials. *J. energy*, **2022**.

[56] Wu, C.; Zhang, G.; Zhang, P.; Chang, C. Disintegration of excess activated sludge with potassium permanganate : feasibility , mechanisms and parameter optimization. *Chem. Eng. J.*, **2014**, *240*, 420–425.

[57] Wang, H.; Gao, B.; Wang, S.; Fang, J.; Xue, Y.; Yang, K. Removal of Pb(II), Cu(II), and Cd(II) from aqueous solutions by biochar derived from $KMnO_4$ treated hickory wood. *Bioresour. Technol.*, **2015**, *197*, 356–362.

[58] Kiran; Bharti, R.; Sharma, R. Effect of heavy metals: an overview. *Mater. Today*

Proc., **2021**, *51*, 880–885.

[59] Garai, P.; Banerjee, P.; Mondal, P.; Saha, N. C. Effect of Heavy Metals on Fishes: Toxicity and Bioaccumulation. *J. Clin. Toxicol.*, **2021**, *11*, 1.

[60] Sodhi, K. K.; Mishra, L. C.; Singh, C. K.; Kumar, M. Perspective on the heavy metal pollution and recent remediation strategies. *Curr. Res. Microb. Sci.*, **2022**, *3*, 100166.

[61] Helaluddin, A. B. M.; Khalid, R. S.; Alaama, M.; Abbas, S. A. Main analytical techniques used for elemental analysis in various matrices. *Trop. J. Pharm. Res.*, **2016**, *15* (2), 427–434.

[62] Addis, W.; Abebaw, A. Determination of heavy metal concentration in soils used for cultivation of *Allium Sativum* L. (Garlic) in East Gojjam Zone, Amhara Region, Ethiopia. *Cogent Chem.*, **2017**, *3*, 1–12.

[63] Dima, G.; Popescu, I. O. N. V; Stihi, C.; Oros, C.; Dinu, S.; Manea, L.; Vlaicu, G. Fe, Mn and Zn concentrations determination from Ialomipa river by atomic absorption spectroscopy. *Rom. J. Phys.*, **2006**, *51* (5–6), 667–674.

[64] Atashi, H.; Sahebi-Shahemabadi, M.; Mansoorkiai, R.; Spaili, F. A. Cobalt in zahedan drinking water. *J. Appl. Sci. Res.*, **2009**, *5* (12), 2203–2207.

[65] Hawrami, K.; Mezuri, H. Assessing risks to human health from potentially toxic elements in drinking water of Duhok Province/ Kurdistan region of Iraq. *J. Environ. Pollut. Hum. Heal.*, **2014**, *2* (2), 44–51.

[66] Oghenerobor, B. A.; Gladys, O. O.; Tomilola, D. O. Heavy metal pollutants in wastewater effluents: sources, effects and remediation. *Adv. Biosci. Bioeng.*, **2014**, *2* (4), 37.

[67] Mahmood, T.; Aslam, M.; Naeem, A.; Siddique, T.; Din, S. U. Adsorption of As(III) from aqueous solution onto iron impregnated used tea activated carbon: equilibrium, kinetic and thermodynamic study. *J. Chil. Chem. Soc.*, **2018**, *63* (1), 3855–3866.

[68] Kirti, S.; Sreemoyee, C.; Bhumika, J. Chromium toxicity and its health hazards. *Int. J. Adv. Res.*, **2015**, *3* (7), 167–172.

[69] Hanain, M. F. and S. Cr impact on environment and its appropriate remediations. *Jorunal Pharmacol. Toxicol.*, **2006**, *1* (3), 248–258.

[70] Sankhla, M. S.; Kumari, M.; Nandan, M.; Kumar, R.; Agrawal, P. Heavy Metals contamination in water and their hazardous effect on human health-a review. *Int. J. Curr. Microbiol. Appl. Sci.*, **2019**, *5* (10), 759–766.

[71] Wise, J. P.; Young, J. L.; Cai, J.; Cai, L. Current understanding of hexavalent chromium [Cr(VI)] neurotoxicity and new perspectives. *Environ. Int.*, **2022**, *158*, 106877. https://doi.org/10.1016/j.envint.2021.106877.

[72] Ukhurebor, K. E.; Aigbe, U. O.; Onyancha, R. B.; Nwankwo, W.; Osibote, O. A.; Paumo, H. K.; Ama, O. M.; Adetunji, C. O.; Siloko, I. U. Effect of hexavalent chromium on the environment and removal techniques: a review. *J. Environ. Manage.*, **2021**, *280* (September 2020), 111809.

[73] Liang, J.; Huang, X.; Yan, J.; Li, Y.; Zhao, Z.; Liu, Y.; Ye, J.; Wei, Y. A Review of the formation of Cr(VI) via Cr(III) oxidation in soils and groundwater. *Sci. Total Environ.*, **2021**, *774*, 145762.

[74] Mahipal, S. S.; Rajeev, K. Contaminant of heavy metals in groundwater & its toxic effects on human health & environment. *Int. J. Environ. Sci. Nat. Resour.*, **2019**, *18* (5), 0149–0153.

[75] Malik, Q.; Khan, M. Effect on human health due to drinking water contaminated with heavy metals. *J. Pollut. Eff. Control*, **2016**, *05* (01), 10–11.

[76] Ding, K.; Zhou, X.; Hadiatullah, H.; Lu, Y.; Zhao, G.; Jia, S.; Zhang, R.; Yao, Y. Removal performance and mechanisms of toxic hexavalent chromium (Cr(VI)) with $ZnCl_2$ enhanced acidic vinegar residue biochar. *J. Hazard. Mater.*, **2021**, *420*, 126551.

[77] Hassaan, M. A.; Nemr, A. El. Health and environmental impacts of dyes : mini review. *Am. J. Environ. Sci. Eng.*, **2017**, *1* (3), 64–67.

[78] Saini, R. D. Textile Organic Dyes: Polluting effects and elimination methods from textile waste water. *Int. J. Chem. Eng. Res.*, **2017**, *9* (1), 975–6442.

[79] Terefe Tolcha, P. Khat marketing and its export performance in the Ethiopian economy. *Sci. Res.*, **2020**, *8* (4), 90.

[80] Dadi, D.; Daba, G.; Beyene, A.; Luis, P.; Van der Bruggen, B. Composting and co-composting of coffee husk and pulp with source-separated municipal solid waste: a breakthrough in valorization of coffee waste. *Int. J. Recycl. Org. Waste Agric.*, **2019**, *8* (3), 263–277.

[81] Desai, N. M.; Varun, E.; Patil, S.; Pimpley, V.; Murthy, P. S. *Hand Book of Environmental Materials Management*; Hussain, C. M., Ed.; Springer Nature Switzerland, 2020.

[82] Castaldo, L.; Graziani, G.; Gaspari, A.; Izzo, L.; Luz, C.; Mañes, J.; Rubino, M.; Meca, G.; Ritieni, A. Study of the chemical components, bioactivity and antifungal properties of the coffee Husk. *J. Food Res.*, **2018**, *7* (4), 43.

[83] Setter, C.; Ataíde, C. H.; Mendes, R. F.; De-Oliveira, T. J. P. Influence of particle size

on the physico-mechanical and energy properties of briquettes produced with coffee husks. *Environ. Sci. Pollut. Res.*, **2021**, *28* (7), 8215–8223.

[84] Amena, B. T.; Tibba, G. S.; Lemu, H. G. Analysis of the negative impacts of coffee husk on the local environment. *Res. Sq.*, **2022**, 1–17.

[85] Kueh, A. H.; Samarahan, K. Spent ground coffee awaking the sustainability prospects. *Environ. Toxicol. Manag.*, **2021**, *1*, 1–6.

[86] Gabriel, T.; Wondu, K.; Dilebo, J. Valorization of khat (*Catha Edulis*) waste for the production of cellulose fibers and nanocrystals. *PLoS One*, **2021**, *16* (2), 1–20.

[87] Afessa, G.; Saka, A.; Tesfaye, J. L.; Nagaprasad, N.; Shanmugam, R.; Dwarampudi, L. P.; Venkatesh, S.; Badassa, B.; Krishnaraj, R. Synthesis of plant-derived khat waste for environmental application. *J. Nanomater.*, **2022**.

[88] Santhosh, C.; Daneshvar, E.; Tripathi, K. M.; Baltrėnas, P.; Kim, T. Y.; Baltrėnaitė, E.; Bhatnagar, A. Synthesis and characterization of magnetic biochar adsorbents for the removal of Cr(VI) and acid orange 7 dye from aqueous solution. *Environ. Sci. Pollut. Res.*, **2020**, *27*, 32874–32887.

[89] Tong, X. J.; Li, J. Y.; Yuan, J. H.; Xu, R. K. Adsorption of Cu(II) by biochars generated from three crop straws. *Chem. Eng. J.*, **2011**, *172*, 828–834.

[90] Moazzam, A.; Jamil, N.; Nadeem, F.; Qadir, A.; Ahsan, N.; Zameer, M. Reactive dye removal by a novel biochar/ MgO nanocomposite. *J. Chem. Soc. Pakistan*, **2017**, *39* (01), 26–34.

[91] Ghorbani-Khosrowshahi, S.; Behnajady, M. A. Chromium(VI) adsorption from aqueous solution by prepared biochar from onopordom heteracanthom. *Int. J. Environ. Sci. Technol.*, **2016**, *13* (7), 1803–1814.

[92] Gunathilake C, F. C. N. K. C. P. N. P. H. A. Methylene blue adsorption onto surface modified beli (aegle marmelos) fruit shell biochar. *Biomed. J. Sci. Tech. Res.*, **2018**, *11* (5), 8730–8738.

[93] Kyi, P. P.; Quansah, J. O.; Lee, C. G.; Moon, J. K.; Park, S. J. The removal of crystal violet from textile wastewater using palm kernel shell-derived biochar. *Appl. Sci.*, **2020**, *10* (2251), 1–13.

[94] Chwastowski, J.; Bradło, D.; Żukowski, W. Adsorption of cadmium, manganese and lead ions from aqueous solutions using spent coffee grounds and biochar produced by its pyrolysis in the fluidized bed reactor. *Materials (Basel).*, **2020**, *13* (12), 1–14.

[95] Chen, X.; Chen, G.; Chen, L.; Chen, Y.; Lehmann, J.; McBride, M. B.; Hay, A. G. Adsorption of copper and zinc by biochars produced from pyrolysis of hardwood and corn straw in aqueous solution. *Bioresour. Technol.*, **2011**, *102* (19), 8877–8884.

[96] Fayanto, S.; Naba, S. D.; Ahmanas, S. R.; Nugraha, N. Adsorption of heavy metals based on the bio-removal method. *AIP Conf. Proc.*, **2019**, *2169* (060003), 0–7.

[97] Pellera, F. M.; Giannis, A.; Kalderis, D.; Anastasiadou, K.; Stegmann, R.; Wang, J. Y.; Gidarakos, E. Adsorption of Cu(II) ions from aqueous solutions on biochars prepared from agricultural by-products. *J. Environ. Manage.*, **2012**, *96* (1), 35–42.

[98] Ray, P. Z.; Shipley, H. J. Inorganic nano-adsorbents for the removal of heavy metals and arsenic: a review. *RSC Adv.*, **2015**, *5*, 29885–29907.

[99] Lu, F.; Astruc, D. Nanomaterials for removal of toxic elements from water. *Coord. Chem. Rev.*, **2018**, *356*, 147–164.

[100] Huang, Q.; Song, S.; Chen, Z.; Hu, B.; Chen, J.; Wang, X. Biochar-based materials and their applications in removal of organic contaminants from wastewater: State-of-the-art review. *Biochar*, **2019**, *1* (1), 45–73.

[101] Motasemi, F.; Afzal, M. T. A Review on the microwave-assisted pyrolysis technique. *renew. Sustain. Energy Rev.*, **2013**, *28*, 317–330.

[102] Islam, A.; Auta, M.; Kabir, G.; Hameed, B. H. A thermogravimetric analysis of the combustion kinetics of karanja (*Pongamia Pinnata*) fruit hulls char. *Bioresour. Technol.*, **2016**, *200*, 335–341.

[103] Chen, Z.; Jing, Y.; Wang, Y.; Meng, X.; Zhang, C.; Chen, Z.; Zhou, J.; Qiu, R.; Zhang, X. enhanced removal of aqueous Cd(ii) by a biochar derived from salt-sealing pyrolysis coupled with naoh treatment. *Appl. Surf. Sci.*, **2020**, *511* (145619), 1–11.

[104] Palma, C. F. Modelling of tar formation and evolution for biomass gasification : a review. *Appl. Energy*, **2013**, *111*, 129–141.

[105] Waheed, Q. M. K.; Williams, P. T. Hydrogen production from high temperature pyrolysis / steam reforming of waste biomass : rice husk , sugar cane bagasse , and wheat straw. *Energy & Fuels*, **2013**, *27*, 6695−6704.

[106] Colomba, D. B. modeling chemical and physical processes of wood and biomass pyrolysis. *Prog. Energy Combust. Sci.*, **2008**, *34*, 47–90.

[107] Celso, G. M.; Rapagna, S. Devolatilization of wood particles in a hot fluidized bed : product yields and conversion rates. *Biomass and Bioenergy*, **2008**, *32*, 1123–1129.

[108] Yang, X.; Zhang, S.; Ju, M.; Liu, L. preparation and modification of biochar materials and their application in soil remediation. *Appl. Sci.*, **2019**, *9*, 1365.

[109] Tomczyk, A.; Sokołowska, Z.; Boguta, P. Biochar physicochemical properties: pyrolysis temperature and feedstock kind effects. *Rev. Environ. Sci. Biotechnol.*, **2020**, *19* (1), 191–215.

[110] Tessfaw, Z. A.; Beyene, A.; Nebiyu, A.; Pikoń, K.; Landrat, M. Co-composting of

khat-derived biochar with municipal solid waste: a sustainable practice of waste management. *Sustain.*, **2020**, *12* (24), 1–14.

[111] Teli, M. D.; Terega, J. M. Chemical , Physical and thermal characterization of ensete ventricosum plant fibre. *Int. Res. J. Eng. Technol.*, **2017**, *04* (12), 67–75.

[112] Gabriel, T.; Belete, A.; Syrowatka, F.; Neubert, R. H. H.; Gebre-mariam, T. Extraction and characterization of celluloses from various plant byproducts. *Int. J. Biol. Macromol.*, **2020**, *158*, 1248–1258.

[113] Oliveira, F. D. C.; Srinivas, K.; Helms, G. L.; Nancy, G.; Cort, J. R.; Gonçalves, A. R.; Ahring, B. K. Characterization of coffee (*Coffea Arabica)* husk lignin and degradation products obtained after oxygen and alkali addition. *Bioresour. Technol.*, **2018**, 1–38..

[114] Tolesa, L. D.; Gupta, B. S.; Lee, M. Treatment of coffee husk with ammonium-based ionic liquids : lignin extraction , degradation , and characterization. *ACS Omega*, **2018**, *3*, 10866–10876.

[115] Tesfaye, G.; Kebede, W.; Jemal, D. Valorization of Khat (*Catha Edulis*) waste for the production of cellulose fibers and nanocrystals. *PLoS One*, **2021**, *16* (2), 1–20.

[116] Wang, J.; Tan, Y.; Yang, H.; Zhan, L.; Sun, G.; Luo, L. On the adsorption characteristics and mechanism of methylene blue by ball mill modified biochar. *Sci. Rep.*, **2023**, *13* (1), 1–12.

[117] Ge, Q.; Li, P.; Liu, M.; Xiao, G. ming; Xiao, Z. qian; Mao, J. wei; Gai, X. kun. Removal of methylene blue by porous biochar obtained by KOH activation from bamboo biochar. *Bioresour. Bioprocess.*, **2023**, *10* (1).

[118] Hassaan, M. A.; Yılmaz, M.; Helal, M.; El-Nemr, M. A.; Ragab, S.; El Nemr, A. Improved methylene blue adsorption from an aqueous medium by ozone-triethylenetetramine modification of sawdust-based biochar. *Sci. Rep.*, **2023**, *13* (1), 1–20.

[119] Venkatraman, Y.; Arunkumar, P.; Kumar, N. S.; Osman, A. I.; Muthiah, M.; Al-Fatesh, A. S.; Koduru, J. R. Exploring modified rice straw biochar as a sustainable solution for simultaneous Cr(VI) and Pb(II) removal from wastewater: characterization, mechanism insights, and application feasibility. *ACS Omega*, **2023**, *8* (41), 38130–38147.

[120] Zhou, J.; Chen, H.; Thring, R. W.; Arocena, J. M. Chemical pretreatment of rice straw biochar: effect on biochar properties and hexavalent chromium adsorption. *Int. J. Environ. Res.*, **2019**, *13* (1), 91–105.

[121] Fan, L. Q.; Liu, Q.; Wan, Y.; Wang, X. D.; Miao, J. X.; Cai, J.; Chen, W.; Chen, F. H.; Cheng, L.; Ji, L. Hexavalent chromium adsorption removal from aqueous solution by

Fe-modified biochar derived from rice straw. *Appl. Ecol. Environ. Res.*, **2019**, *17* (6), 15311–15327.

[122] Salgado, M. D. F.; Abioye, A. M.; Junoh, M. M.; Santos, J. A. P.; Ani, F. N. Preparation of activated carbon from *Babassu endocarpunder* microwave radiation by physical activation. *Earth Environ. Sci.*, **2018**, *105* (1), 1–14.

[123] Enaime, G.; Baçaoui, A.; Yaacoubi, A.; Lübken, M. Biochar for wastewater treatment-conversion technologies and applications. *Appl. Sci.*, **2020**, *10*, 3492.

[124] Wu, H.; Feng, Q.; Yang, H.; Alam, E.; Gao, B.; Gu, D. Modified biochar supported Ag/Fe nanoparticles used for removal of cephalexin in solution : characterization , kinetics and mechanisms. *Colloids Surfaces A Physicochem. Eng. Asp.*, **2017**, *517*, 63–71.

[125] Peng, P.; Lang, Y.; Wang, X. Adsorption behavior and mechanism of pentachlorophenol on reed biochars : pH effect , pyrolysis temperature , hydrochloric acid treatment and isotherms. *Ecol. Eng.*, **2016**, *90*, 225–233.

[126] Khalid, D.; Amran, M.; Salleh, M.; Azlina, W.; Abdul, W.; Idris, A.; Zainal, Z. Batch adsorption of basic dye using acid treated kenaf fibre char : equilibrium , kinetic and thermodynamic studies. *Chem. Eng. J.*, **2012**, *181–182*, 449–457.

[127] Lu, B.; Hu, L.; Yin, H.; Mao, X.; Xiao, W.; Wang, D. Preparation and application of capacitive carbon from bamboo shells by one step molten carbonates carbonization. *Int. J. Hydrogen Energy*, **2016**, 6–13.

[128] Tingting, W.; Gang, W.; Qiang, D.; Fei, Z.; Xu, Z.; Shaofeng, L.; Huiying, Q.; Jieshan, Q.; 5. Starch derived porous carbon nanosheets for high-performance photovoltaic capacitive deionization. *Environ. Sci. Technol.*, **2017**, 1–25.

[129] Akkaya, G.; Say, H. Optimized preparation for bimodal porous carbon from lentil processing waste by microwave-assisted K_2CO_3 activation : spectroscopic characterization and dye decolorization activity. *J. Clean. Prod. J.*, **2019**, *226*, 968–976.

[130] Wang, L.; Sun, F.; Hao, F.; Qu, Z.; Gao, J.; Liu, M.; Wang, K. A green trace K_2CO_3 induced catalytic activation strategy for developing coal-converted activated carbon as advanced candidate for CO_2 adsorption and supercapacitors. *J. Clean. Prod.*, **2019**, *227*, 1002–1022.

[131] Tsubouchi, N.; Nishio, M.; Shinohara, Y.; Bud, J.; Mochizuki, Y. Production of activated carbon from peat by with natural soda ash and effect of nitrogen addition on the development of surface area. *Fuel Process. Technol.*, **2018**, *176*, 76–84.

[132] Gao, Y.; Yue, Q.; Gao, B.; Li, A. Insight into activated carbon from different kinds of

chemical activating agents : a review. *Sci. Total Environ.*, **2020**, *746*, 1–19.

[133] Chen, W.; Gong, M.; Li, K.; Xia, M.; Chen, Z.; Xiao, H.; Fang, Y.; Chen, Y.; Yang, H.; Chen, H. Insight into KOH activation mechanism during biomass pyrolysis : chemical reactions between O-containing groups and KOH. *Appl. Energy*, **2020**, *278*, 115730.

[134] Bag, O.; Tekin, K.; Karagoz, S. Microporous activated carbons from lignocellulosic biomass by KOH activation. *Fullerenes, Nanotub. Carbon Nanostructures*, **2020**, 1–8.

[135] Casoni, A. I.; Mendioroz, P.; Volpe, M. A.; Gutierrez, V. S. Magnetic amendment material based on bio-char from edible oil industry waste. its performance on aromatic pollutant removal from water. *J. Environ. Chem. Eng.*, **2020**, *8* (2),

[136] Chen, B.; Chen, Z.; Lv, S. A novel magnetic biochar efficiently sorbs organic pollutants and phosphate. *Bioresour. Technol.*, **2011**, *102*, 716–723.

[137] Ali, S.; Zhu, J.; Muhammad, N.; Sheng, T. Effect of synthesis methods on magnetic kans grass biochar for enhanced As(III, V) adsorption from aqueous solutions. *Biomass and Bioenergy*, **2014**, 1–12.

[138] Mubarak, N. M.; Kundu, A.; Sahu, J. N.; Abdullah, E. C. Synthesis of palm oil empty fruit bunch magnetic pyrolytic char impregnating with $FeCl_3$ by microwave heating technique. *Biomass and Bioenergy*, **2013**, *61*, 265–275.

[139] Ashraf, J. M.; Ansari, M. A.; Khan, H. M. Green synthesis of silver nanoparticles and characterization of their inhibitory effects on AGEs formation using biophysical techniques. *Sci. Rep.*, **2016**, *6*, 1–10.

[140] Nadeem, F.; Jamil, N.; Moazzam, A.; Ahmad, S. R.; Lateef, A.; Khalid, A.; Qadir, A.; Ali, A.; Munir, S. Synthesizing and characterizing sawdust biochar/Fe_3O_4 nanocomposites and its potential application in textile wastewater treatment. *Polish J. Environ. Stud.*, **2019**, *28* (4), 2311–2319.

[141] D. Mohan, H. Kumar, A. Saraswat, M. Alexandre-Franco, C. U. Cadmium and lead remediation using magnetic oak wood and oak bark fast pyrolysis bio-chars. *Chem. Eng. J.*, **2014**, *236* (15), 513–528.

[142] Bardestani, R.; Patience, G. S. Experimental methods in chemical engineering : specific surface area and pore size distribution measurements — BET ,. *Can. J. Chem. Eng.*, **2019**, *97*, 2781–2791.

[143] Wang, S.; Gao, B.; Zimmerman, A. R.; Li, Y.; Ma, L.; Harris, W. G.; Migliaccio, K. W. Removal of arsenic by magnetic biochar prepared from pinewood and natural hematite. *Bioresour. Technol.*, **2015**, *175*, 391–395.

[144] Zheng, Y.; Wan, Y.; Chen, J.; Chen, H.; Gao, B. MgO modified biochar produced

through ball milling : a dual-functional adsorbent for removal of different contaminants. *Chemosphere*, **2020**, *243* (125344), 1–7.

[145] Aboustait, M.; Kim, T.; Ley, M. T.; Davis, J. M. Physical and chemical characteristics of fly ash using automated scanning electron microscopy. *Constr. Build. Mater.*, **2016**, *106*, 1–10.

[146] Baisheng, N.; Xianfeng, L.; Longlong, Y.; Junqing, M.; Xiangchun, L. Pore structure characterization of different rank coals using gas adsorption and scanning electron microscopy. *FUEL*, **2015**, *158*, 908–917.

[147] Eaton, P.; Quaresma, P.; Soares, C.; Neves, C.; Almeida, M. P. De; Pereira, E.; West, P. A direct comparison of experimental methods to measure dimensions of synthetic nanoparticles. *Ultramicroscopy*, **2017**, *182*, 179–190.

[148] Wang, Y.; Xie, X.; Chen, X.; Huang, C.; Yang, S. Biochar-loaded Ce^{3+} enriched ultrafine ceria nanoparticles for phosphate dsorption. *J. Hazard. Mater.*, **2020**, *396*, 1–8.

[149] Chauhan, A. Powder XRD technique and its applications in science and technology. *J. Anal. Bioanal. Tech.*, **2020**, *5* (5), 1–6.

[150] Kim, S. H.; Lee, C. M.; Kafle, K. Characterization of crystalline cellulose in biomass : basic principles , applications , and limitations of XRD , NMR , IR , Raman , and SFG. *Korean J. Chem. Eng.*, **2013**, *30* (12), 2127–2141.

[151] Zhang, K.; Cheng, Y.; Li, W.; Hao, C.; Hu, B. Microcrystalline characterization and morphological structure of tectonic anthracite using XRD , liquid nitrogen adsorption , mercury porosimetry , and micro-CT. *Energy & Fuels*, **2019**, *33*, 10844–10851.

[152] Xu, X.; Hu, X.; Ding, Z.; Chen, Y.; Gao, B. Waste-art-paper biochar as an effective sorbent for recovery of aqueous Pb(II) into value-added PbO nanoparticles. *Chem. Eng. J.*, **2017**, *308*, 863–871.

[153] Lyu, H.; Tang, J.; Huang, Y.; Gai, L.; Zeng, E. Y.; Liber, K.; Gong, Y. Removal of hexavalent chromium from aqueous solutions by a novel biochar supported nanoscale iron sulfide composite. *Chem. Eng. J.*, **2017**, *322*, 516–524.

[154] Sen, K.; Mishra, D.; Debnath, P.; Mondal, A.; Mondal, N. K. Adsorption of uranium (VI) from groundwater by silicon containing biochar supported iron oxide nanoparticle. *Bioresour. Technol. Reports*, **2021**, *14* (1000659), 1–8.

[155] Zhu, D.; Chen, Y.; Yang, H.; Wang, S.; Wang, X.; Zhang, S.; Chen, H. Synthesis and characterization of magnesium oxide nanoparticle- containing biochar

composites for efficient phosphorus removal from aqueous solution. *Chemosphere*, **2020**, *247*, 125847.

[156] Das, V. C. P.; Roy, P. K. Synthesis and application of graphene oxide - coated biochar composite for treatment of strontium - containing solution. *Int. J. Environ. Sci. Technol.*, **2021**, *18*, 1953–1966.

[157] Asim, A. Y.; Tabassum, P.; Khalid, U.; Mohamad Nasir, M. I. Role of nanomaterials in the treatment of wastewater: a review. *Water*, **2020**, *12* (495), 1–30.

[158] Yu, P.; Hu, T.; Chen, H. H.; Wu, F.; Liu, H. Effective removal of congo red by triarrhena biochar loading with TiO_2 nanoparticles. *Scanning*, **2018**, *2018*, 1–8.

[159] Zhang, H.; Xu, F.; Xue, J.; Chen, S.; Wang, J.; Yang, Y. Enhanced removal of heavy metal ions from aqueous solution using manganese dioxide-loaded biochar: behavior and mechanism. *Sci. Rep.*, **2020**, *10* (1), 1–13.

[160] Yu, P.; Hu, T.; Chen, H. H.; Wu, F.; Liu, H. Synthesizing and Characterizing Sawdust Biochar/Fe_3O_4 Nanocomposites and Its Potential Application in Textile Wastewater Treatment. *Pol. J. Environ. Stud.*, **2019**, *28* (4), 2311–2319.

[161] Zawrah, M. F.; El, M. I.; Mahmoud, G.; Mervat, S.; Sonbati, A. El; Ahmed, M. Recycling of rice husk for preparation of activated carbon/magnetite nanocomposites for removal of methylene blue from wastewater. *Int. J. Environ. Res.*, **2023**, *17*, 51.

[162] Ahmadi, A.; Foroutan, R.; Esmaeili, H. The role of bentonite clay and bentonite clay@$MnFe_2O_4$ composite and their physico-chemical properties on the removal of Cr(III) and Cr(VI) from aqueous media. *Environ. Sci. Pollut. Res.*, **2020**, *27*, 14044–14057.

[163] Sukhbaatar, B.; Yoo, B.; Lim, J. Metal-free high-adsorption-capacity adsorbent derived from spent coffee grounds for methylene blue. *R. Soc. Chem.*, **2021**, *11*, 5118–5127..

[164] Qu, L.; Han, T.; Luo, Z.; Liu, C.; Mei, Y.; Zhu, T. One-step fabricated Fe_3O_4@C core–shell composites for dye removal : kinetics , equilibrium and thermodynamics. *J. Phys. Chem. Solids*, **2015**, *78*, 20–27.

[165] Cervera-Gabalda, L.; Gómez-Polo, C. Magnetic Fe/Fe_3C@C nanoadsorbents for efficient Cr(VI) Removal. *Int. J. Mol. Sci.*, **2022**, *23*, 15135.

[166] Kataria, N.; Chauhan, A. K.; Garg, V. K.; Kumar, P. Sequestration of heavy metals from contaminated water using magnetic carbon nanocomposites. *J. Hazard.*

Mater. Adv., **2022**, *6*, 100066.

[167] Zhang, X.; Yi, G.; Zhang, Z.; Yu, J.; Fan, H.; Li, P.; Zeng, H. magnetic graphene-based nanocomposites as highly efficient absorbents for Cr(VI) removal from wastewater. *Environ. Sci. Pollut. Res.*, **2021**, *28*, 14671–14680.

[168] Zheng, Y.; Wang, J.; Li, D.; Liu, C.; Lu, Y.; Lin, X. Insight into the KOH / $KMnO_4$ activation mechanism of oxygen-enriched hierarchical porous biochar derived from biomass waste by in-situ pyrolysis for methylene blue enhanced adsorption. *J. Anal. Appl. Pyrolysis*, **2021**, *158*, 105269.

[169] Ying, D.; Hong, P.; Jiali, F.; Qinqin, T.; Yuhui, L.; Youqun, W.; Zhibin, Z.; Xiaohong, C.; Yunhai, L. Biomass and bioenergy removal of uranium using MnO_2/orange peel biochar composite prepared by activation and in-situ deposit in a single step. *Biomass and Bioenergy*, **2020**, *142*, 105772.

[170] Bakatula, E. N.; Richard, D.; Neculita, C. M.; Zagury, G. J. Determination of point of zero charge of natural organic materials. *Environ. Sci. Pollut. Res.*, **2018**, *25* (8), 7823–7833.

[171] Koochakzadeh, F.; Norouzbeigi, R.; Shayesteh, H. Statistically optimized sequential hydrothermal route for $FeTiO_3$ surface modification: evaluation of hazardous cationic dyes adsorptive removal. *Environ. Sci. Pollut. Res.*, **2023**, *30* (7), 19167–19181.

[172] Zhang, M.; Gao, B.; Yao, Y.; Xue, Y.; Inyang, M. Synthesis of porous MgO-biochar nanocomposites for removal of phosphate and nitrate from aqueous solutions. *Chem. Eng. J.*, **2012**, *210*, 26–32.

[173] Fang, C.; Zhang, T.; Li, P.; Jiang, R.; Wang, Y. Application of magnesium modified corn biochar for phosphorus removal and recovery from Swine wastewater. *Int. J. Environ. Res. Public Heal.*, **2014**, *11*, 9217–9237.

[174] Fang, C.; Zhang, T.; Li, P.; Jiang, R.; Wu, S.; Nie, H.; Wang, Y. Phosphorus recovery from biogas fermentation liquid by Ca-Mg loaded biochar. *J. Environ. Sci.*, **2015**.

[175] Zheng, Y.; Zimmerman, A. R.; Gao, B. Comparative investigation of characteristics and phosphate removal by engineered biochars with different loadings of magnesium , aluminum , or iron. *Sci. Total Environ.*, **2020**, *747*, 141277.

[176] Giraldo, S.; Robles, I.; God, L. A.; Acelas, N. Experimental and theoretical insights on methylene blue removal from wastewater using an adsorbent obtained

from the residues of the orange industry. *Molecules*, **2021**, *26*, 4555.

[177] Haider, Z.; Gao, M.; Qiu, W.; Song, Z. Mechanisms for cadmium adsorption by magnetic biochar composites in an aqueous solution. *Chemosphere*, **2020**, *246*, 125701.

[178] Jung, K. W.; Lee, S. Y.; Choi, J. W.; Lee, Y. J. A facile one-pot hydrothermal synthesis of hydroxyapatite/biochar nanocomposites: adsorption behavior and mechanisms for the removal of copper(II) from aqueous media. *Chem. Eng. J.*, **2019**, *369*, 529–541.

[179] Bandar, S.; Anbia, M.; Salehi, S. Comparison of MnO_2 modified and unmodified magnetic Fe_3O_4 nanoparticle adsorbents and their potential to remove iron and manganese from aqueous media. *J. Alloys Compd.*, **2021**, *851*, 156822.

[180] Upadhyay, S.; Parekh, K.; Pandey, B. Influence of crystallite size on the magnetic properties of Fe_3O_4 nanoparticles. *J. Alloys Compd.*, **2016**, *678*, 478–485.

[181] Adorna, J.; Borines, M.; Dang, V. D.; Doong, R. Coconut shell derived activated biochar – manganese dioxide nanocomposites for high performance capacitive deionization. *Desalination*, **2020**, *492*, 114602.

[182] Goswami, R.; Shim, J.; Deka, S.; Kumari, D.; Kataki, R. Characterization of cadmium removal from aqueous solution by biochar produced from *Ipomoea fistulosa* at different pyrolytic temperatures. *Ecol. Eng.*, **2016**, *97*, 444–451.

[183] Krishna Murthy, T. P.; Gowrishankar, B. S. Process optimisation of methylene blue sequestration onto physical and chemical treated coffee husk based adsorbent. *SN Appl. Sci.*, **2020**, *2*, 836..

[184] Paredes-laverde, M.; Salamanca, M.; Diaz-corrales, J. D.; Fl, E.; Silva-agredo, J.; Torres-palma, R. A. Understanding the removal of an anionic dye in textile wastewaters by adsorption on $zncl_2$ activated carbons from rice and coffee husk wastes : a combined experimental and theoretical study. *J. Environ. Chem. Eng.*, **2021**, *9*, 105685.

[185] Kumar, U.; Vibhute, B.; Sharma, N.; Sahay, A. Efficient removal of methylene blue dye by alkaline-treated banana stem biochar through adsorption method. *Appl. Ecol. Environ. Sci.*, **2022**, *10* (4), 236–243..

[186] Le, V. T.; Tran, T. K. N.; Tran, D. L.; Le, H. S.; Doan, V. D.; Bui, Q. D.; Nguyen, H. T. One-Pot synthesis of a novel magnetic activated carbon/clay composite for removal of heavy metals from aqueous solution. *J. Dispers. Sci. Technol.*, **2018**.

[187] Fakhri, A. Adsorption characteristics of graphene oxide as a solid adsorbent for

aniline removal from aqueous solutions: kinetics, thermodynamics and mechanism studies. *J. Saudi Chem. Soc.*, **2013**..

[188] Song, X.; Li, L.; Geng, Z.; Zhou, L.; Ji, L. Effective and Selective Adsorption of As(III) via Imprinted Magnetic Fe_3O_4/HTCC composite nanoparticles. *J. Environ. Chem. Eng.*, **2017**, *5* (1), 16–25.

[189] Argun, M. E.; Güclü, D.; Karatas, M. Adsorption of reactive blue 114 dye by using a new adsorbent: pomelo peel. *J. Ind. Eng. Chem.*, **2014**, *20* (3), 1079–1084.

[190] Hamid, N. A.; You, J. J. Mangosteen peel-derived hydrochar prepared via hydrothermal carbonization for methylene blue removal. *IOP Conf. Ser. Earth Environ. Sci.*, **2021**, *765*, 012114.

[191] Ma, J.; Yu, F.; Zhou, L.; Jin, L.; Yang, M.; Luan, J.; Tang, Y.; Fan, H.; Yuan, Z.; Chen, J. Enhanced adsorptive removal of methyl orange and methylene blue from aqueous solution by alkali-activated multiwalled carbon nanotubes. *ACS Appl. Mater. Interfaces*, **2012**, *4*, 5749–5760.

[192] Islam, M. A.; Ahmed, M. J.; Khanday, W. A.; Asif, M.; Hameed, B. H. Mesoporous activated carbon prepared from NaOH activation of rattan (*Lacosperma secundiflorum*) hydrochar for methylene blue removal. *Ecotoxicol. Environ. Saf.*, **2017**, *138*, 279–285.

[193] Subratti, A.; Ladeira, J.; Lalgee, L. J.; Kerton, F. M.; Jalsa, N. K. Preparation and characterization of biochar derived from the fruit seed of *Cedrela odorata* L and evaluation of its adsorption capacity with methylene blue. *Sustain. Chem. Pharm.*, **2021**, *21*, 100421.

[194] Lisandra de Castro, A.; Susana, Y.-V.; Yolanda, P.-R.; José, R. Efficient separation of heavy metals by magnetic nanostructured beads. *Inorganics*, **2020**, *8*, 40.

[195] Kumar, J. A.; Amarnath, D. J.; Senthil Kumar, P.; Kaushik, C. S.; Varghese, M. E.; Saravanan, A. Mass Transfer and thermodynamic analysis on the removal of naphthalene from aqueous solution using oleic acid modified palm shell activated carbon. *Desalin. Water Treat.*, **2018**, *106* (January), 238–250.

[196] Kumar, J. A.; Krithiga, T.; Narendrakumar, G.; Prakash, P.; Balasankar, K.; Sathish, S.; Prabu, D.; Pushkala, D. P.; Marraiki, N.; Ramu, A. G.; et al. Effect of Ca^{2+} ions on naphthalene adsorption/desorption onto calcium oxide nanoparticle: adsorption isotherm, kinetics and regeneration studies. *Environ. Res.*, **2022**, *204* (PB), 112070.

[197] Tran, T. H.; Le, H. H.; Pham, T. H.; Nguyen, D. T.; La, D. D.; Chang, S. W.; Lee,

S. M.; Chung, W. J.; Nguyen, D. D. Comparative study on methylene blue adsorption behavior of coffee husk-derived activated carbon materials prepared using hydrothermal and soaking methods. *J. Environ. Chem. Eng.*, **2021**, *9* (4), 105362.

[198] Zewdu, F.; Amare, M. Determination of the level of hexavalent , trivalent , and total chromium in the discharged effluent of bahir dar tannery using ICP-OES and UV–Visible spectrometry determination of the level of hexavalent , trivalent , and total chromium in the discharg. *Cogent Chem.*, **2018**, *4* (1), 1–9.

[199] Dame, J.; Wedajo, F.; Molole, G. J.; Gure, A. Salting-out assisted liquid-liquid extraction of Cr(VI) from water samples before its determination by UV-Vis spectrophotometry. *J. Chem.*, **2023**, 8857010.

[200] Ma, Y.; Liu, W.; Zhang, N.; Li, Y.; Jiang, H.; Sheng, G. Polyethylenimine modified biochar adsorbent for hexavalent chromium removal from the aqueous solution. *Bioresour. Technol.*, **2014**, *169*, 403–408.

[201] Zhao, F.; Shan, R.; Gu, J.; Zhang, Y.; Yuan, H.; Chen, Y. Magnetically recyclable loofah biochar by $KMnO_4$ modifiation for adsorption of Cu(II) from aqueous solutions. *ACS Omega*, **2022**, *7*, 8844–8853.

[202] Julien, C. M. Local Structure of lithiated manganese oxides. *Solid State Ionics*, **2006**, *177*, 11–19.

[203] Qin, Q.; Wang, Q.; Fu, D.; Ma, J. An efficient approach for Pb(II) and Cd(II) removal using manganese dioxide formed in situ. *Chem. Eng. J.*, **2011**, *172* (1), 68–74.

[204] Zeghioud, H.; Fryda, L.; Mahieu, A.; Visser, R.; Kane, A. Potential of flax shives and beech wood - derived biochar in methylene blue and carbamazepine removal from aqueous solutions. *Materials*, **2022**, *15*, 2824.

[205] Tao, X.; Wu, Y.; Cha, L. Shaddock Peels-Based Activated carbon as cost-saving adsorbents for efficient removal of Cr(VI) and methyl orange. *Environ. Sci. Pollut. Res.*, **2019**, *26*, 19828–19842.

[206] Kumar, U.; Vibhute, B.; Sharma, N.; Sahay, A. Efficient removal of methylene blue dye by alkaline-treated banana stem efficient removal of methylene blue dye by alkaline-treated banana stem biochar through adsorption method. *Appl. Ecol. Environ. Sci.*, **2022**, *10* (4), 236–243.

[207] Serafin, J.; Dziejarski, B. Application of isotherms models and error functions in activated carbon CO_2 sorption processes. *Microporous Mesoporous Mater.*, **2023**,

354, 112513.

[208] Ji, C.; Yin, H.; Zhou, M.; Sun, Z. Adsorption of total petroleum hydrocarbon in groundwater by KOH-activated biochar loaded double surfactant-modified NZVI. *Front. Mater.*, **2023**, 1–15.

[209] Coetzee, J. J.; Bansal, N.; Chirwa, E. M. N. Chromium in environment , its toxic effect from chromite - mining and ferrochrome industries , and its possible bioremediation. *Expo. Heal.*, **2018**, No. 0123456789.

[210] Gracepavithra, K.; Jaikumar, V.; Kumar, P. S. A review on cleaner strategies for chromium industrial wastewater : present research and future perspective. *J. Clean. Prod.*, **2019**, *228*, 580–593.

[211] Sanchez-Hachair, A.; Hofmann, A. Hexavalent chromium quantification in solution: comparing direct UV–Visible spectrometry with 1,5-Diphenylcarbazide colorimetry. *Comptes Rendus Chim.*, **2018**, *21* (9), 890–896.

[212] Cui, B.; Chen, Z.; Wang, F.; Zhang, Z.; Dai, Y.; Guo, D.; Liang, W.; Liu, Y. Facile synthesis of magnetic biochar derived from burley tobacco stems towards enhanced Cr(VI) removal: performance and mechanism. *Nanomaterials*, **2022**, *12* (4).

[213] Liang, M.; Ding, Y.; Zhang, Q.; Wang, D.; Li, H.; Lu, L. Removal of aqueous Cr(VI) by magnetic biochar derived from bagasse. *Sci. Rep.*, **2020**, *10* (1), 1–13.

[214] Mahanty, B.; Mondal, S. Synthesis of magnetic biochar using agricultural waste for the separation of Cr(VI) from aqueous solution. *Arab. J. Sci. Eng.*, **2021**, *46* (11), 10803–10818.

[215] Bagherzadeh, M.; Aslibeiki, B.; Arsalani, N. Preparation of Fe_3O_4/vine shoots derived activated carbon nanocomposite for improved removal of Cr(VI) from aqueous Solutions. *Sci. Rep.*, **2023**, *13* (1), 1–19.

APPENDICES

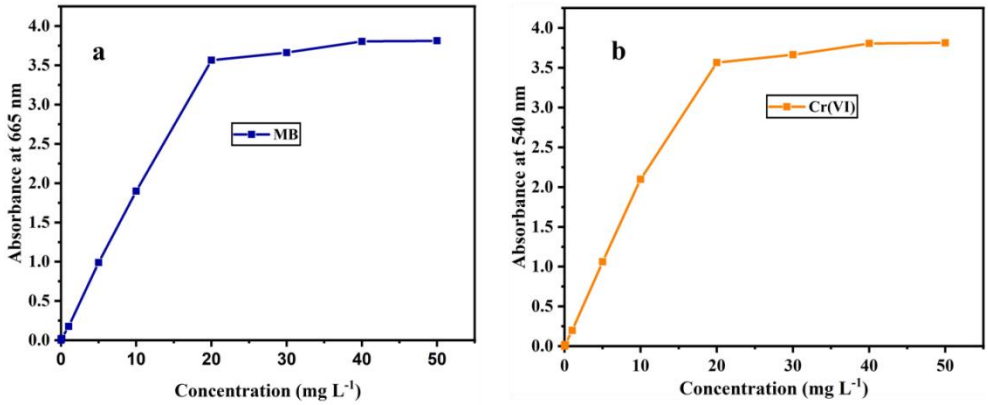

Figure A1. Linearity range for MB and Cr(VI) analysis.

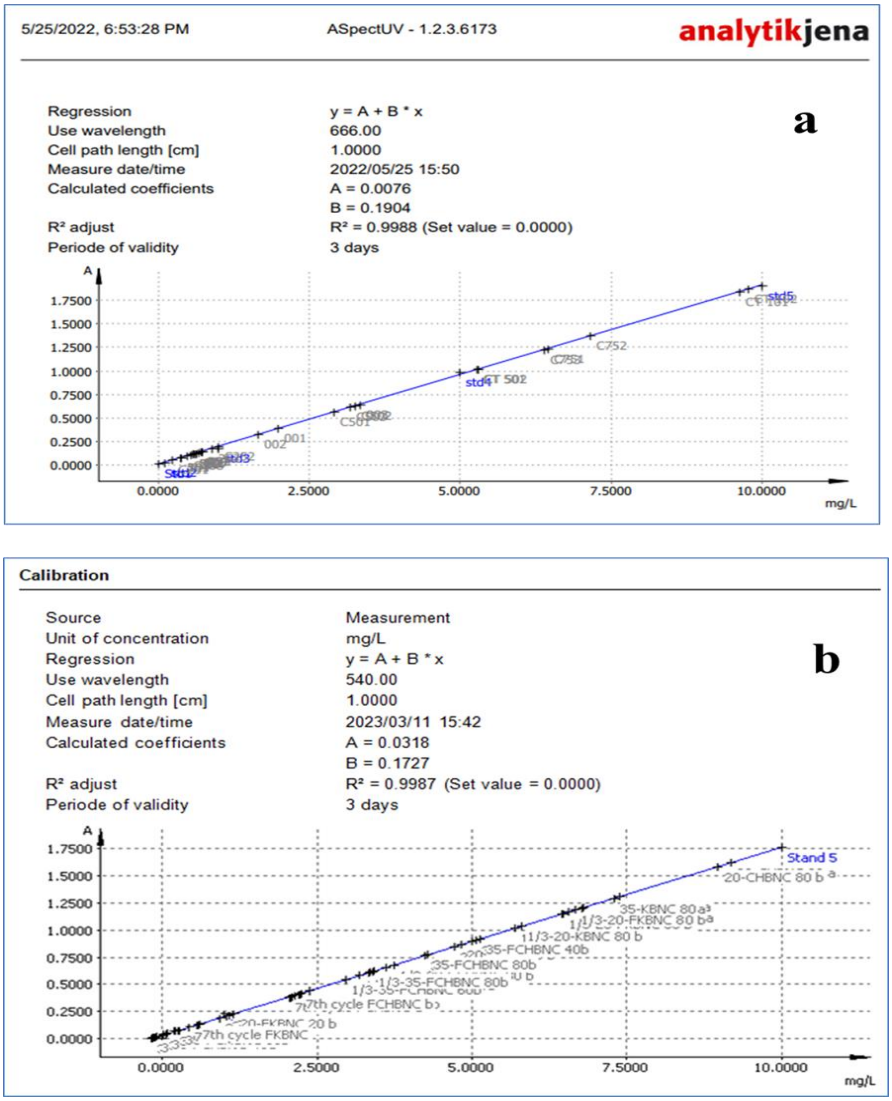

Figure A2. Calibration curve for (a) MB and (b) Cr(VI) analysis.

CURRICULUM VITAE

Name: Jemere Kochito Ayano (MSc.)

Academic rank: Lecturer

Professional Address: Department of Chemistry

College of Natural Sciences

Mizan Tepi University, Mizan Aman, Ethiopia

Email address: jemere@mtu.edu.et/jemerekochito@gmail.com

Telephone number: +251(9)12202360

ORCID id: 0000-0003-3274-9457

Google Scholar: Jemere Kochito Ayano - Google Scholar

University education

- ✓ Doctor of Philosophy (PhD) Candidate in chemistry (Analytical) at Jimma University, Ethiopia.
- ✓ Master of Science in Chemistry (Analytical) obtained from Ambo University, Ethiopia, July 2011.
- ✓ Bachelor of Education (BEd) in Chemistry obtained from Addis Ababa University, Ethiopia, August 2007

Leadership experience

- ✓ Vice President for Business and Resource Development of Mizan Tepi University, as of Dec.2016 - Sept. 2019
- ✓ Vice President for Administration, Business and Resource Development of Mizan Tepi University, Feb.2014 - Dec. 2016
- ✓ Chief Executive Director of Tepi Campus, Dec. 2012 - Feb. 2014
- ✓ Dean of the Students Affairs of Tepi Campus. July 2011 - Dec.2012
- ✓ Associate of the Registrar Officer of Tepi Campus, Nov. 2007 - Oct. 2009

Research interest

- ✓ Analytical methods development for the analysis of pesticide residues and their degradation products, pollutants such synthetic dyes and toxic heavy metals in water, food, beverages, biological and environmental samples.

List of publications

1. **Kochito, J.**; Gure, A.; Abdissa, N.; Beyene, T. T.; Femi, O. E. MnOx-*Coffea arabica* Husk and *Catha edulis* Leftover Biochar Nanocomposites for Removal of Methylene blue from Wastewater. *Sci. World J.*, **2024**, ID. 7585145. DOI:10.1155/2024/7585145.
2. **Kochito, J.**; Gure, A.; Abdisa, N.; Tadesse, T.; Femi, O. E. Magnetic Iron-oxide Coffee Husk and Khat Waste Biochar Nanocomposites for Removal of Methylene blue from Aqueous Solution. *Sep. Sci. plus.*, **2024**, 2300246.
3. **Kochito, J.**; Gure, A.; Abdisa, N.; Tadesse, T.; Femi, O. E. Magnetic Biochar Nanocomposites of Coffee Husk and Khat (Catha Edulis) Leftover for Removal of Cr(VI) from Wastewater. *Curr. Res. Green Sustain. Chem.*, **2024**, *8*, 100403.
4. Ago, K.A., Gure A., Kitte, S.A., **Kochito, J.,** Balcha, Y.B. Vortex Assisted Dispersive Micro-Solid-Phase Extraction using Fe_2O_3-Modified Khat (Catha Edulis) Biochar Nanocomposite Supported with Silica for the Determination of Organochlorine Pesticides in Juice Samples using GC-MS. *J. Environ. Sci. Health, Part B*, **2024**, 1–14. Doi: 10.1080/03601234.2024.2336572.
5. **Kochito, J.**; Femi, O. E; Beyene, T. T.; Abdissa, N.; Gure, A. Manganese oxide-coffee husk and khat (*Catha edulis)* leftover biochar nanocomposites for removal of Cr (VI) from wastewater. *Bull. Chem. Soc. Ethiop.* **2024**, *38* (5*) (accepted, in press)*

Conference presentations

- **Kochito J**, Gure, A.; Abdisa, N.; Gonfa, G.; Femi, O. E. (2022) Synthesis and characterization of biochar–based nanocomposite adsorbents for the removal of heavy metals from waste water. The 11th National research conference of Mizan Tepi University held from June 10-11, at Mizan Tepi University Tepi Campus, Tepi, Ethiopia.